Liquid Phase Exfoliation of 2D Materials under Ambient Conditions

John B. Boland

A thesis submitted for the degree of

Doctor of Philosophy

2020

Approved 2021

Supervised by Professor Jonathan Coleman

Chemical Physics of Low Dimensional Nanostructures Group

School of Physics

Trinity College Dublin

Abstract:

A technique developed by the Coleman group in 2008 called liquid phase exfoliation (LPE) has been shown to be effective for the delamination of any material exhibiting a layered structure.

Molybdenum dioxide (MoO_2) was identified as promising candidate for exfoliation, and a natural successor to extensive work carried out previously on molybdenum trioxide (MoO_3). This material shows promise for a number of applications in the electrochemical energy storage arena. Mostly studied as a bulk layered material, MoO_2 has not previously been exfoliated in large quantities.

Chapter 3 of this thesis describes the work performed with MoO_2, the primary goal of which was to use the increased surface area of the exfoliated material to maximise lithium storage capacity. After preliminary research the objectives were also revised to include achieving an understanding of the oxidation process of MoO_2 in ambient conditions and identifying a means to slow this process to facilitate battery fabrication.

Initial tests of MoO_2 dispersions indicated a layered structure, contradicting the general perception of the material. Exfoliation conditions such as sonication time and subsequent centrifugation rates were optimised, and isopropanol (IPA) was identified as a suitable solvent for dispersion of the nanosheets.

It was found that when dispersed in IPA under ambient conditions, MoO_2 nanosheets are gradually oxidized to higher oxides such as MoO_3 over a period of days. Conversely, if the nanosheets are processed into dried films immediately after exfoliation, and before oxidation has had a chance to progress, the nanosheets are relatively stable under ambient conditions, remaining unoxidised unless the films are heated. It was found that MoO_2 nanosheets could be size selected by controlled centrifugation and showed size-dependent optical properties, which allowed the proposal of spectroscopic metrics for concentration and size-estimation from extinction spectra. Liquid-exfoliated nanosheets were used to produce lithium ion battery anodes with capacities up to 1140 $mAhg^{-1}$.

The propensity of many 2D materials to oxidize in ambient conditions can complicate production and limit applications potential. Described in Chapter 4 is ambient liquid phase exfoliation of germanium sulfide (GeS), a layered material known for its chemical instability. The goal of this research was to gain an understanding of the degradation

process and to potentially identify a means of alleviating the problem. The previously optimized parameters from the work on MoO_2 were utilised to easily identify the ideal exfoliation conditions for this material. Ambient exfoliation in organic solvents such as N-methyl-pyrrolidone yields good quality multi-layer GeS nanosheets. Although oxidation appears to occur with a time constant of ~10 days, the data suggests it to be limited to nanosheet edges leaving the basal plane intact. The rate of oxidation is slow enough to allow processing of the dispersions. For example, it was possible to size-select GeS nanosheets and characterize the size-dependence of nanosheet optical properties, leading to the observation of significant changes in bandgap with nanosheet thickness. Additionally, it is possible to incorporate the nanosheets into lithium ion battery anodes using carbon nanotubes as both binder and conductive additive. These electrodes were relatively stable and displayed near-theoretical capacity of 1523 mAh/g.

Chapter 5 of this thesis entails the preliminary work in the extension of LPE to a new application – light emission. Light-emitting electrochemical cells (LECs) were first demonstrated in 1995 and have since been lauded as a potential successor to OLEDs for solid state artificial lighting due to their simpler architecture and lower production cost when compared to state of the art OLEDs. Solution processable luminescent material is ideally required for the fabrication of these devices and given that LPE dispersions can readily be spray-deposited, they potentially provide a largely untapped source of light-emitting material to compete with those currently in circulation.

Declaration:

I declare that this thesis has not been submitted as an exercise for a degree at this or any other university and it is entirely my own work.

I agree to deposit this thesis in the University's open access institutional repository or allow the library to do so on my behalf, subject to Irish Copyright Legislation and Trinity College Library conditions of use and acknowledgement.

Elements of this work that have been carried out jointly with others or by collaborators have been duly acknowledged in the text wherever included.

_____

John B. Boland

Acknowledgements:

First and foremost, I owe a huge debt of gratitude to Professor Jonathan Coleman for providing me with this wonderful opportunity. It may have just been a quick nod and thumbs up across the room for him, but for me it was life changing.

I would like to show my appreciation for all the members of the Coleman group, both past and present, for the comradery and the fantastic work environment they continue to provide. A special word of thanks to Andrew Harvey for his advice, training and guidance, and the friendship that followed.

I also wish to wholeheartedly thank Colin & Sean, Dan & Jakub, Dave & Ivan and Mark for their friendship, and Conor & Hannah for putting up with me at home.

To my grandparents Peter & Bridie Gough and Tom & Elizabeth Boland, thank you for the value you placed on education. Your vision, sacrifices and support blessed us, your grandchildren, with the gift of learning.

It is difficult to find words to adequately describe how grateful I am to my parents, Trish Gough and John Boland. They have always fostered in me a great appreciation for education in general, but in particular are responsible for both kindling my interest and passion for the sciences and mathematics, and ultimately for the work described here. This thesis is of Masonbrook, Baylin as much as Trinity College Dublin.

Finally, I would like to thank my siblings, Lisa and Daniel and my girlfriend Aideen for their constant encouragement and support. I could not have made it this far without you.

Contents

List of publications:

1. *Liquid phase exfoliation of MoO_2 nanosheets for lithium ion battery applications*, John B. Boland, Andrew Harvey, Ruiyuan Tian, Damien Hanlon, Victor Vega-Mayoral, Beata Szydlowska, Aideen Griffin, Tanja Stimpel-Lindner, Sonia Jaskaniec, Valeria Nicolosi, Georg Duesberg and Jonathan N. Coleman. *Nanoscale Adv*., 2019, 1, 1560-1570.
2. *Liquid phase exfoliation of GeS nanosheets in ambient conditions for lithium ion battery applications*, John B. Boland, Andrew Harvey, Ruiyuan Tian, Victor Vega-Mayoral, Aideen Griffin, Dominik V. Horvath, Cian Gabbett, Madeleine Breshears, Joshua Pepper, Yanguang Li and Jonathan N. Coleman. *2D Mater*. **7** (2020) 035015.
3. *Non-resonant light scattering in dispersions of 2D nanosheets*, Andrew Harvey, Claudia Backes, John B. Boland, Xiaoyun He, Aideen Griffin, Beata Szydlowska, Cian Gabbett, John F. Donegan and Jonathan N. Coleman. *Nature Communications*, 2018, 9, 4553.
4. *Exploring the versatility of liquid phase exfoliation: Producing 2D nanosheets from talcum powder, cat litter and beach sand*, Andrew Harvey, John B. Boland, Ian Godwin, Adam G. Kelly, Beata Szydlowska, Ghulam Murtaza, Andrew Thomas, David J. Lewis, Paul O'Brien and Jonathan N. Coleman. *2D Mater*., 2017, 4, 025054.
5. *Exfoliation in endotoxin-free albumin generates pristine graphene with reduced inflammatory properties*, Filipa Lebre, Damien Hanlon, John B. Boland, Jonathan N. Coleman and Ed C. Lavelle. *Advanced Biosystems*, 2018, 2, 1800102.
6. *Liquid exfoliated $Co(OH)_2$ nanosheets as low-cost, yet high-performance, catalysts for the oxygen evolution reaction*, David Mcateer, Ian Godwin, Zheng Ling, Andrew Harvey, Lily He, Conor S. Boland, Victor Vega-Mayoral, Beata Szydlowska, Aurelie A. Rovetta, Claudia Backes, John B. Boland, Xin Chen, Michael E. G. Lyons and Jonathan N. Coleman. *Adv. Energy Mater.*, 2018, 8, 1702965.
7. *Carbon nanotubes-bridged molybdenum trioxide nanosheets as high performance anode for lithium ion batteries*, Haiyan Sun, Damien Hanlon, Duc Anh Dinh, John B. Boland, Antonio Esau Del Rio Castillo, Carlo Di Giovanni, Alberto Ansaldo, Vittorio Pellegrini, Jonathan N. Coleman and Francesco Bonaccorso. *2D Mater.*, 2018, 5, 015024.
8. *Dependence of photocurrent enhancements in quantum dot (QD) sensitized MoS_2 devices on MoS_2 film properties*, John J. Gough, Niall McEvoy, Maria O'Brien, Alan

P. Bell, David McCloskey, John B. Boland, Jonathan N. Coleman, Georg S. Duesberg, A. Louise Bradley. *Adv. Funct. Mater.*, 2018, 28, 1706149.

9. *Graphene-coated polymer foams as tuneable impact sensors*, Conor S. Boland, Umar Khan, Matthew Binions, Sebastian Barwich, John B. Boland, Denis Weaire and Jonathan N. Coleman. *Nanoscale*, 2018, 10, 5366-5375.
10. *Whiskey-phase exfoliation: exfoliation and printing of nanosheets using Irish whiskey*, Adam G. Kelly, Victor Vega-Mayoral, John B. Boland and Jonathan N. Coleman. *2D Mater.*, 2019, 6, 045036.
11. *Nonradiative energy transfer and photocurrent enhancements in hybrid quantum dot-MoS_2 devices*, John J. Gough, Niall McEvoy, Maria O'Brien, Alan P. Bell, John McManus, David McCloskey, John B. Boland, Jonathan N. Coleman, Georg S. Duesberg and A. Louise Bradley. *20th International Conference on Transparent Optical Networks (ICTON), Bucharest,* 2018, pp. 1-4.
12. *Pristine graphene induces innate immune training*, Filipa Lebre, John B. Boland, Pedro Gouveia, Aoife Gorman, Mimmi Lundahl, Fergal O'Brien, Jonathan N. Coleman and Ed C. Lavelle. Submitted to *Nanoscale* November 2019.

To Lisa and Daniel,

The Doctors before and after

1

An Introduction to Layered Materials

1.1 Layered materials:

Two-dimensional materials are those which consist of stratified planes of atoms making up a crystal. These planes can be monatomically thin, as is the case with graphene[1], or consist of monolayers a few atoms thick, such as molybdenum disulphide (MoS_2)[2]. In either case, a defining quality of layered materials is the strong intralayer covalent bonds within these monolayers, and the significantly weaker van der Waals bonds between the stacked layers. This disparity in bond strength allows the individual layers to be isolated via exfoliation. Once delaminated the material can exhibit changes in its properties when compared to the bulk.

1.2 Carbon:

Carbon (originating from the Latin term *carbonem/carbo* meaning coal or charcoal) is one of the most abundant elements in the world around us and a core component in the make-up of every living thing on the planet. Its four valence electrons ensure that it is an extremely versatile element regarding bond formation[3] and there are myriad carbon compounds which exist naturally and many more that can be synthesized. Activated charcoal is a form of carbon that has been used for millennia, indicating that the extraordinary properties of this material were recognised by early civilisations. The ability of charcoal to adsorb poisons when ingested meant it saw extensive use in medical treatment throughout history, as far back as the ancient Egyptians and Greeks[4], and is still used to this day in a similar manner. Filtration using activated carbon is used in some modern systems to remove unwanted contaminants from water. It appears that this idea may have also been adopted by the Phoenicians, who opted to store their water in containers of charred wood while on sea voyages.[5] It was perhaps observed that water stored in this manner remained cleaner than alternative methods, although this is only speculation. Swords, daggers and blades have been discovered in the Middle East, which were used hundreds of years ago and at the time, simultaneously had a much harder cutting edge and were more flexible than the weapons being used in medieval Europe. These weapons were fashioned with what is called ‘Damascus steel’, named after the city in Syria. The metal had a mottled appearance, caused by carburization[6]. Unfortunately, the exact methods used have been lost, but examination of these weapons has shown carbon nanotubes within the structure of the blade.[7]

Some of the most common forms of carbon found naturally are graphite and diamond.[8] Graphite consists of stacked planes of sp^2 hybridised carbon atoms in a hexagonal arrangement, with each atom covalently bonded to three other carbon atoms.[9] These bonds are much stronger than the van der Waals forces between the individual planes. This means the material can be delaminated easily and gives it a soft and slippery feel. The ease with which the material can be deposited gave rise to its use in early script and written works. Indeed, this is where the name originates, from the word *graphein,* meaning "write" in Greek. The term was first used by Abraham Werner.[10] Graphite is often used as a dry lubricant, or as an electrode material due to its electrical conductivity. The material is mined in multiple locations around the world, with particularly high-quality graphite originating in Sri Lanka (up to 100 % carbon content).[8]

Diamond usually forms in a cubic structure, with each carbon atom covalently bonded to four other atoms (sp^3) in a tetrahedron. This structure results in a substantial thermal conductivity, but very low electrical conductivity rendering diamond an insulator. The name originates from the Latin *adamantem*, meaning "the hardest metal", and from the Greek *adamas*, meaning "unbreakable/unconquerable". Diamond is a highly valuable material both as a gemstone in jewellery, and in industry.[8]

Another allotrope of carbon is fullerene, named after Buckminster Fuller, an architect who designed geodesic dome structures with an appearance somewhat similar to the icosahedral C_{60} formation shown in Fig 1.1. C_{60} is comprised of carbon atoms arranged in the approximation of a sphere, 12 pentagons and 20 hexagons, not unlike the pattern of leather sewn on a football.[3] Although first identified through microscopy by a man called Sumio Iijima in 1980,[11] the discovery of fullerene is accredited to Kroto et al. for their work 5 years later.[12] They were awarded the Nobel Prize for Chemistry in 1996 for

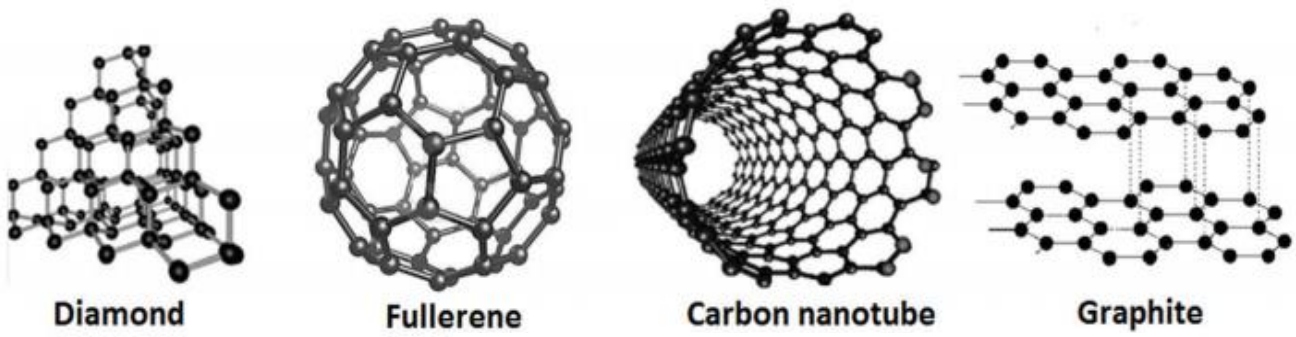

Figure 1.1: Allotropes of carbon. Adapted from [13].

this discovery. The isolation of this 0D particle heralded a surge in research towards carbon nanomaterials, which eventually led to the discovery of carbon nanotubes in 1991[11], and graphene in 2004.[1] Both materials feature prominently in the exfoliation of 2D materials and were used in the work described in this thesis.

Carbon nanotubes:

A carbon nanotube (CNT) is essentially a sheet of graphite that has been rolled up into a cylinder. The CNTs may be composed of one layer, in which case they are called single-walled CNTs (SWCNTs) or multiple layers (MWCNTs).[3] The cylindrical wall of the nanotube retains the 2D structure of the graphite sheet,[14] with each carbon atom covalently bonded to three neighbouring atoms. However, the tube in its entirety can be approximated as a 1D nanostructure given that its diameter is in the nanometre range, whereas the length of the nanotube can extend up to a few centimetres.[3] SWCNTs have been shown to have extraordinary mechanical properties, with tensile strengths up 100 GPa while being extremely lightweight. They also have exceptional thermal and electrical conductivities, but all these properties are affected by the constitution of the CNTs themselves (their diameter, length and configuration).[15]

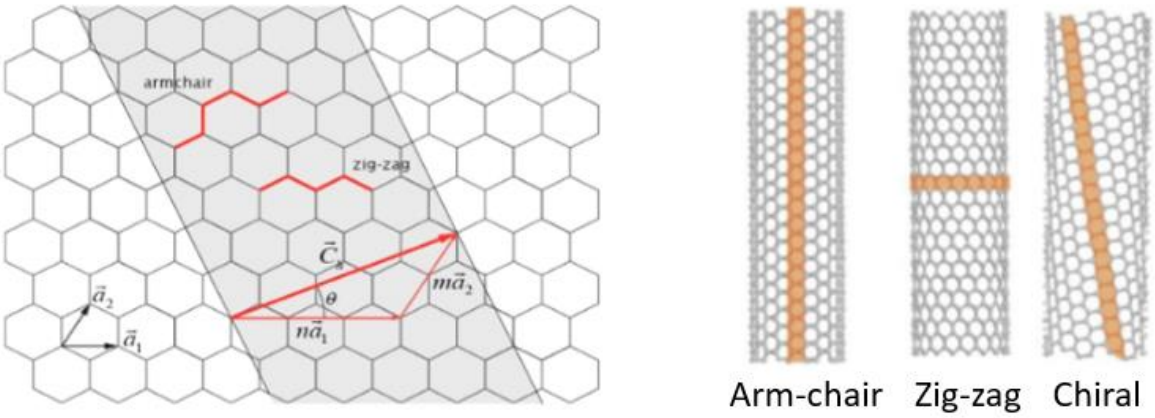

Figure 1.2: Different configurations of carbon nanotubes. Adapted from [15].

The helicity of the nanotube is the characteristic used to define the configuration. The chiral vector, C_h essentially represents the direction the nanosheet is rolled in the formation of the CNT i.e. it is perpendicular to the nanotube wall. This vector is defined using the unit vectors a_1 and a_2, and the integers n and m designate the magnitude of the vectors:[16]

$C_h = na_1 + na_2$

The configuration of the CNT in question is defined by n and m. A chiral nanotube is one for which n and m are not equal, with a chiral angle (θ) between 0 and 30 °. A zig-zag structure is observed when m=0 (θ = 0 °) and armchair when m = n (θ = 30 °). All armchair and some zig-zag nanotubes are metallic, with the remainder being semiconducting.[17]

A relationship between the chiral angle and (n, m) can be determined using trigonometry to give the following:[18]

$$\tan\theta = \frac{\sqrt{3}m}{2n+m}$$

In the work described in this thesis carbon nanotubes are added to dispersions prior to battery preparation to augment the electrical conductivity, with the added benefit of functioning as a mechanical binder.

Graphene:

In recent years, graphene has become the new face of the world of nanotechnology. Its successful isolation[1] along with the earlier discoveries of fullerenes and carbon nanotubes, has reinvigorated the field of carbon based material science. Graphene forms the building block from which these other carbon structures are formed, as depicted in Fig. 1.3.

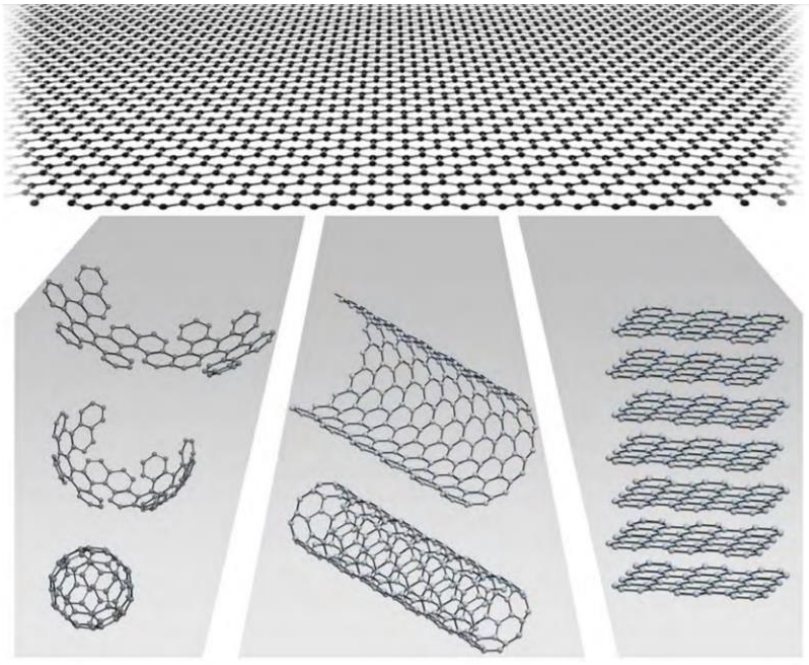

Figure 1.3: Graphene monolayer provides the building block for other carbon nanomaterials. Adapted from [19].

As discussed earlier, graphite consists of stacked planar carbon sheets in a honeycomb lattice. In 2004 Novoselov and Geim used mechanical cleavage with scotch tape to separate the individual graphite layers.[1] These monolayers are referred to as graphene and are composed of sp^2 hybridized carbon with each atom bonded to three neighbouring atoms. Three of carbon's four valence electrons are taken to form these bonds, leaving the fourth free to migrate within the plane of the lattice. These delocalized electrons give rise to the high carrier concentrations observed in graphene. This combined with the high electron mobility of the material makes graphene a potentially ideal candidate for transistor technology. However, graphene is a zero-bandgap semiconductor material which severely restricts the on/off ratio, and it is therefore problematic to incorporate into conventional device architecture.

The question of whether free-standing monolayer species could exist was disputed,[19] as theoretical analysis suggested the structure to be thermodynamically unstable. Modelling graphene as a completely flat atomic plane means that the atomic displacement caused by thermal vibrations would be sufficient to cause the nanosheets to break apart. Prior to the production of graphene investigations seemed to align with this theory. However, about 70 years later, Geim and Novoselev not only isolated the graphite monolayer, they also demonstrated rippling or 'crumpling' of graphene. This deformation suppresses the thermal vibrations, providing a form of self-stabilization.

After the successful exfoliation of graphene, it was immediately apparent that myriad other layered crystals could be exfoliated in a similar manner. In the years that have followed transition metal dichalcogenides (TMDs), boron nitride (BN), transition metal oxides, layered double hydroxides (LDHs), III-VI layered semiconductors, black phosphorus and many more besides have been shown to exhibit exceptional properties when successfully delaminated. Additionally, numerous methods of nanosheet production have been developed, as mechanical cleavage is a tedious and low-yield process.

Graphene was the first material delaminated using liquid phase exfoliation (LPE) in 2008.[20] It has been demonstrated that dispersions of graphene nanosheets can be stabilized against reaggregation in various dispersal media, including solvents such as n-methyl-2-pyrrolidone (NMP), n-cyclohexyl-2-pyrrolidone (CHP) or water-surfactant

solutions. These dispersions can easily be processed into films via vacuum filtration or spray coating.

It is important to note at this point that while graphene technically refers specifically to the monolayer, the same term is used generally in this thesis to designate dispersions of exfoliated few-layer graphite, which contain but are not solely composed of monolayers.

1.3 Molybdenum oxides:

Molybdenum is a component of many of the most widely studied layered materials, such as MoS_2 amongst the TMDs. Elemental molybdenum is a refractory material with a very high melting point and electrical conductivity. It is most commonly refined through the reduction of MoO_3, which occurs naturally in the form of molybdite. Mo gets its name from the Greek word, *molybdos*, meaning lead, as it was often mistaken for lead due to its similar appearance. Molybdenum is used in the alloying of steel to augment its strength and corrosion resistance.

One of the first families of layered materials explored after the initial focus on TMDs, BN and graphene were the transition metal oxides (TMOs). These are a versatile group of compounds consisting of a transition metal (such as Ti, Mo, Mn, W, Nb, Ru) and oxygen O_x where x is determined by the valence of the transition metal in a given TMO. The electronic properties of these materials vary significantly with metallic, semiconducting and insulating materials all represented within the grouping. The inconsistency of this behaviour is due in part to the differences in structure amongst the different TMOs, ranging from cubic to orthorhombic, monoclinic, tetrahedral and rutile configurations.

A given transition metal may form a variety of different oxides, depending on the valence state. These can exist naturally or have their structure altered in response to external stimuli. This can be seen in the case of oxides of molybdenum, as it can manifest in the form of MoO_3 (Mo(VI)), with an orthorhombic structure, that can be reduced to MoO_2, which has a distorted monoclinic structure (Mo(IV)). In addition to these there are at least six other Magneli phases formed during the reduction, of the formula Mo_xO_y, such as Mo_4O_{11}.

MoO_3:

Molybdenum trioxide (MoO_3) is a layered semiconductor material, blue in colour, with an orthorhombic structure. As mentioned previously it is important in the production of molybdenum metal but is also used extensively in energy storage devices such as fuel cells, lithium batteries and has been shown to have field emission properties. Another application is to aid the growth of Mo TMDs via chemical vapour deposition, where the MoO_3 can react with sulphur, selenium or any other appropriate precursor as required.

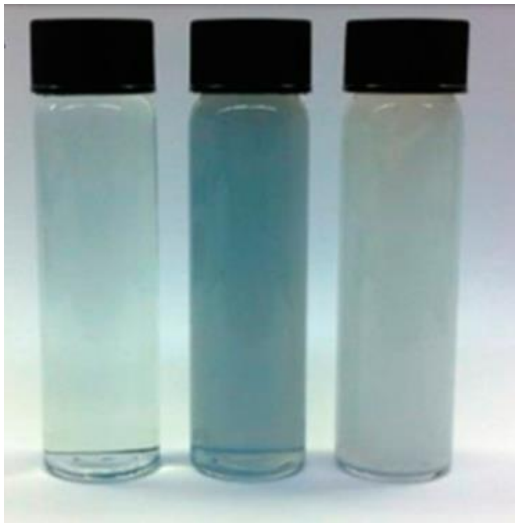

Figure 1.4: Dispersions of MoO_3 at various concentrations. [21]

Previous work in the Coleman group was carried out on the exfoliation of MoO_3 and its subsequent stabilisation in isopropanol (IPA).[21] Dispersions of MoO_3 were processed into films for use in supercapacitor technology, achieving specific capacitances as high as 350 F/g (0.1 mV/s). The success of this exfoliation project was important in that it was one of the first forays of liquid phase exfoliation beyond TMDs, BN and graphene, and proved that the technique could be readily applied to other families of materials without requiring any major changes to the methodology.

<u>MoO_2:</u>

Molybdenum dioxide (MoO_2) is a material which exhibits metallic electronic behaviour, with a low resistivity of 8.8×10^{-5} Ω cm.[22, 23] Compared with semiconducting MoO_3, it has a much higher conductivity and melting point. The crystal structure of MoO_2 is similar to the rutile configuration of TiO_2 but is distorted and consists of MoO_6 octahedra chained together. The metallic conductivity of the material arises from the bonding. Mo(IV) has a t_{2g}^2 configuration, but only one of the two d electrons is involved in the formation of the metal-metal bond. For a d^1 ion such as NbO_2 this would result in semiconductor behaviour, but in the case of MoO_2, the second d electron resides in a partially filled Mo-O pi bond.

MoO_2 is an attractive candidate for several applications due to its low toxicity, cost and relative abundance.[24] It is synthesized primarily via the reduction of MoO_3, but may also be generated using hydrothermal methods, thermal evaporation, CVD or electrodeposition from solutions.[25] Various nanostructures of MoO_2 have been reported, such as nano/micro spheres, nanorods and nanowires. Current applications include widespread use in catalysis for partial oxidation of hydrocarbons, fuel cells, electrode material for lithium ion batteries and in supercapacitors.[26] As with MoO_3, this material shows promise for field emission applications.[27]

The reduction of MoO_3 to MoO_2 is a multi-step process which can produce numerous intermediate species such as Mo_4O_{11}.

$$4MoO_3 + H_2 \rightarrow Mo_4O_{11} + H_2O$$
$$Mo_4O_{11} + 3H_2 \rightarrow 4MoO_2 + 3H_2O$$

Additionally, the oxidation process of MoO_2 in the temperature range 800 K – 900 K has been shown to produce Mo_4O_{11} and MoO_3:[28]

$$4MoO_2 + 1.5O_2 \rightarrow Mo_4O_{11}$$
$$Mo_4O_{11} + 0.5O_2 \rightarrow 4MoO_3$$

It is unclear whether the oxidation process behaves in a similar manner at room temperature or whether intermediate Mo_xO_y species are formed.

As part of the work described in this thesis a thorough exfoliation study of MoO_2 was carried out and the resultant nanosheet dispersions were processed into films for battery applications (Chapter 3).

1.4 Germanium sulfide:

In recent years phosphorene has generated great interest and exhibits potential for use in a multitude of applications. This material is composed of atomically thin nanosheets of black phosphorus (BP). As with other layered materials such as graphene or BN these sheets are held together via van der Waals forces, significantly weaker than the in-plane bonds.

Materials such as MoS_2 undergo major changes in properties after exfoliation. For example, the bandgap swaps from indirect to direct in the monolayer, ideal for electronics and optoelectronic applications. One issue hindering its use is the difficulty in achieving large quantities of monolayers, as the bandgap is sensitive to any increase in thickness. Phosphorene also has a direct bandgap in monolayer form but crucially, few-layer BP does too. This would suggest dispersions of BP in a suitable solvent could be utilized for implementation into various applications. Previous work in the group has shown that it is possible to both exfoliate BP and to stabilize it adequately against degradation. The material reacts readily with water or oxygen[29, 30] but using a solvent such as CHP or NMP protects the material due to the formation of a solvation shell. These results inspired the search for materials with a similar structure. To BP

The IV-VI semiconductor materials are a family of narrow bandgap compounds. Materials such as GeS, GeSe and SnS have a similar layer structure to BP[31, 32] and can therefore theoretically be exfoliated in the same manner. Chapter 4 of this thesis describes my work in exfoliating germanium (II) sulfide (GeS).

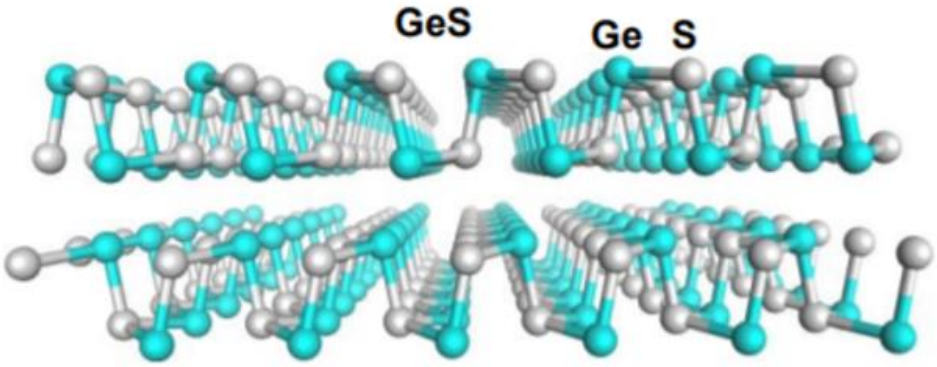

Figure 1.5: Structure of GeS monolayer. Adapted from [32].

GeS is a p-type semiconductor with an orthorhombic structure and is isoelectronic to phosphorene, with a reported electron mobility of up to 3680 $cm^2 V^{-1} s^{-1}$, which is higher than for MoS_2. This material has numerous direct and indirect bandgap transitions in the 1.5 – 1.65 eV range and exhibits high photoresponsivity, and so shows promise for applications in photodetectors or other photoelectronics.[32, 34]

GeS nanosheets can be produced using a broad range of techniques, such as mechanical cleavage from bulk,[33] wet chemical approaches,[35, 36] and has been exfoliated via ultrasonication in an inert environment.[37] It is generally accepted that the presence of water causes the material to hydrolize to produce germanium hydroxide ($Ge(OH)_2$) with the evolution of hydrogen sulfide (H_2S). Further reaction with water ultimately results in the formation of germanium oxide (GeO).[29, 30] This tendency to degrade in water suggests that exfoliation in ambient conditions would be difficult. However, this issue can be overcome in a similar manner to BP, using a suitable solvent to protect the nanosheets.

1.5 Methods of nanosheet production:

Mechanical cleavage (Scotch tape method):

When monolayer graphite (graphene) was first exfoliated in 2004[1], the nanosheets were produced using Scotch tape. The premise this technique is based upon is that the adhesive force from the tape is sufficiently strong to overcome the van der Waal's bonds between each of the

individual layers of the material, and they can therefore be separated from each other as the tape is peeled away. The procedure consists of placing the material to be exfoliated between two pieces of adhesive tape. The upper piece is then peeled away perpendicular to the direction

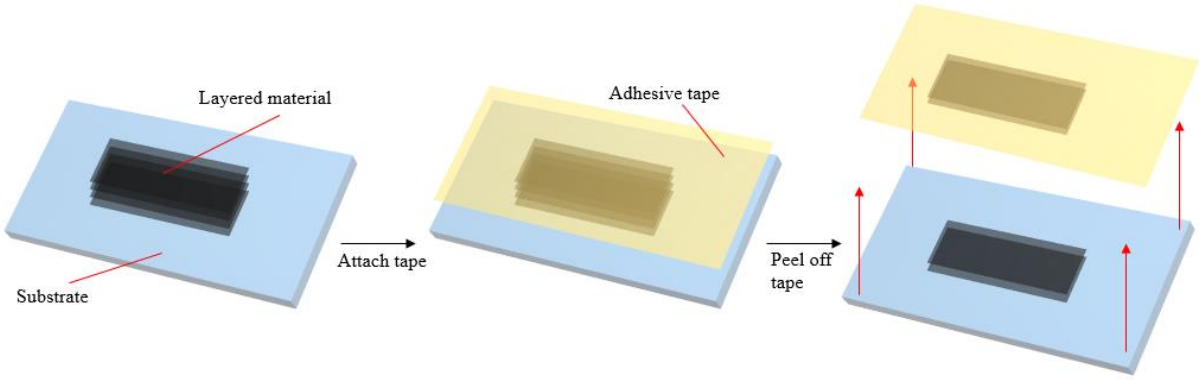

Figure 1.6: Mechanical exfoliation using the 'Scotch tape' method.

of the bottom piece of tape. This leaves two separate strips, each with some of the 2D material on them. Fresh scotch tape is attached to the material on one of these pieces and the process starts again. Through multiple iterations of peeling the material is reduced to a few layers or even monolayers, which can be transferred to a substrate such as silicon. Mechanical exfoliation in this manner remains arguably the best means to obtain high quality few-layer samples of 2D materials. However, the technique is time and labour intensive, with little opportunity for scalability. Despite extensive use in academic research, the scotch tape method has limited potential for industrial applications.

Intercalation:

Intercalation is an exfoliation technique whereby molecules can be adsorbed into the gap between layers, creating inclusion complexes. The adsorbed species increase the layer spacing, weakening the bonds holding the sheets together and facilitating exfoliation. This is generally achieved by sonication[38] or thermal shock[39] of the sample after intercalation. Both ionic and covalent intercalation compounds can be utilised. Using the former results in charge transfer between the material to be exfoliated and the intercalate. For example, Matte et al.[40] exfoliated MoS_2 and WS_2 by intercalation with lithium ions, and graphite has been intercalated with a variety of ionic species such as sulfuric acid, halogen intercalants[39] and tetraalkylammonium cations.[41] Alternatively, covalent compounds like graphite oxide[42, 43] can produce graphene by changing the hybridization of some of the carbon atoms from sp^2 to sp^3.

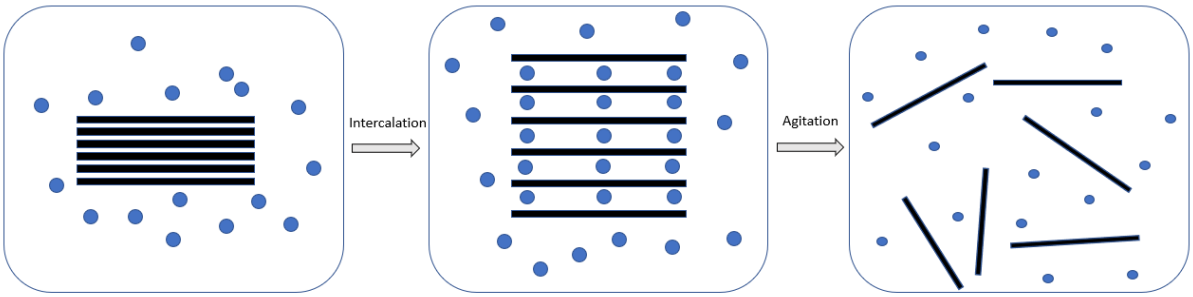

Figure 1.7: Mechanism of exfoliation via ion intercalation.

While intercalation has proven effective to delaminate many layered materials, there are several issues associated with this method. For instance, the intercalation process can alter the structure of the nanosheets or cause defects,[44] which may affect the properties of the material. The experimental set-up used often involves chemicals which are hazardous, or that may result in unwanted by-products. Additionally, the procedure is highly specific to the material to be exfoliated, with a significant degree of variation from one intercalation to the next. In this regard, intercalation is not as versatile as other exfoliation techniques.

Ion exchange:

This exfoliation method exploits the fact that certain 2D materials contain ions between sheets to counterbalance the charge of the layers. This technique is particularly effective for the delamination of layered double hydroxides (LDHs) and metal oxides.[45] The mechanism involves the exchange of ions from the interlayers with those from another species being introduced. The new ions modify the layer spacing - essentially swelling the nanosheets, which reduces the energetic input required to facilitate exfoliation. [46-50]

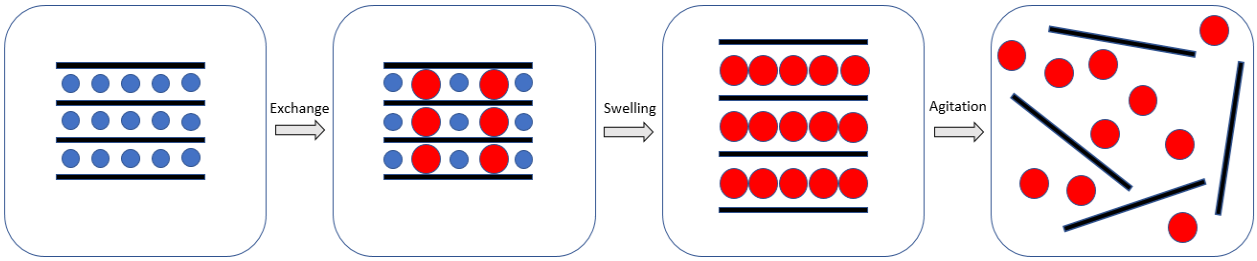

Figure 1.8: Mechanism of exfoliation via ion exchange.

Chemical vapour deposition (CVD):

CVD is a bottom up process whereby material is grown via deposition from vapour phase reactions. One or more precursors and/or catalysts react in a suitable environment, and material deposits on a substrate.[51-54] The temperature, pressure, choice of substrate and catalyst are variables that can influence the quality of the 2D materials produced. One of

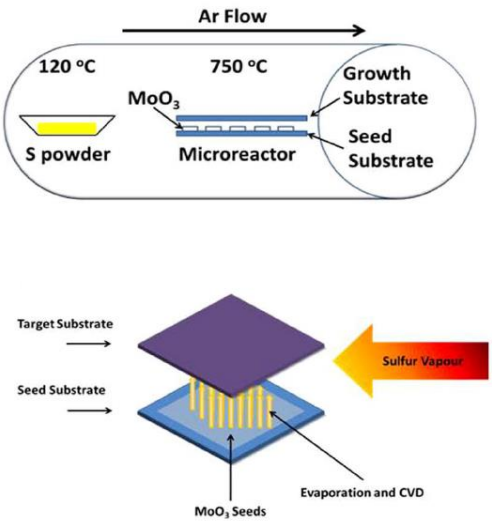

Figure 1.9: Preparation of molybdenum disulfide by chemical vapour deposition. Adapted from [50]

the key advantages of this technique is that the thickness of the films can be readily controlled and in a more uniform manner than many top-down delamination methods.

Wet-jet milling:

One of the more recent techniques which has evolved for exfoliating layered materials is wet-jet milling.[55-57] More commonly used in the fields of chemical engineering and food technology, this method has been adapted for producing high quality 2D crystal dispersions.[58, 59] The mixture of solvent and material is forced through a narrow region at high pressure and split into high speed jet streams which are made to collide together. The necessary pressure is supplied by a hydraulic piston system. The impacting particles and turbulent flow within the system results in the delamination of the nanosheets. This technique is promising in that the process is comparatively fast, producing exfoliated dispersions in a manner of minutes. However, increasing the number of piston passes to improve the degree of exfoliation may have a detrimental effect on the structural integrity of the nanosheets. In a similar manner to LPE, wet jet milling has the advantage that the process is largely independent of the material in question, with a solvent change being the only variable from one exfoliation to another.

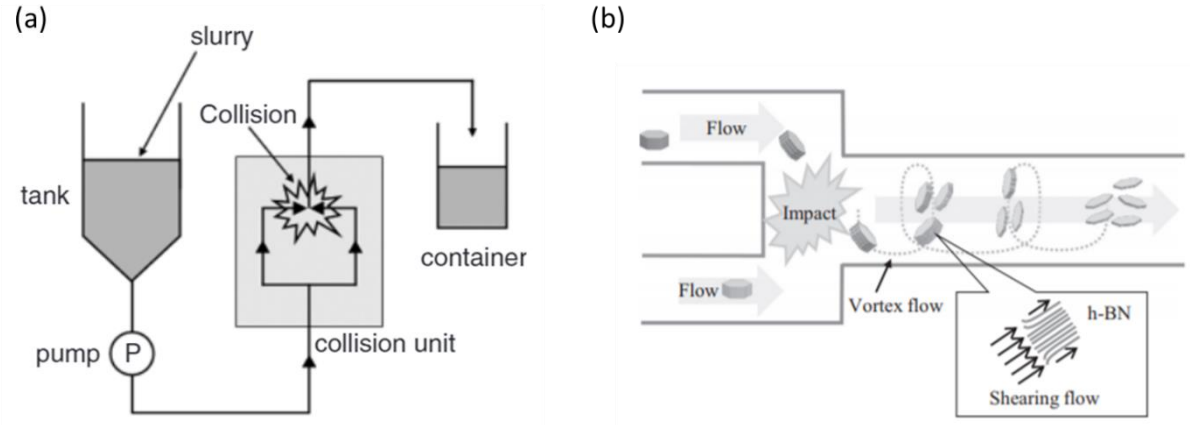

Figure 1.11: (a) Schematic describing WJM process. (b) Delamination of nanosheets after collision of jet streams. Adapted from [55] and [58] respectively.

Ball milling:

This method involves grinding the material to be exfoliated in a rotary mill. The cylinder contains spheres or ball bearings with a higher density than the material. As the container spins the friction between the material and the spheres cause shearing and subsequent delamination. The milling can be carried out in the presence of solvent[60] (wet milling) to stabilise dispersed material or other media such as dry ice.[61]

1.6 Liquid phase exfoliation:

Liquid phase exfoliation (LPE)[20] is a technique for delaminating layered materials. It is a relatively simple procedure, involving the application of ultrasonic or shear energy to a material dispersed in a stabilizing medium. During sonication, cavitation bubbles and high energy jets caused by the vibrations provide sufficient energy to overcome the interlayer van der Waals forces. A sonic bath or sonic tip can provide the necessary ultrasonic acoustic energy. Solvents such as NMP, water-surfactant mixtures and polymer solutions have all been used to stabilize nanosheets produced in this manner. Exfoliation using a solvent is dependent on the matching of solubility parameters. If there is a large discrepancy between the surface energies of the material and solvent the resulting dispersion will not be stable, leading to reaggregation of the nanosheets. Conversely, identifying and using a solvent with surface energy close to that of the material provides homogenous suspension of the material in dispersion.

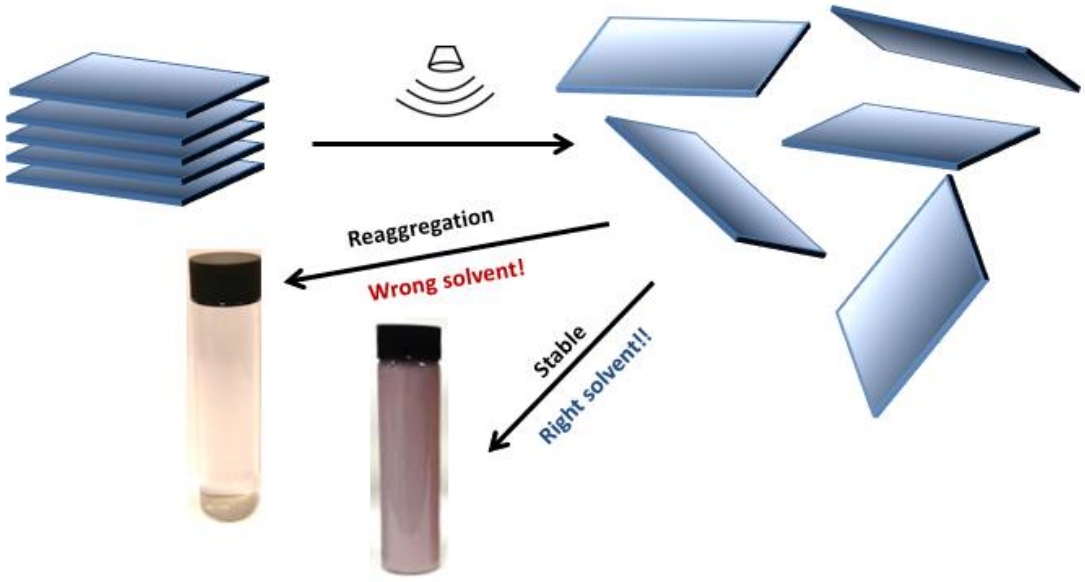

Figure 1.12: Liquid Phase Exfoliation proceeds via the application of ultrasonic energy to a layered material dispersed in a liquid medium. If a suitable solvent is chosen, the result is a stable dispersion. If not, then the nanosheets begin to aggregate almost immediately and sediment at the bottom of the vial.

Surfactant stabilization operates in a different manner. The water-surfactant solution is mixed with the material prior to sonication, and the surfactant molecules adsorb onto the surface of the nanosheets generated. This results in electrostatic repulsion of other similarly coated nanosheets, preventing them from interacting with each other. An

advantage of surfactant exfoliation is that the use of toxic solvents with high boiling points can be avoided. However, a washing step is often necessary to remove residual surfactant after exfoliation, which can cause loss in mass and therefore a reduced efficiency. It is also difficult to estimate the amount of surfactant which remains present on the nanosheets.

LPE is a versatile technique, which can be applied to new materials with very little changes necessary to the exfoliation protocol. A broad range of materials have been exfoliated using this method to date, such as graphene[20, 62-64], BN[65-67], GaS[68, 69], TMDs (MoS_2[70-72], WS_2[73, 74], $MoSe_2$[75, 76], etc), LDHs[77] ($Ni(OH)_2$[78], $CO(OH)_2$[79, 80]), BP[81, 82], MoO_3[21, 83], MoO_2[84], antimonene[85] and TiS_2[86]. Beyond these conventional materials it has also been shown that LPE can be used to produce nanosheets from samples containing a mixture of species, some of which may not even be layered. A. Harvey et al.[87] demonstrated that the layered species in clay, talcum powder and cat litter could be successfully delaminated using a series of cleaning steps to remove impurities. More recently, work by Kelly et al.[88] has shown that LPE can delaminate and stabilize nanosheets even when using solvents of inferior quality to lab-grade.

The high tensile and shear stresses caused by the implosion of cavitation bubbles during ultrasonication not only overcomes the interplanar van der Waals forces, but also causes fragmentation of the atomic planes. Consequently, the resultant dispersions are typically polydisperse, containing nanosheets with a broad range of lengths and thicknesses. They are also primarily composed of few-layer nanosheets with only a small quantity of monolayers. Enrichment using iterative centrifugation steps can improve the monolayer content.

Depending on the desired application, flakes of a specific size may be preferable. For example, smaller nanosheets with higher surface area are ideal for catalysis, while larger flakes perform better for mechanical reinforcement. It was necessary therefore to develop a means to exert control over the size of the nanosheets produced by isolating all material with similar dimensions into distinct size fractions. This can be achieved using controlled centrifugation conditions.

1.7 Size selection:

One of the major advantages of LPE is the ability to influence the size of the flakes present in a given exfoliated sample. Below are two methods used to segregate the material in dispersions into discrete fractions based upon size.

Density Gradient Ultracentrifugation (DGU):

DGU exploits the fact that polydisperse suspensions contain material with a range of buoyant densities. Adding the dispersed material to an aqueous solution with a density gradient creates an almost tiered system where material can sediment at the isopycnic point (where the density of the solution matches its own).[89, 90]

Creating an aqueous solution using a compound with a higher density than water allows for a linear density gradient to be easily produced by controlling the concentration. DGU has been used extensively in the pharmaceutical industry but it was first applied to 2D nanomaterials by Hersam et al.. Injecting the dispersion into the density gradient and subjecting the entire ensemble to ultracentrifugation causes the material constituents to sediment at their respective buoyant densities. In this way monolayers, bilayers, trilayers etc can be effectively segregated from each other and removed independently.[91-93]

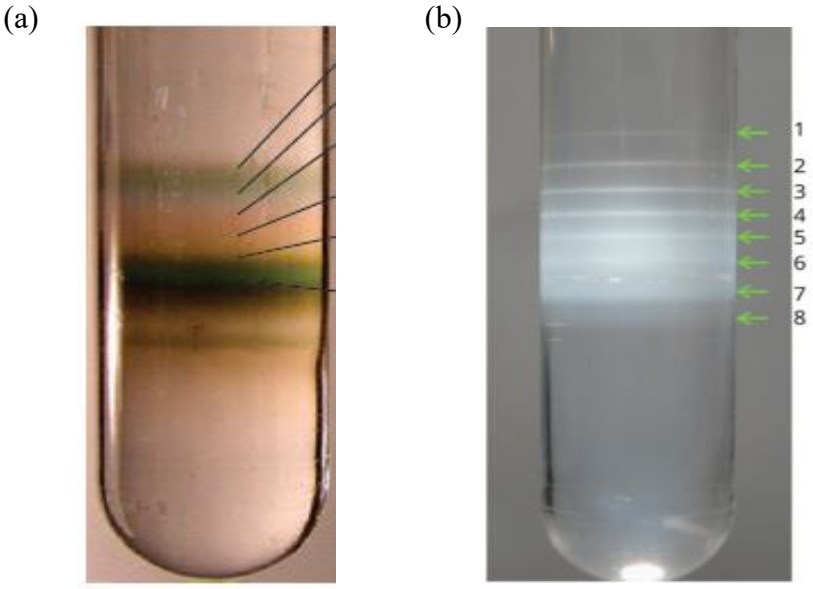

Figure 1.10: Production of (a) SWCNTs, and (b) h-BN by density gradient ultracentrifugation. Adapted from [88] and [89] respectively.

Liquid Cascade Centrifugation (LCC):

Liquid cascade centrifugation (LCC)[94], is a procedure which comprises a series of centrifugation steps, each of higher speed than the last. Initially the dispersion is subjected to low speed centrifugation to cause any unexfoliated material to sediment out. This material is discarded after decanting the supernatant (the remaining liquid), which is immediately centrifuged at a higher speed. After this step the sediment is retained, designated as the largest nanosheet size present in the original dispersion. This sediment can be redispersed in fresh solvent to any desired concentration with mild agitation in a sonic bath and represents a distinct size fraction with reasonably uniform nanosheets in terms of length and thickness. Repeating this process of increasing centrifuge speed, decanting supernatant and retaining the sediment, a range of samples are produced in descending order of nanosheet size. Statistical analysis from TEM measurement can provide the average lengths of the nanosheets in each sample. A schematic representation

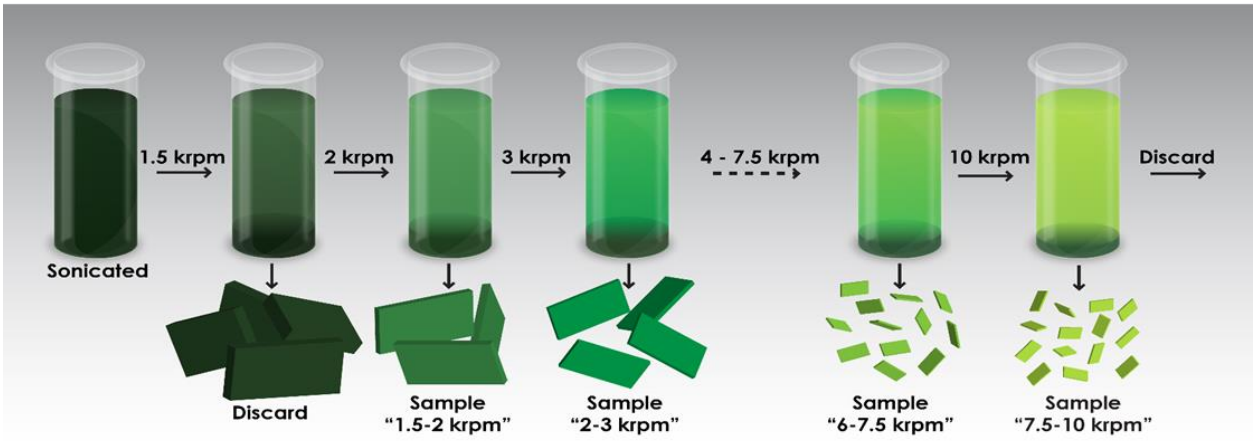

Figure 1.13: Size selection via liquid cascade centrifugation.

of the LCC procedure is featured in Fig 1.13.

LCC has multiple advantages over other means of size selection. It is highly versatile in that the size, thickness and (to an extent) the monolayer content can be controlled. Additionally, this technique has a very high yield with minimum wastage of material, and each individual size-selected sample can be redispersed to any desired concentration.

1.8 Thermodynamics of stabilization:

The selection of an appropriate dispersal medium is an essential part of the exfoliation process. In order to choose the best candidate, it is necessary to understand the thermodynamics governing all interactions between the solvent and material. This is defined by the Gibbs free energy of mixing:

$$\Delta G_{mix} = \Delta H_{mix} - T\Delta S_{mix} \qquad 1.1$$

Here ΔG_{mix} is the Gibbs free energy of mixing, ΔH_{mix} and ΔS_{mix} are the enthalpy and entropy of mixing respectively, and T is the absolute temperature. In order for mixing to be favourable, the Gibbs free energy needs to be negative.[95-97]

Entropy of mixing:

The entropic component describes the change in disorder from the separate individual components (solute and solvent), and the combination of the two after mixing. Consequently, the entropy of mixing is always positive.[97]

Consider a binary mixture composed of species x and species y. The entropy of mixing ΔS is the difference before and after mixing, given by the following equation:

$$\Delta S = S_{x+y} - \left(S_x + S_y\right) \qquad 1.2$$

The entropy can be described in terms of the number of accessible states ω via Boltzmann's equation $S = k_B \ln \omega$. For a molecule x, ω =N_x, the number of x particles. The entropy per molecule in its unmixed state is therefore given by $s_x = k \ln N_x$. However, after mixing this same molecule has more accessible states available $s_x = k \ln\left(N_x + N_y\right)$. Therefore, the difference in entropy before and after mixing for the molecule is:

$$\Delta s_{mix,x} = k \ln\left(N_x + N_y\right) - k \ln N_x = k \ln\left(\frac{N_x + N_y}{N_x}\right) \qquad 1.3$$

The volume fraction for molecule x is defined as follows: $\phi_x = N_x/N$, where $N = N_x+N_y$. Inserting the volume fraction into equation 1.3 gives:

$$\Delta s_{mix,x} = k \ln \frac{1}{\phi_x} = -k \ln \phi_x \qquad 1.4$$

Extrapolating this to all molecules, the entropy of mixing for the mixture is described by the following equation:

$$\Delta S_{mix} = N_x \Delta s_{mix,x} + N_y \Delta s_{mix,y} = -k\left[N_x \ln \phi_x + N_y \ln \phi_y \right] \qquad 1.5$$

From earlier we know that $\phi_x = N_x/N$ so we can rewrite equation 1.5 in terms of N:

$$\Delta S_{mix} = -kN\left[\phi_x \ln \phi_x + \phi_y \ln \phi_y \right] \qquad 1.6$$

Rewriting the entropy on per-molecule basis:

$$\Delta \bar{S}_{mix} = \frac{\Delta S_{mix}}{N} \rightarrow \Delta \bar{S}_{mix} = -k\left[\phi_x \ln \phi_x + \phi_y \ln \phi_y \right] \qquad 1.7$$

This relationship describes a mixture of two components, x and y. If one now considers a liquid phase exfoliated mixture consisting of nanosheets and a suitable solvent, the material volume fraction is given by ϕ and the solvent volume fraction is written as (1-ϕ). The above equation then becomes:

$$\Delta \bar{S}_{mix} = -k\left[(1-\phi)\ln(1-\phi) + \phi \ln \phi \right] \qquad 1.8$$

In the case of large rigid particles like carbon nanotubes, the entropy of mixing is very small.[96] As such, in comparison to enthalpy, entropy is hardly considered to be a factor in choosing energy efficient solvents. Therefore, in order to fulfil the criteria for a Gibbs free energy conducive to mixing, it is paramount to minimize the enthalpic component. While it is true that the enthalpy of mixing is vital to the choice of dispersal medium, recent work has shown that the assumption that entropy is too small to impact on the free energy of mixing is perhaps misleading. [98]

Enthalpy of mixing:

The enthalpy of mixing describes the energetic cost of separating solvent and solute molecules, minus the energy from surrounding the nanosheets with solvent molecules. A number of different solubility parameters have been proposed to describe this quantity. An early model was developed relating the enthalpy of mixing ΔH_{mix} per volume of mixture to surface energies:[95, 97, 99]

$$\frac{\Delta H_{mix}}{V} = \frac{2}{T_M}\left(\sqrt{\gamma_s} - \sqrt{\gamma_M}\right)^2 \phi \qquad 1.9$$

γ_S and γ_M are the surface energies of the solvent and dispersed material respectively. T_M is the thickness of the nanosheets and ϕ is the volume fraction of the dispersed material. It is evident from this model that the enthalpy of mixing is at a minimum when a solvent with surface energy close to the material is chosen.[99]

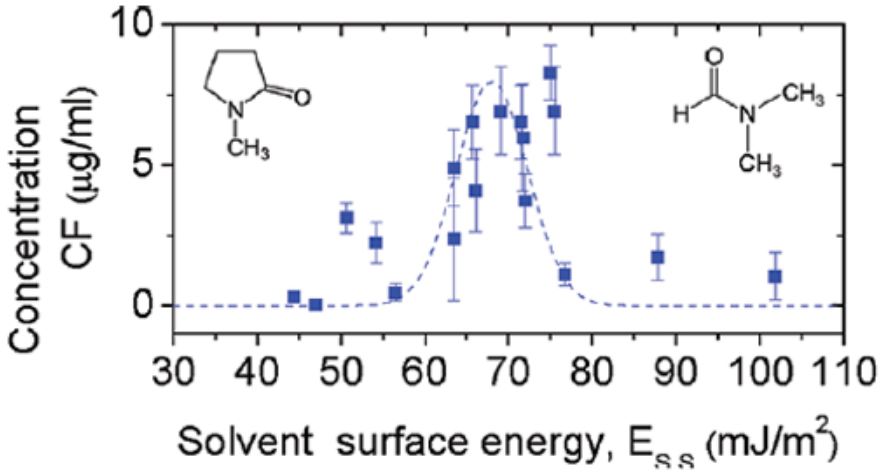

Figure 1.14: Dispersed concentration plotted versus solvent surface energy. Adapted from [99].

Fig 1.14 shows the variation in dispersed concentration with different solvents ranging in surface energy. While providing a good approximation, surface energy is not an ideal means to predict solvent quality regarding capacity for exfoliation. As a solubility parameter, it is rather crude, and often results in concentrations lower than would be expected.[99, 100]

Before the enthalpy of mixing is discussed in more detail it is necessary to introduce Flory-Huggins theory.

One must consider the solvent-solvent and solute-solute interactions in addition to those of the solute and solvent.[101] The strength of the solute-solvent interaction relative to the inter-solvent and inter-solute interactions is of utmost importance. If the solute is attracted to other material more strongly than to the solvent, there will be an energetic tendency towards aggregation and therefore sedimentation of the material. On the other hand, if the solute-solvent interaction is strong there will be an energetic cost in bringing the nanosheets together, facilitating the material to remain uniformly dispersed. The balance of these interaction energies can be described by the Flory-Huggins parameter, χ:[101]

$$\chi = -\frac{z}{2}\frac{\left(2\varepsilon_{AB} - \varepsilon_{AA} - \varepsilon_{BB}\right)}{kT} \qquad 1.10$$

This expression assumes very similar volumes for solute and solvent molecules i.e. very small molecules. *z* denotes the coordination number of the solute/solvent and ϵ represents the strength of the inter-molecular pairwise interaction energies. A and B refer to the solute and solvent respectively. If χ is negative, interactions between the solute and solvent dominate. If it is positive, the solute molecules have increased attraction to each other over the solvent and the material will reaggregate. Describing the enthalpy of mixing in terms of the Flory-Huggins parameter we get the following expression:

$$\Delta H_{mix} = \chi\phi\left(1-\phi\right)\frac{kT}{v_0} \qquad 1.11$$

Here ϕ is the solvent volume fraction and v_0 is the solvent molecular volume.

One of the early pioneers of solubility theory was Hildebrand, who recognized that for molecular solutes the solubility is related to the cohesive energy density. The Hildebrand solubility parameter, δ, is defined as the square root of the cohesive energy density (CED)[102], where the CED is given by:

$$\Delta E_c = -\frac{z\frac{\varepsilon}{2}}{v_0} \qquad 1.12$$

Using this relation, it is possible to rewrite the Flory-Huggins parameter in terms of the solubility parameters of the solute and solvent:[99]

$$\chi = \frac{v_0}{kT}\left(\delta_A - \delta_B\right)^2 \qquad 1.13$$

While functioning as a superior alternative to surface energy, the Hildebrand solubility parameter also occasionally results in concentrations lower than expected.

Hansen further developed upon the work of Hildebrand by suggesting that the solubility parameter could be divided into distinct contributions from several individual parts. These are defined by the types of interactions that a material may experience: dispersive (δ_D), polar (δ_P), and hydrogen bonding (δ_H).[99]

Dispersive (δ_D): Non-polar interactions experienced by all molecules deriving from atomic forces.

Polar (δ_P): Dipole moment is the primary parameter used to calculate these interactions, stemming from dipole-dipole interactions.

H-bonding (δ_H): Attractions between molecules based on hydrogen bonds. Loosely used as an umbrella term for all interactions not encompassed within the dispersive or polar contributions.

The Hildebrand solubility parameter is equal to the square root of the sum of the squares of the three different Hansen solubility parameters:[102, 103]

$$\delta_T{}^2 = \delta_D{}^2 + \delta_P{}^2 + \delta_H{}^2 \qquad 1.14$$

The Flory-Huggins parameter can be expressed in terms of the individual interaction energies:

$$\chi = -\frac{v_0}{kT}\left[\left(\delta_{DA} - \delta_{DA}\right)^2 + \left(\delta_{PA} - \delta_{PB}\right)^2 + \left(\delta_{HA} - \delta_{HB}\right)^2\right] \qquad 1.15$$

It is evident from Equations 1.13 & 1.15 that making the difference between the solubility parameters as small as possible will provide the lowest value for the Flory-Huggins parameter. This in turn minimizes the enthalpy of mixing, resulting in a stable dispersion. It is usually sufficient to identify solvents with a similar Hildebrand solubility parameter but for optimal exfoliation it is necessary to match all three Hansen parameters.

This analysis forms the basis of the approach to selecting the optimal solvents for exfoliating the materials examined in this thesis. Having access to databases with solubility parameters implies that a screening process can be applied to quickly identify the range of solvents for which dispersions of high concentration and stability can be consistently produced.

2

Materials & methods

2.1 Introduction:

In order to be able to study these materials and take advantage of their incredible properties, it is necessary to have the ability to control their production. Within the framework of LPE, the two steps which control this production are sonication and centrifugation. Sonication provides the necessary energy to delaminate the material and the conditions under which it is carried out determine the stability and concentration of the resulting dispersion. Centrifugation extracts the unexfoliated material and can be utilized to partition the dispersion into distinct size fractions. It is therefore possible using LPE to exert a level of control on the concentration and nanosheet size of a given material dispersion and tailor these parameters to fit the desired application. For example, a dispersion containing small flakes would be ideal for catalysis applications, whereas longer nanosheets would be well suited to use in mechanical reinforcement. One of the many advantages of LPE is its versatility. This procedure can be applied to virtually any layered material, with only a few changes in the sonication and centrifugation parameters required for optimization. The results of such optimizations are reproducible nanosheet dispersions easily processable into composites, films and devices.

Having produced a liquid exfoliated dispersion, it is vital to be able to characterize the nanosheets contained within the sample. Microscopy techniques such as SEM, AFM and TEM provide information on the appearance of the flakes, while also allowing their lengths and thicknesses to be determined. Spectroscopic methods including Raman, UV-vis and XPS give insight into the optical properties and composition of the material.

In this chapter all of the methods used to successfully exfoliate 2D materials during this work will be discussed in detail, both the techniques themselves and their role in characterizing liquid phase exfoliated nanosheets.

Unless otherwise stated, all materials used in this work were purchased from Sigma Aldrich and received in the form of fine powder. Material in compacted solids or aggregates is ground to a powder with a pestle and mortar prior to exfoliation.

For the purposes of this thesis ‘ambient conditions’ refers to full exposure to air and no temperature regulation.

2.2 Sample Preparation:

Sonication:

As mentioned previously, sonication i.e. the exposure of the layered material to ultrasonic energy, is a fundamental part of LPE. The mechanism of exfoliation is acoustic cavitation, which involves the implosion of bubbles in the solvent. The ultrasonic vibrations cause the growth and propagation of both newly formed and existing microbubbles, which oscillate in response to the applied high amplitude waves. Growth of the bubbles is facilitated in the areas of negative pressure of the acoustic field and they are compressed and shrink in the regions of positive pressure. Fig. 2.1 shows a schematic for this process. This repeated expansion and contraction of the bubbles eventually results in their collapse, and the implosion generates high-speed jets. The shock waves are intense enough to overcome the interlayer forces between the planes of the material, and the nanosheets are forcibly separated. During the collapse of the bubble it experiences intense heating and extreme pressure over a period of a few microseconds.[104-110]

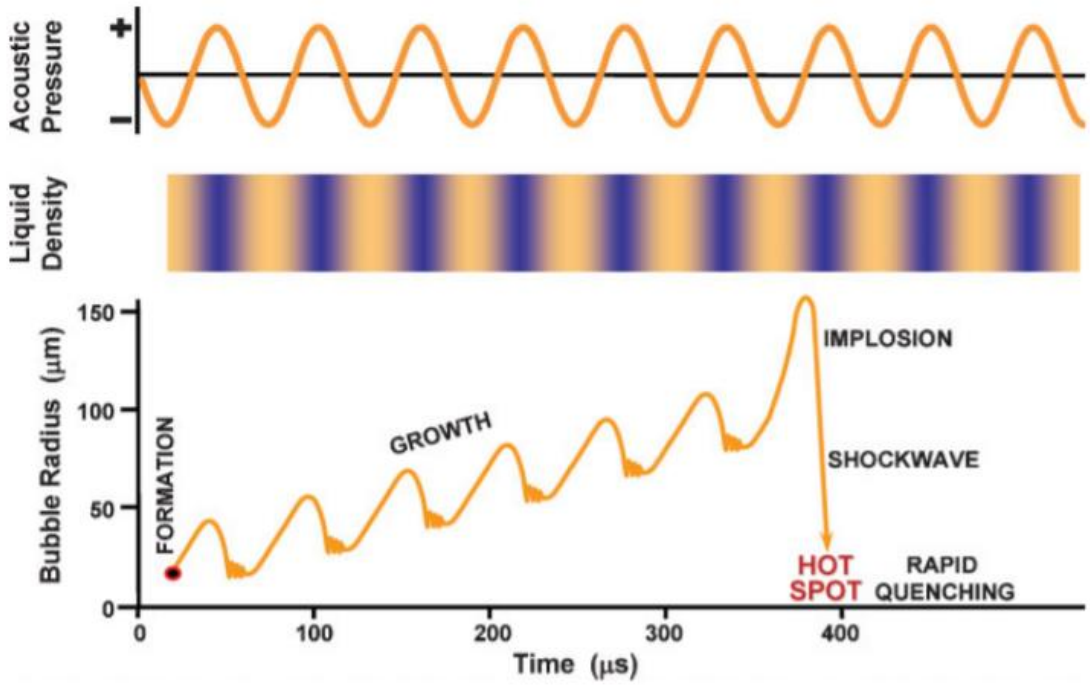

Figure 2.1: Mechanism describing the formation, growth and implosion of cavitation bubbles. [106]

There are two main methods for applying the required sonic energy, a sonic bath or a sonic probe (tip) inserted into the solvent-powder mixture. In the case of the former, the sample is inserted in a beaker of water, which is placed in the sonic bath, and so receives the sonic energy second-hand through the water in the beaker, whereas in tip sonication the energy is imparted directly to the sample. As a result, the energy input is higher and more localized, and so could be considered a more aggressive exfoliation method than bath sonication. For these reasons the tip usually causes increased fragmentation of the nanosheets,[111] producing flakes with a smaller size distribution when compared to samples exfoliated in a bath. An issue with the use of baths is that the distribution of localized hot spots is generally not uniform across the area and so rotation of the samples in the bath is required to alleviate this problem somewhat. In general, tip sonication is preferable to bath sonication for exfoliating layered materials because it gives an increased concentration in a given exfoliation time, but in some cases the bath sonication approach provides better results.[68] For the work described in this thesis, the exfoliation was carried out using a sonic tip, and bath sonication was used exclusively for redispersal of sediment in fresh solvent after centrifugation.

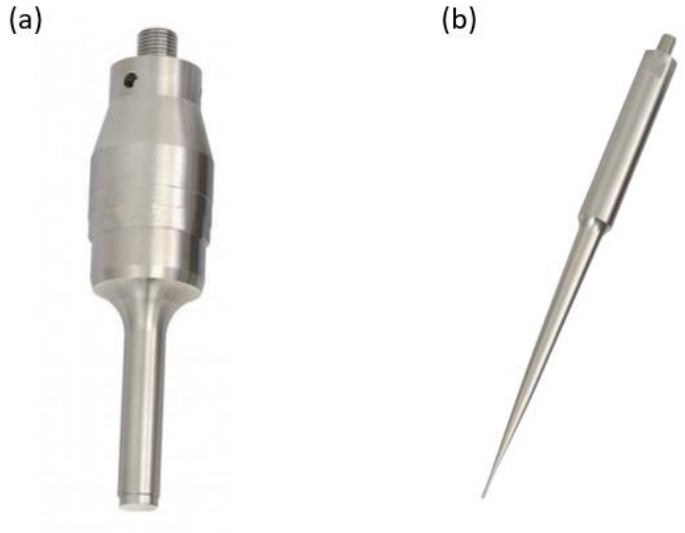

Figure 2.2: Sonic tips: (a) Horn probe, (b) Tapered

For standard dispersions of 80 mL, sonication is performed using a horn probe tip as shown in Fig. 2.2(a). The tip is lowered into an aluminium vessel containing the solvent-powder mixture and secured 1 cm above the bottom of the vessel. The sonication is

usually carried out at 60 % amplitude and a pulse rate of 6 s on 2 s off, with constant cooling to reduce heating of the sample. A higher amplitude would result in the degradation of the tip with frequent use. The cooling system involves a jacketed beaker around the sonication vessel, through which chilled water is circulated.

When dispersions of a smaller volume are required sonication instead uses a tapered tip, as shown in Fig 2.2(b), which is inserted into a glass 28.5 mL vial containing the sample. The minimum volume feasible for sonication in this manner is 15 mL.

While it is true as a general rule that longer sonication times result in higher concentrations, shorter processing times are preferable. Extended periods of sonication can cause damage to the sonication unit or result in heating of the dispersion and negatively influence the material properties. For example, in the case of materials that tend to oxidize in ambient conditions it can be prudent to expedite the sonication step to minimize the processing time from powder to exfoliated nanosheets. For these reasons, sonication times of less than 8 hours are usually opted for. In a similar manner to lengthening the sonication time, increasing the starting concentration of powder in the dispersion will result in a higher concentration of the sample after exfoliation. It is often a case of diminishing returns however with the economic ramifications needing to be considered. When exfoliating a new material for the first time it is necessary to do a comparative study to examine the effects of adjusting these parents so that optimal conditions for sonication can be determined.

Centrifugation:

One of the major disadvantages of exfoliating layered materials using sonication is that the resultant dispersions are polydisperse, containing nanosheets with an assortment of sizes and thicknesses. Additionally, a portion of the material may remain unexfoliated, and jeopardize the stability. In order to overcome these issues dispersions are subjected to a process called centrifugation.

If you consider one of these polydisperse samples, the size discrepancy of the flakes means that there is a mass difference also. By placing the sample in a centrifuge and spinning at high speed a strong centripetal force is generated, which causes the denser material to be pulled down towards the bottom of the vial. In this way the sample can be

separated into sediment (material that settles out of dispersion) and supernatant (the solvent and any remaining dispersed material), as shown in Fig 2.3.

The largest particles i.e. the unexfoliated material will sediment[112, 113] out first, followed by the larger (and generally thicker) nanosheets. High rpm is often required to remove the smallest of the nanosheets present. In order for the sample to continue travelling in a circular direction in the centrifuge, a continuous centripetal force must be applied perpendicular to the direction of motion (as shown in Fig 2.4), which is balanced by the centrifugal force.

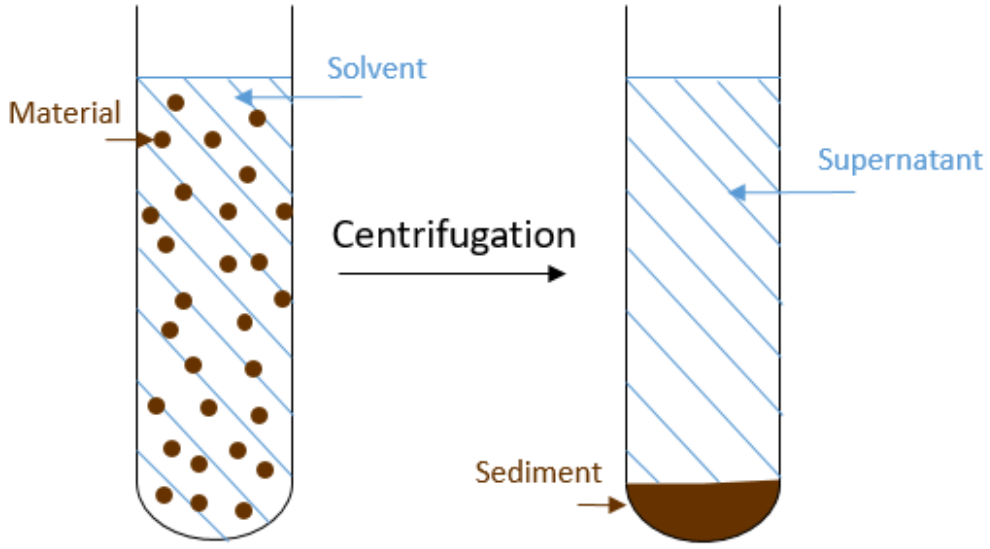

Figure 2.3: Sedimentation of material via centrifugation.

The magnitude of this force is given by:

$$F = \frac{mv^2}{r}$$

where the mass of the sample is m, *v* is its speed, and r is the distance from the sample to the center of rotation, which is approximately equal to the radius of the rotor. It is important to note that the force increase with the square of the speed of rotation, which means a tenfold increase in rpm (from 500 to 5000 rpm for example) results in an increase in force by a factor of 100.

For dispersions produced by LPE to be stable, a combination of the correct dispersal medium and sedimentation of unstable species by centrifugation is necessary. The importance of solvent selection was discussed previously, in section 1.7.

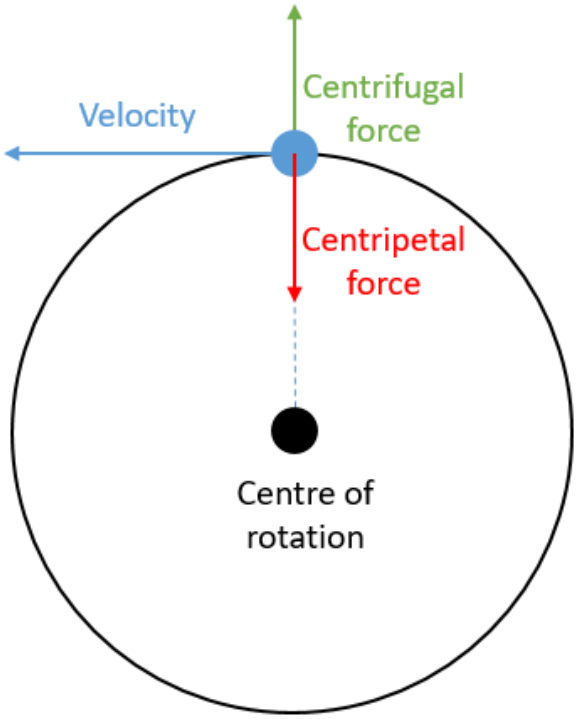

Figure 2.4: Forces acting on a body under circular motion.

Film Preparation:

A significant advantage of LPE is that dispersions of layered materials can be easily processed into films via vacuum filtration, which is ideal for some methods of characterization. Additionally, these films provide a convenient starting point for applications testing such as batteries. Prior to filtration carbon nanotubes can be added to function as a conductive additive and mechanical binder simultaneously. Using vacuum filtration of samples with known concentration allows the thickness of the film to be carefully controlled. When dry, these films can be cut to the desired size and shape.

In general filtration is carried out using nitrocellulose membranes. After a film has been created on the membrane, the nitrocellulose can be removed through dissolution with acetone. This process is shown in Fig. 2.5.

The film is placed material side down on a desired substrate to replace the nitrocellulose, such as a glass slide or copper foil in the case of battery applications. Wetting the back of the film with isopropanol (IPA) while pressed against the chosen substrate is sufficient to facilitate adhesion. Exposing the nitrocellulose to acetone vapour followed by repeated steps of immersion in an acetone bath ensures that all the nitrocellulose has been removed, and the material isolated on the substrate.

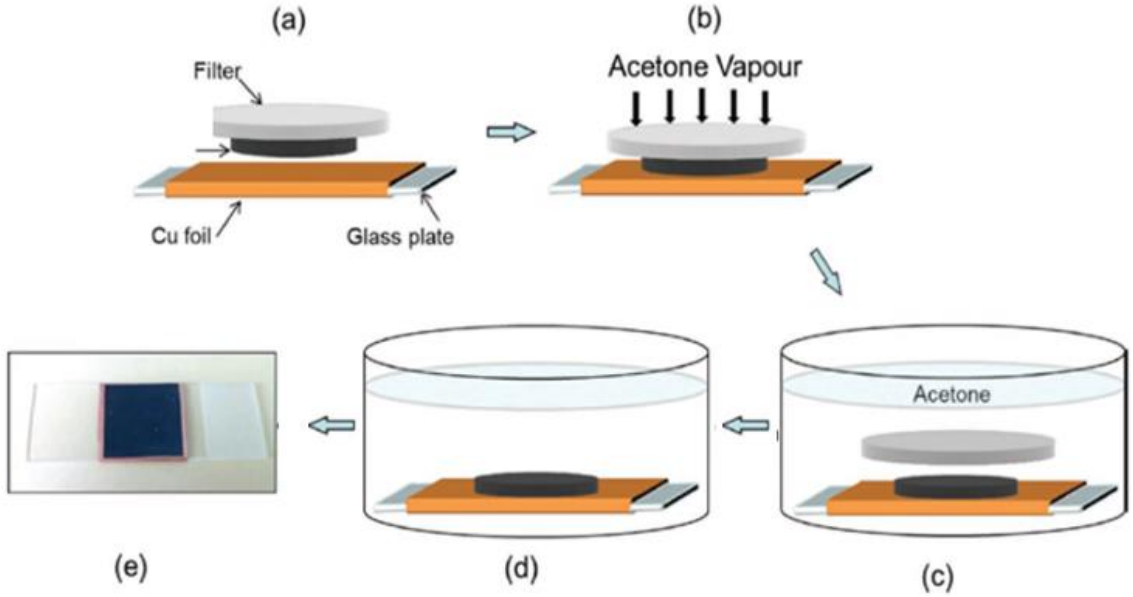

Figure 2.5: Procedure for transferring films from filter membranes.

Alternatively, LPE dispersions can be processed into films using ink-jet printing[114] or spray-coating using an airbrush. Samples in low boiling point solvents such as isopropanol or water are particularly well-suited to spray deposition. A backpressure of nitrogen allows the dispersion to be atomized at the nozzle of the airbrush, which is mounted onto a stage with a programmable movement pattern. The airbrush deposits the material through a continuous raster process, which can be repeated for as many passes as needed to achieve the desired film thickness. The nozzle diameter controls the rate of deposition and limits the dimensions of nanosheets possible for spraying.

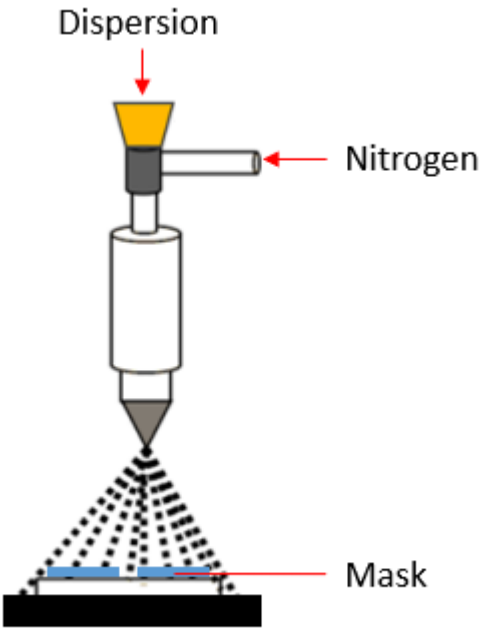

Figure 2.6: Spray deposition of a dispersion via airbrush. Adapted from [114].

This is an effective means of film formation but there is an inherent lack of precision in the spraying process. Given the continuous nature of the stream from the airbrush as it moves, it is necessary to mask the substrate if a specific pattern is required. As a result, a significant amount of material is wasted. This can be problematic when dealing with low quantities of starting material which can yield dispersions of low concentrations.

2.3 Characterization:

UV-vis Spectroscopy:

Optical absorption spectroscopy provides a means to analyze the interaction of light with sample dispersions, or more specifically, the nanosheets suspended in a given dispersion. When

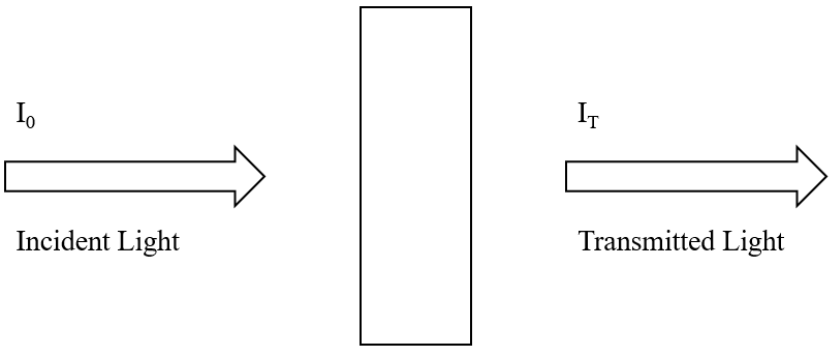

Figure 2.6: Transmission of light incident on a medium.

light travels from one medium into another, the incident intensity (I_o) can be attenuated through absorption by the medium (I_A) or scattered by suspended particles (I_s). The beam which emerges after passing through the medium is the transmitted light (I_T). The sum of these intensities must equal the intensity of the incident beam.

$$I_0 = I_A + I_T + I_S$$

For now we shall ignore the contributions from scattering and focus on the relationship between the absorbed and transmitted light. Transmittance (T) is the ratio of the amount of light transmitted by or passing through the sample relative to the incident beam.

$$T = \frac{I_T}{I_0} = \frac{intensity\ of\ transmitted\ light}{intensity\ of\ incident\ light}$$

The absorbance (A) of the sample is defined as the negative logarithm of the transmittance (T) i.e. the absorbance and transmittance are inversely related. It stands to reason that the more light absorbed by the medium, the lower the amount of light transmitted.

$$A = -\log(T) = -\log\left(\frac{I_T}{I_0}\right)$$

Consider a vial containing a solvent such as water. If one adds a small amount of soluble material that absorbs in the visible range you will notice that the resulting solution remains transparent, but displays the same colour as the solute which has been dissolved. Adding more solute increases the concentration of the solution, and in doing so the transparency is reduced. If sufficient solute is added the solution becomes opaque in the visible range. We can interpret from this that the higher concentration of the solution has increased the absorption and thus reduced the amount of light being transmitted. Similarly, the absorption is related to the path length i.e the distance through the medium the light travels. The relationship between the absorbance, concentration and path length for dilute solutions and suspensions is described by the Beer-Lambert (BL) law:

$$A = \alpha c l$$

where A is the absorbance, α is the absorption coefficient of the material, c is the concentration and l is the path length. At high concentrations the absorption bands will saturate, and the BL law may no longer hold, therefore it is imperative that the sample is diluted sufficiently before measurement is attempted.[116]

Using a quartz cuvette with a known path length it is possible to identify the absorption coefficient for a given wavelength if the concentration is known. Alternatively, the

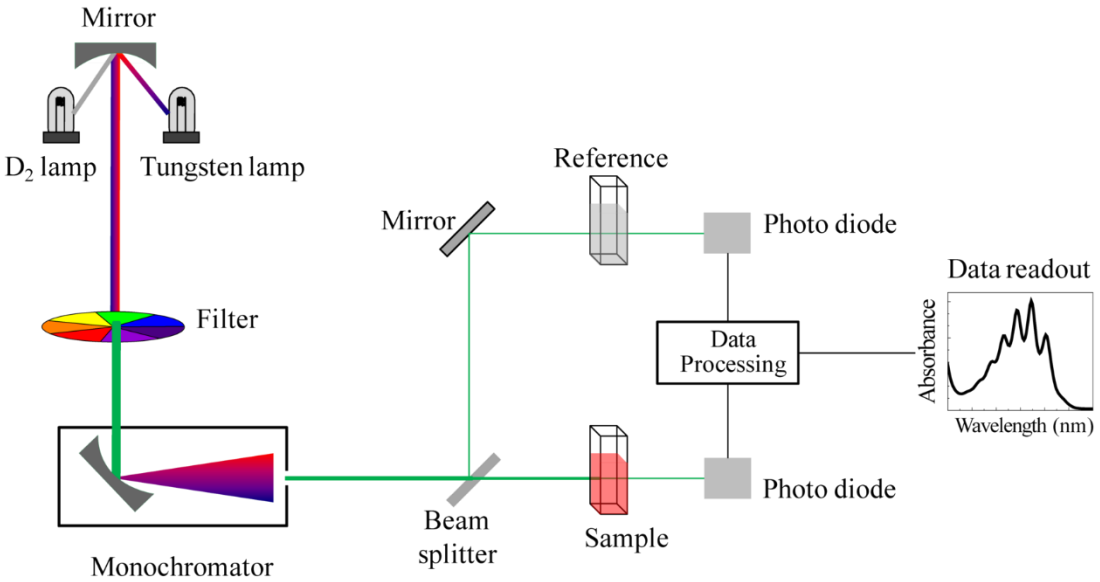

Figure 2.7: Schematic of UV-vis spectrometer.

concentration can be extracted from the UV-vis spectra if the coefficient for a given wavelength is available.

The standard set-up for a UV-vis spectrometer is shown in Fig. 2.7. The sample to be analyzed is first diluted to an optical density suitable for measurement, then an aliquot is pipetted into a quartz cuvette with a known path length. A reference sample containing the solvent is measured simultaneously, providing a baseline which is subtracted from the sample spectrum. In this manner the absorbance of the material is isolated from the solvent.

It is in fact more accurate to describe this attenuation of the beam as extinction, rather than absorption, but for solutions they are essentially identical as particles are so small that scattering contributions can essentially be ignored. In the case of dispersions of 2D nanosheets however, the interaction of incident radiation with the relatively large nanosheets (compared to the solvent molecules) results in significant scattering. This scattering is dependent on the size of nanosheets in the dispersion and may be wrongly attributed to the absorption of the material, giving an incorrect spectrum. The extinction ($\epsilon(\lambda)$) is therefore a combination of the absorption ($\alpha(\lambda)$) and the scattering ($\sigma(\lambda)$).

$$\varepsilon(\lambda) = \alpha(\lambda) + \sigma(\lambda)$$

In order to deconvolute the extinction into its absorption and scattering components it is necessary to use an attachment for a UV-vis spectrometer called an integrating sphere. As the name suggests the attachment is a spherical container, the inside walls of which

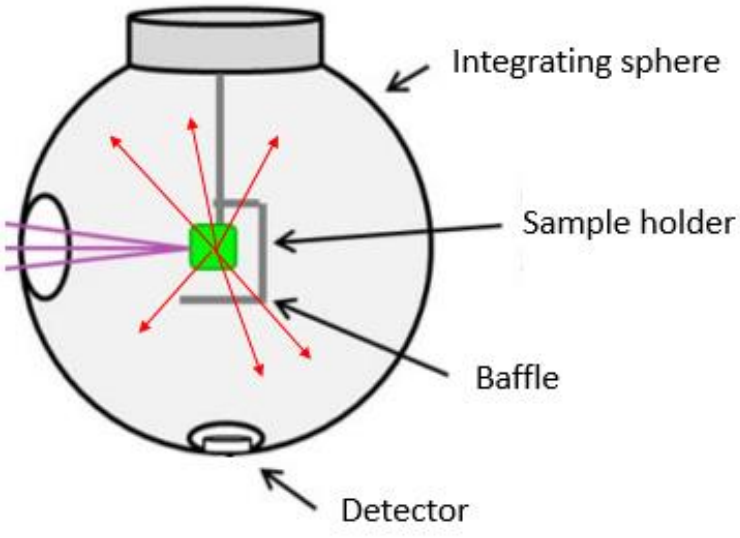

Figure 2.8: Cross section of an integrating sphere. Adapted from [117].

are covered in a diffuse white coating. Incident light passes through an opening in the front of the sphere and interacts directly with the sample which is suspended in a cuvette. Subsequent scattering of the light from the nanosheets cause numerous instances of light impinging on the white coating, where it is reflected. Multiple iterations of the light reflecting causes the intensity level to reach a steady state,[117, 118] and only light rays that have been diffused within the sphere arrive at the detector. Fig. 2.8 shows a schematic of an integrating sphere.

Determining the absorbance in this way allows the scattering contribution to be isolated as it can easily be subtracted from the extinction spectrum. In this way multiple spectral responses can be examined independently for a given sample.

Electron microscopy:

Electron microscopes use beams of high energy electrons emitted from a gun, which then impinge upon the sample. Transmission electron microscopy (TEM) and scanning electron microscopy (SEM) were both used in the work described in this thesis to image layered materials. Unlike TEM, SEM can image bulk specimens, which means it can be used to image material prior to exfoliation in its initial bulk form. In this case the electrons

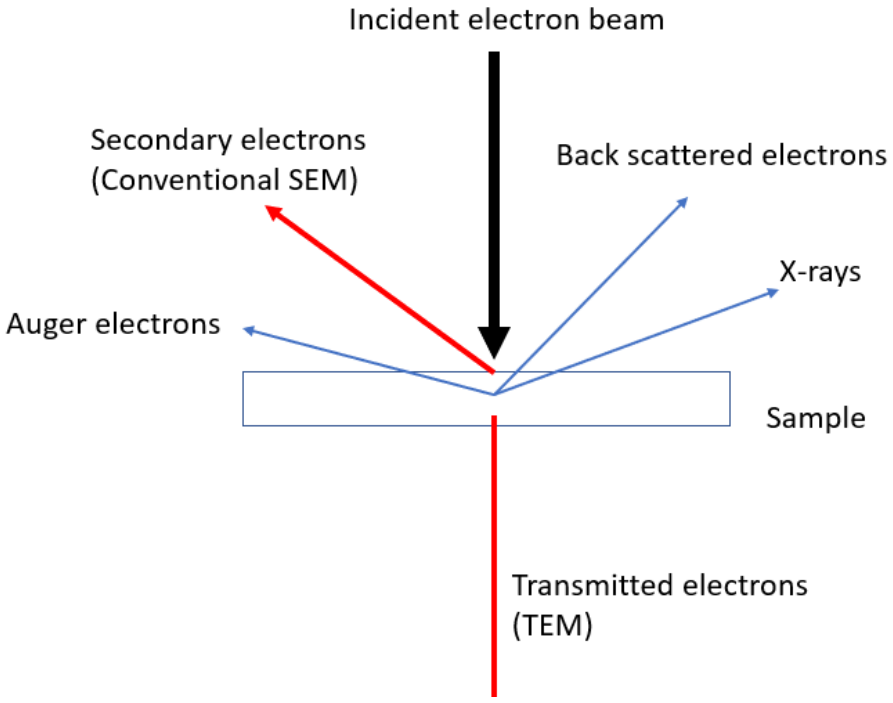

Figure 2.9: Interactions of electron beam with sample.

are scattered from the surface of the specimen. TEM on the other hand requires a thin sample to facilitate the transmission of the electron beam through it.

Transmission Electron Microscopy:

Conventional TEM involves the irradiation of a thin sample with a high energy electron beam. These electrons are produced by thermionic or field emission in an electron gun. The illumination of the sample by the beam is controlled using a condenser system composed of lenses and apertures. After impinging upon the sample, the transmitted beam passes through the objective system, which controls the imaging conditions. Finally, a projector lens system magnifies the resultant image or diffraction pattern onto a fluorescent screen.[119-121] The schematic for a standard TEM column is shown in Fig. 2.10.

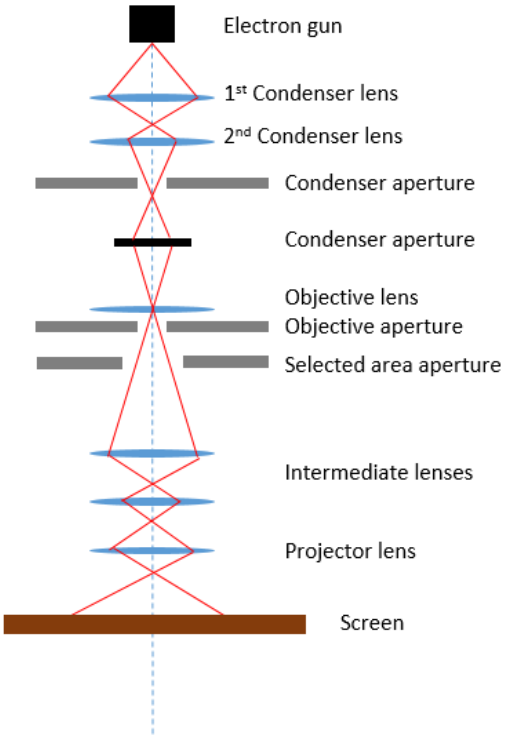

Figure 2.10: Schematic of a TEM.

A sample must be very thin to be suitable for imaging using TEM, as the electrons interact very strongly with atoms by scattering, both elastic and inelastic. For thicker samples to be examined an increased voltage is required.[120]

Conventional imaging in TEM can be either *bright field* or *dark field*.[119] A bright field image is formed when the aperture is positioned in such a manner to only permit the transmitted (not diffracted) electrons. Conversely, for dark field images some of the diffracted electrons are allowed to pass.

Performing TEM on liquid exfoliated samples allows the dispersed species to be imaged and is one of the first priorities among characterization methods when exfoliating a new material for the first time. It is often clearly apparent from the images whether the material is indeed a layered species, and whether the exfoliation process has been successful in delaminating the flakes. Additionally, analysis of TEM images using ImageJ software allows the flake size distribution of the nanosheets to be measured. The length of a given nanosheet in this case is defined as its longest dimension. Fig. 2.11 gives example TEM bright field images of liquid phase exfoliated nanosheets.

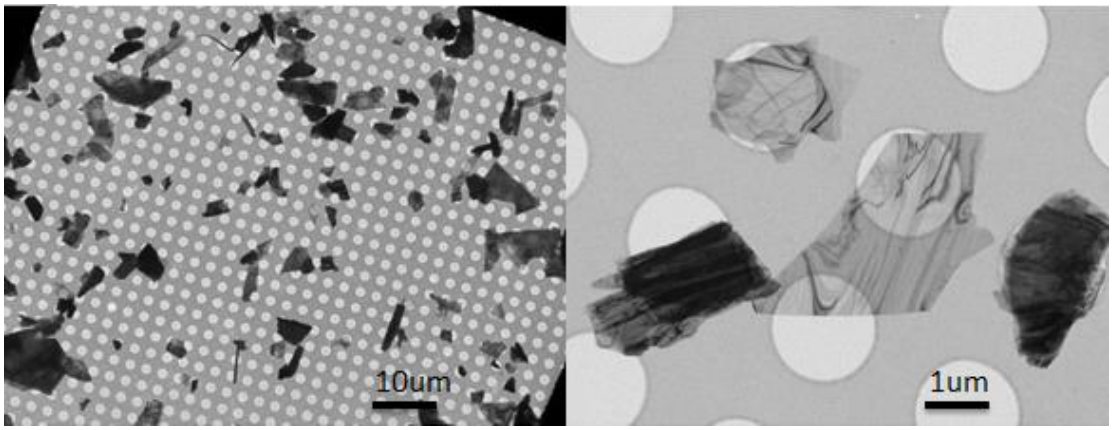

Figure 2.11: Example TEM images.

As discussed above, TEM imaging is dependent on using a thin specimen. In order to prepare a suitable sample, a few drops of the diluted dispersion are drop casted on holey carbon TEM grids. These grids are first placed on filter paper to wick away any excess solvent. Prior to imaging the grids are dried, typically overnight, to ensure all solvent has been removed.

As mentioned above, in addition to the qualitative information provided by the images, quantitative analysis of the nanosheets can be performed to give an indication of the distribution of flake sizes within the sample dispersion. This is done by taking a series of images at random points on the grid, taking care to include an unbiased array of the flakes

present. ImageJ software is then used to calculate the length of all the nanosheets imaged, where the length is designated as the longest dimension of the nanosheet. Maximising the number of counts (~200) increases the accuracy of the average length. The resulting flake size distributions are commonly represented by histograms.

The instrument used for this work was a JEOL 2100 series TEM.

Scanning Electron Microscopy:

In contrast to TEM imaging, SEM can be utilized to provide information about bulk powder as received. The fact that SEM operates using emitted electrons from close to the sample surface means that this technique is not as limited in the samples which can be analysed as for TEM. Images are produced by scanning the sample surface with the electron beam. Atoms excited by the beam may emit secondary electrons, and it is these electrons which are used for imaging most commonly in conventional SEM. These electrons are emitted from very close to the surface and so can produce high resolution images of the surface morphology. The electron gun emits via thermionic, Schottky or field emission and the electrons are accelerated towards the anode. The path of the beam is controlled by electromagnetic lenses, similarly to the TEM operation. A condenser lens converges the beam and scanning coils are then used to raster the beam across the sample surface. Interaction of the beam can produce various forms of radiative responses, as shown in Fig 2.9. Secondary electrons are primarily used for imaging as mentioned above but back scattered electrons are also used occasionally. These belong to the parent electron beam and have been reflected back after elastic interactions between the beam and the sample surface. This takes place deeper in the sample whereas secondary electrons are emitted from very close to the surface, and therefore provide more information.[122-124]

Fig 2.12 shows a schematic for a conventional SEM.

The SEM imaging included in this thesis was performed by Cian Gabbett.

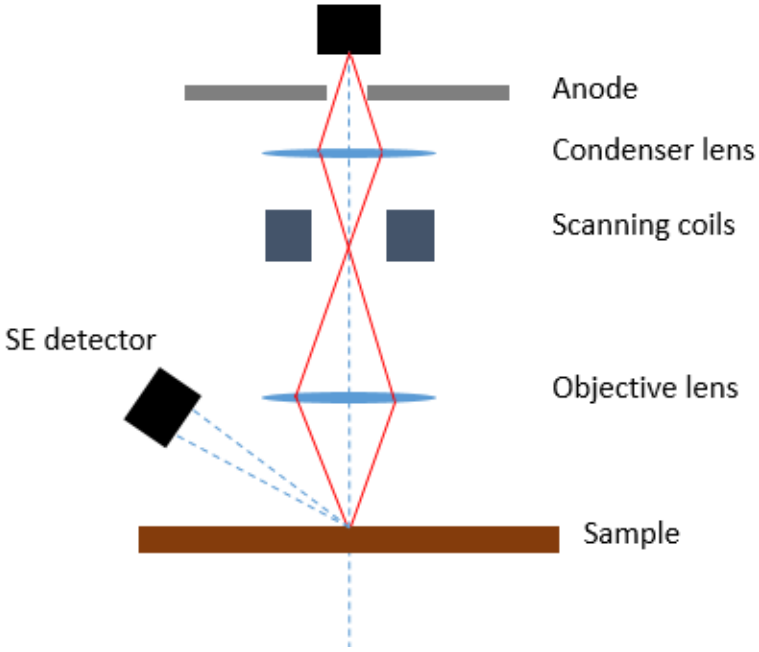

Figure 2.12: Schematic of SEM

Atomic Force Microscopy:

Atomic force microscopy (AFM) is a type of scanning probe microscopy which can be used to measure the dimensions of nanosheets present in dispersion. It provides a second method of examining the length of the flakes to compare with TEM analysis, but more importantly allows the thickness to be ascertained. Knowledge of the thickness of samples gives an indication of the number of individual layers and by extension, the degree of exfoliation.

The primary component of the AFM apparatus is a cantilever probe with a narrow tip, as shown in Fig. 2.13. The force between the probe and sample is measured by reflecting a laser beam off the cantilever. The reflected beam impinges on a photodetector which is position sensitive. In this manner any vertical or lateral deflections of the cantilever can be registered through variation of the beam position incident on the photodetector.

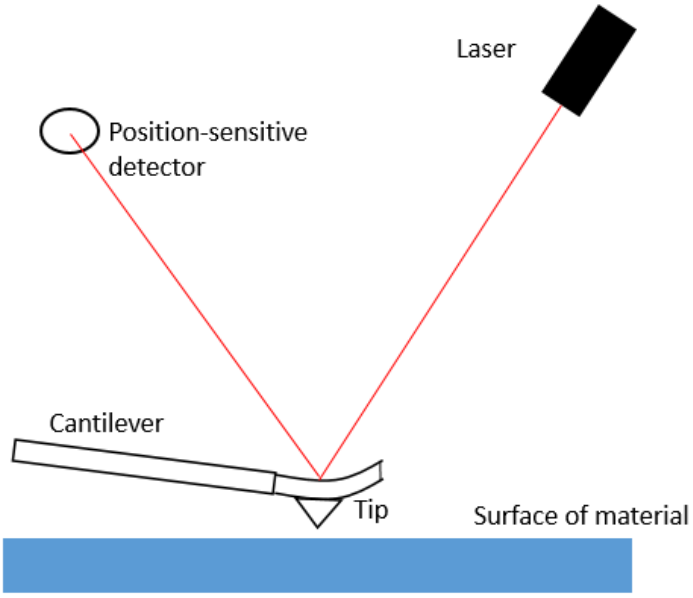

Figure 2.13: Schematic of AFM in operation.

Piezoelectric ceramics (a class of materials which expand or contract in response to electrical stimulus) are commonly used to position the tip with high resolution. The tip is made to raster across a small area of the sample surface at its resonant frequency. The response of the cantilever (and by extension, laser) as it scans provides topographical information about the sample via pixelated data of cantilever deflections. In order to optimize the resolution, the tip is ideally narrow enough that only the front atom interacts strongly with the surface.[125, 126]

Dispersions of nanosheets produced via LPE can be readily processed for AFM analysis by drop casting a diluted sample onto a hot substrate to evaporate the excess solvent. The dilution step is necessary in order to minimize the chances of material agglomerations on the substrate and ensure that individual exfoliated flakes are available for analysis. Step height measurements can extract the height difference between individual monolayers in the stack, and using this information the number of layers can be calculated.

Raman Spectroscopy:

Raman spectroscopy is a fast and non-destructive analysis technique based on the interaction of light with the chemical bonds within a material.[127] This spectroscopic method is commonly used to provide a structural fingerprint to identify molecules, and determines the vibrational modes present. In the work described in this thesis, Raman analysis is utilized primarily to compare bulk material with exfoliated nanosheets in dispersion, in addition to providing a means to track any observed degradation.

The technique is named after Indian scientist C.V. Raman who first observed the phenomenon in 1928.[128] However, it had been predicted by theoretical means in 1923 by A. Smekal.[129]

A source of monochromatic radiation such as a laser between the near-IR and near-UV range is typically used to provide incident light on the species in question. Scattering of the radiation occurs, with most of the scattered light being at the same wavelength as the

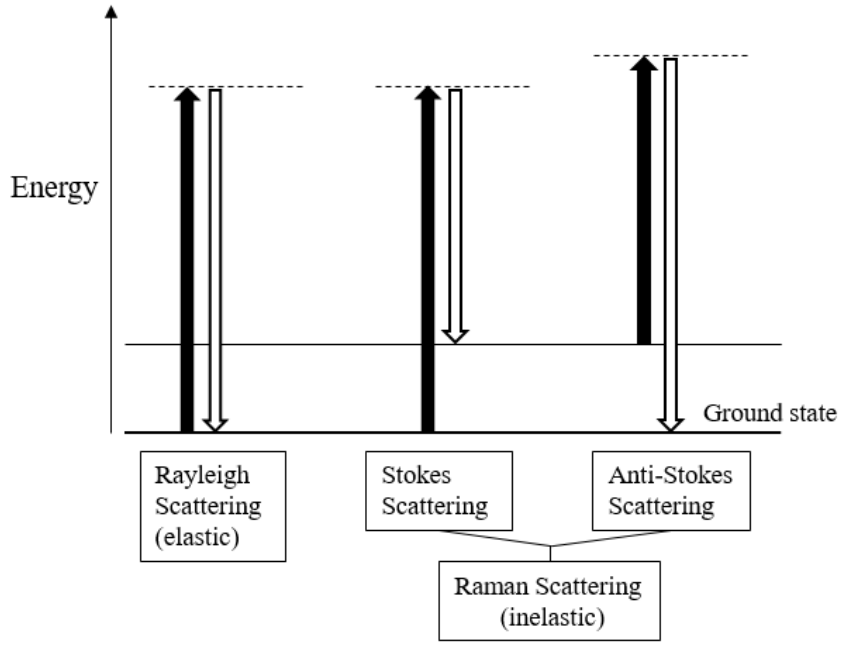

Figure 2.14: Jablonski diagram of Raman processes.

incident beam. This is known as Rayleigh scattering (elastic). However, a small portion of the light is scattered at different wavelengths. The photons lose or gain energy during the process, and this is known as Raman scattering (inelastic). If a molecule is in a higher energy state after scattering than before interacting with the incident beam it is called Stokes scattering. Conversely, Anti-Stokes scattering takes place when the molecule is in a lower energy state after scattering.

In general the peak positions and their relative intensities in spectra provide a unique chemical fingerprint which facilitates the identification of the material. Extensive libraries of Raman spectra are readily available for comparison. With regard to exfoliation of 2D materials, Raman is an important method for confirming that delamination has occurred without a change in the chemical composition of the material. Where oxidation has taken place, it is often immediately apparent from the addition of peaks or general shape change of the spectrum. Raman signals may also contain a contribution from photoluminescence (PL). Understanding that in the case of some semiconducting TMD species only the monolayers exhibit PL means that for these materials the PL/Raman ratios can give an indication of the monolayer volume fraction.[94]

Photoluminescence Spectroscopy:

Photoluminescence spectroscopy (PL) is a method for probing the electronic structure of materials. Incident light is absorbed and excites an electron to a higher energy state. The average lifetime in this state is very short, so relaxation of the electron back to its ground state takes place. There are multiple pathways this relaxation can take, some of which are non-radiative and others which occur with the emission of light. Fig 2.15 shows some of the energetic transitions which can be observed during photoluminescence.

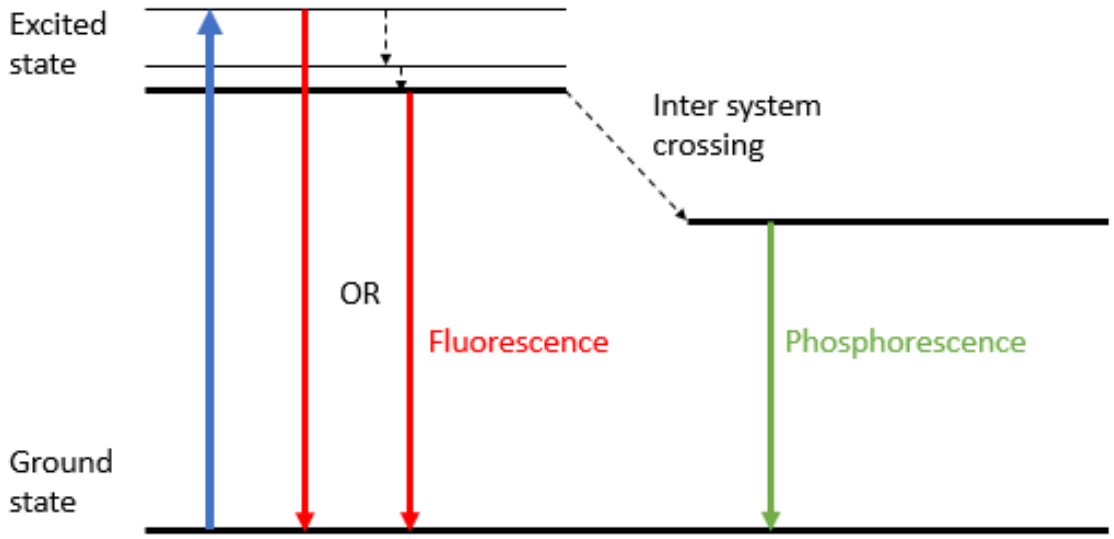

Figure 2.15: Representation of radiative processes in photoluminescence.

If light is emitted as the electron drops immediately from this excited state back to its initial state, this emission is called fluorescence. The timescale of this emission is very short, in the order of nanoseconds. Alternatively, if the promoted electron is at a higher energy level than the ground level of the excited state, non-radiative vibrational relaxation followed by fluorescence can occur. Another form of relaxation without emission is inter-system crossing, which involves the transition from the ground level of one excited sate into a different excited state or lower energy. If this process is followed by radiative relaxation to the ground state the emission is called phosphorescence and takes place much more slowly than fluorescence (milliseconds). [130, 131]

PL spectroscopy is a non-destructive technique which can be used for samples in both liquid and solid form, making it ideal for analysing liquid exfoliated samples.[131] It can be used to provide information about the optical bandgap and exciton binding energy of a material. In the case of semiconducting TMDs which undergo a transition from indirect to direct bandgap going from bulk to monolayer, the light emission for monolayers is much higher than for multilayers.

Fig 2.16 shows a schematic for a typical PL spectrometer.

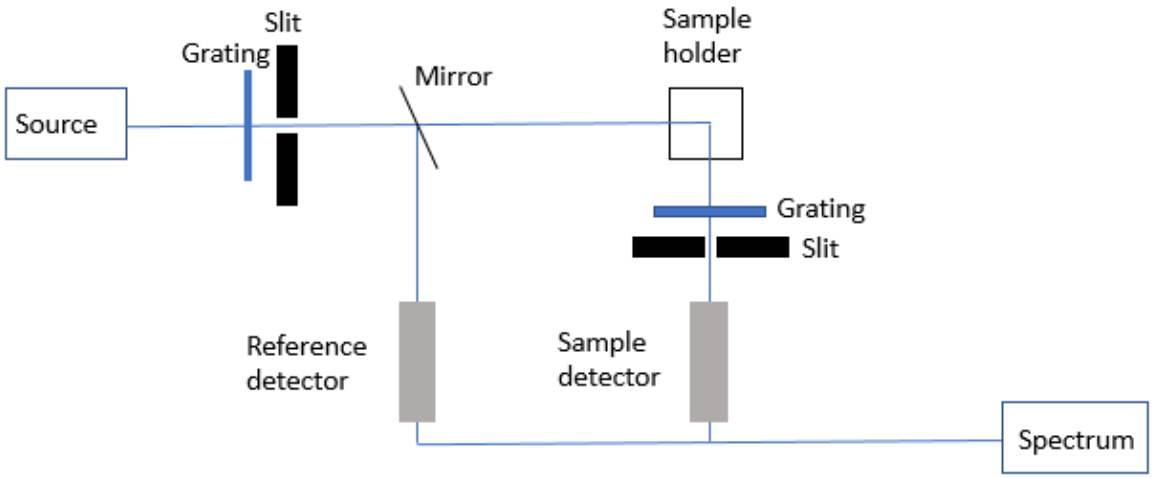

Figure 2.16: Photoluminescence spectrometer.

X-ray Photoelectron Spectroscopy (XPS):

XPS is a surface analysis technique which can provide information about the elemental composition, chemical/oxidation state of a material and detect the presence of functional groups. [132, 133] Irradiating a material with x-rays causes photoelectrons to be emitted (photoelectric effect). By measuring the kinetic energy of the emitted electrons the atomic core binding energy relative to the Fermi level can be determined. The various binding energies observed and relative intensity of peaks in a spectrum can be used to identify the elements present in the sample, in addition to their oxidation states.

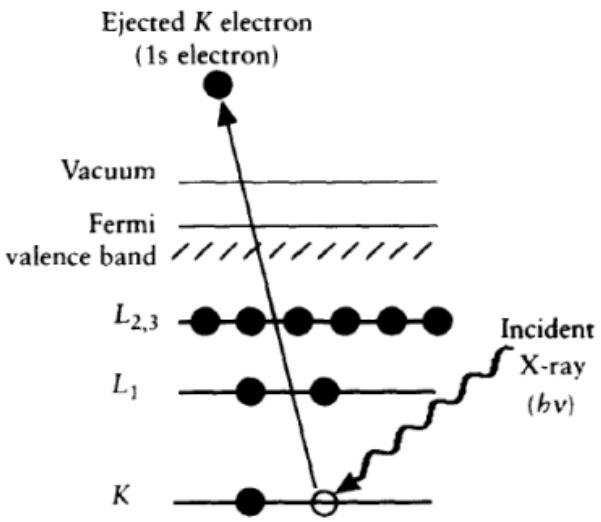

Figure 2.17: Ejection of a photoelectron following irradiation with X-rays. [132]

XPS measurements are carried out on solid samples, and typically does not probe deeper than ~ 5-10 nm into the material. The outer layers may be scraped or etched away to allow analysis of the bulk material or to simply remove surface contamination. Given that liquid exfoliated dispersions can be easily processed into films by vacuum filtration or drop casting, XPS is a compatible characterization technique for dispersions produced by LPE. In addition, the fact that the incident beams are composed of x-rays there is very little charging of the sample. As a result the electrical conductivity of the material to be examined is irrelevant with regard to suitability for this process.[134] For the work described herein XPS is used primarily as a means to ascertain the oxidation state of species detected in exfoliated nanosheets.

X-ray Diffraction:

Although discovered in 1895 by Rontgen, the wave nature of x-rays was not successfully demonstrated until 1913 by von Laue. X-ray diffraction (XRD) utilises x-rays to provide a

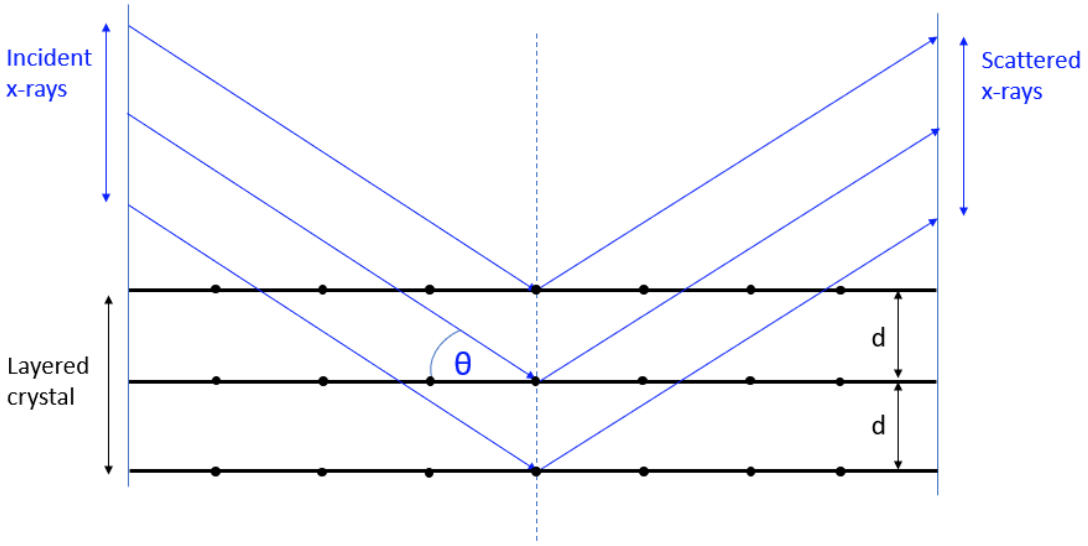

Figure 2.18: Interaction of x-rays with layered structure.

substantial amount of information about a material, such as the chemical composition, its crystallinity, the presence of any impurities and the crystal parameters. Each material examined gives a distinct fingerprint response which can be compared to a database to identify any species present. Regarding dispersions of nanosheets produced by LPE, XRD is a powerful technique for comparing the material before and after treatment or for identifying any species observed to appear with oxidation/degradation of the sample. A key advantage of XRD is the versatility it provides, to the extent that the technique is equally capable of analysing powder samples or films made from dispersed nanosheets by vacuum filtration. In both cases many particles with random orientations are present, ensuring that at least some of them are properly oriented.

When a beam of monochromatic x-rays impinges on a material, some of the rays are scattered. Fig. 2.18 shows incident x-rays on a crystal composed of multiple equidistant lattice planes, with the separation distance between subsequent planes designated as d. The scattered beams from atoms in each plane are in phase when the angles of incidence and diffraction are equal. In this situation constructive interference produces XRD peaks. Using trigonometry, it can be determined that the path difference between the beams hitting atoms in the first and second planes is 2dsinθ. The conditions necessary for this constructive interference are defined by Bragg's Law:

$$n\lambda = 2dsin\theta$$

where n is an integer, λ is the wavelength of the x-rays and θ is the angle of incidence. If this law is not satisfied, then interference will not be constructive in nature and the intensity of the diffracted beam will be much lower.

In operation, the sample is attached to a goniometer head which allows the orientation of the sample to be varied in relation to the incident beam. A source of monochromatic x-rays is aimed at the sample in the holder and the diffracted beams are collected by a detector which generates peaks at the angles corresponding to the diffraction. Comparison of the observed spectrum to those available in databases is used to identify the material composition.[135-137]

3

Liquid Phase Exfoliation of Molybdenum (IV) Oxide

3.1 MoO_2:

Due to the vast array of layered materials in existence[138] and because LPE has been so successful at exfoliating a wide range of different layered crystals, an obvious strategy is to use this method to delaminate as many new 2D materials as possible. One candidate is molybdenum dioxide (MoO_2). Layered MoO_2 is metallic with a rutile structure[139], is relatively cheap to buy and has low toxicity[23, 24]. This material has been shown to be promising in supercapacitor[140, 141] and catalytic applications,[37, 142] in addition to being used as an anode material in Li ion storage batteries.[110, 143-145]

Figure 3.1: MoO_2 powder, and vial of nanosheets dispersed in IPA.

In this Chapter it will be shown that MoO_2 nanosheets can be produced by liquid phase exfoliation in a range of solvents. A combination of Raman and extinction spectroscopy show the resultant nanosheets to oxidize over a number of days to form higher oxides such as MoO_3. However, if processed rapidly, these nanosheets can be used to prepare reasonably stable networks. The potential of this material is demonstrated through the use of such networks to fabricate high performance Li-ion battery anodes.

Although MoO_2 has been produced through synthesis,[61, 146-148] it has yet to be exfoliated by any liquid exfoliation procedure. Achieving liquid exfoliation of MoO_2 would yield a number of advantages including a nanoscale morphology as well as significantly improved processability. In addition, for battery electrode applications, exfoliation of layered materials to nanosheets has been shown to significantly improve both capacity and stability in materials such as gallium sulfide[69] and vanadium oxide.[149] Thus, liquid phase exfoliation of MoO_2 should yield advantages in battery applications and possibly other application areas. However, it goes without saying that little is known about the properties, processability or stability of liquid exfoliated MoO_2.

Initial examination of the material received from Sigma Aldrich showed that the powder was a purple colour. Imaging of the bulk powder using SEM (Fig. 3.2) indicated distinct, irregularly shaped flakes with its layered nature also being discernible from inspection.

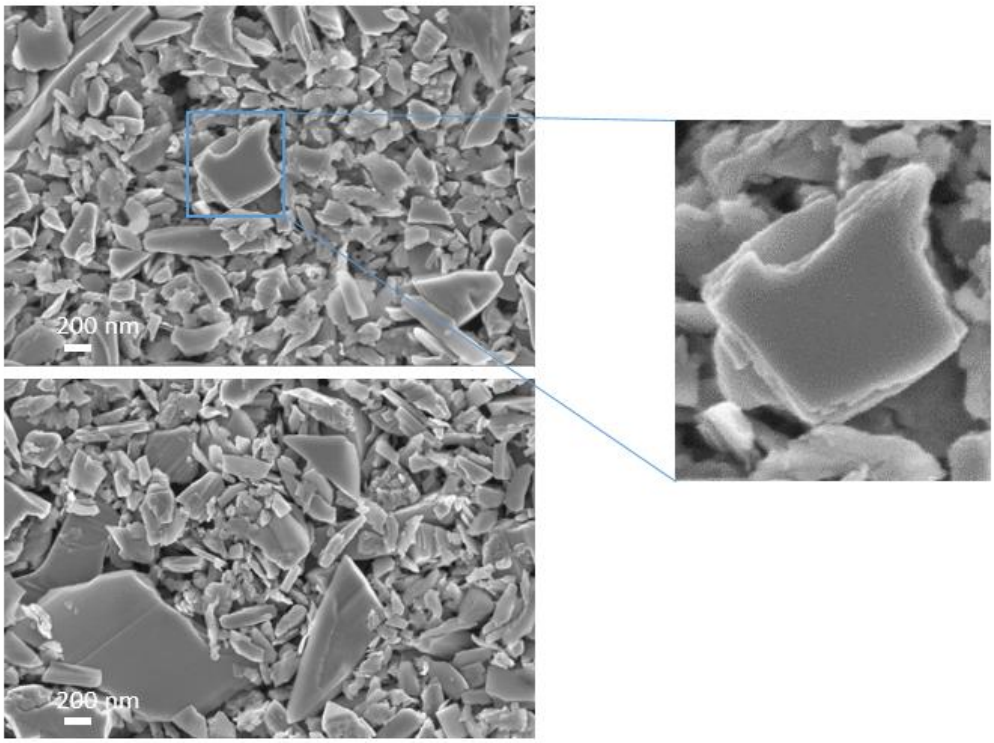

Figure 3.2: SEM images of MoO_2 powder.

A preliminary exfoliation experiment was performed to see if a dispersion of MoO_2 nanosheets could be made. The powder was sonicated in isopropanol (80 mL) at a starting concentration of 10 mg/mL MoO_2. After sonication the dispersion was centrifuged for

one hour at 1000 rpm in order to remove any unexfoliated material. The supernatant was decanted and noted to have a very dark colour, seeming almost black upon initial inspection but displaying a deep purple colour after dilution with more isopropanol. The sample was prepared for TEM by drop casting this diluted dispersion onto a TEM grid, was dried overnight and imaged the following morning. Shown in Fig. 3.3 are representative TEM images from this dispersion, which exhibits multiple MoO_2 nanosheets with little aggregation. There is a significant variance in the size of the flakes, indicating that the nanosheets in suspension are quite polydisperse.

In order to preserve the flow of the Chapter the majority of the specific details of the methods used are included in the experimental approach section (3.8) towards the end of the Chapter.

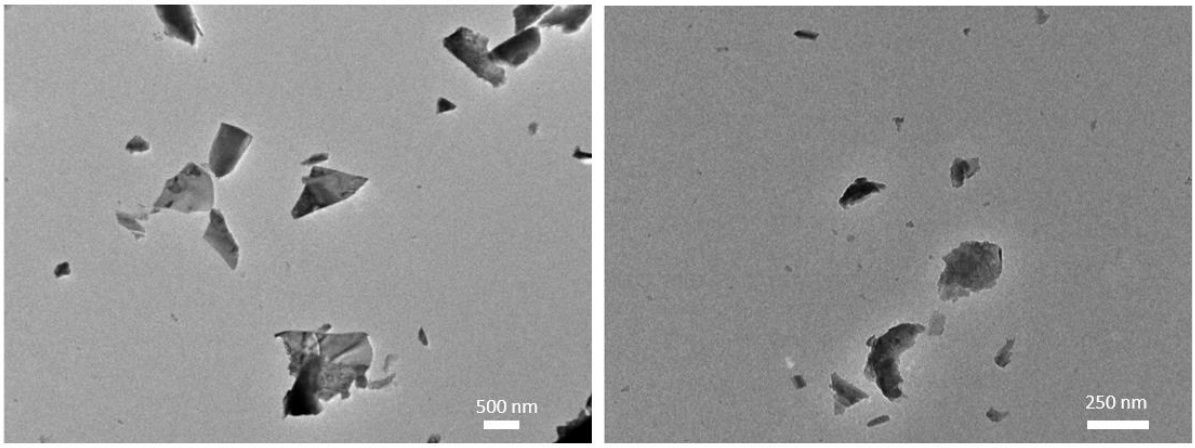

Figure 3.3: TEM images of MoO_2 nanosheets exfoliated in isopropanol (IPA).

3.2 Optimisation of Exfoliation Conditions:

Having shown that MoO_2 could be delaminated successfully using LPE, the next step was to determine the conditions under which optimal exfoliation could occur. The procedure for LPE remains consistent from one material to another for the most part, however a number of variables can be altered to best suit the material in question. Examples of such variables include the solvent used, the sonication time and the initial concentration of material used.

Prior to beginning an exfoliation study on a new material suitable conditions for delamination need to be chosen. There are multiple variables in the exfoliation procedure which must be taken into consideration. These include the sonication method (bath vs sonic probe), sonication parameters (time, initial concentration, pulse ratio), solvent parameters and centrifugation regime (speed and time).

The primary means of gauging the effects of these parameters is measurement of the concentration of the corresponding dispersion after sonication and/or centrifugation, as this gives an indication of the amount of material successfully stabilized in the solvent. A simple yet effective method for ascertaining the concentration of a liquid phase exfoliated sample is vacuum filtration. An aliquot of known volume of the dispersion is passed through a filter membrane of known mass, which permits passage of the solvent and collects the dispersed material. After the membrane has been allowed to dry and is weighed again, the new mass reading corresponds to the material present in the aliquot filtered. This method has been discussed previously in more detail in the Materials & Methods Section. Although vacuum filtration provides a relatively accurate measurement of concentration, it is time consuming and is therefore not feasible in the case where the concentration of multiple samples needs to be acquired simultaneously, particularly for dispersions of materials which are prone to degradation. For these reasons, UV-vis spectroscopy was used to provide an equation relating the dispersed concentration to the extinction.

Calculation of Concentration using Extinction Spectroscopy:

A dispersion of MoO_2 in IPA (80 mL, 20 mg/mL starting concentration MoO_2) was prepared by sonication and was size selected using centrifugation (See ‘liquid cascade centrifugation’ in Materials & Methods section). IPA was used as it has been shown to

be an effective solvent for exfoliation and is easier to work with than many other solvents. The average length for each size fraction was determined by TEM analysis using ImageJ software and the concentration for each was measured by vacuum filtration. An aliquot of each sample was taken and analyzed via UV-vis spectroscopy.

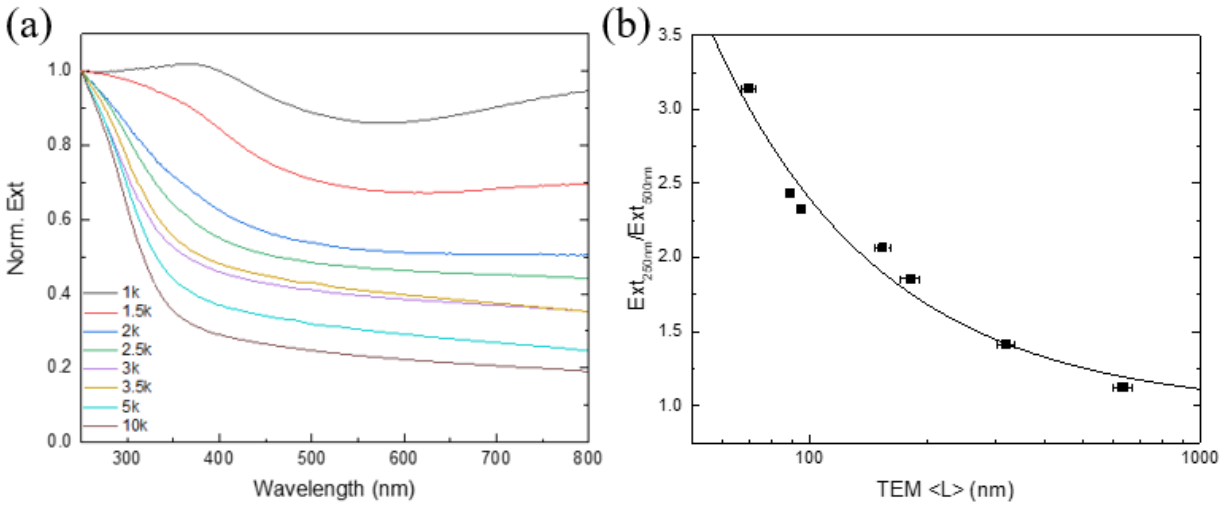

Figure 3.4: (a) Normalized extinction spectra for size selected MoO_2. (b) Ext at 250 nm divided by Ext at 500 nm against average nanosheet length for size selected samples. R-square = 0.96. See appendix for fitting data.

It is now well-known that the optical properties of 2D materials are greatly affected by the dimensions of the nanosheets.[99, 150, 151] The extinction (Ext), absorption (Abs) and scattering (Sca) spectra were measured for each fraction using a UV-vis spectrometer with an integrating sphere attachment.[99] The extinction spectra were normalised to 250 nm as shown in Fig. 3.4(a). It can be seen clearly that there is large variation in spectral shape with nanosheet length. As mentioned previously the extinction spectra are made up of contributions from photons being both absorbed and scattered by the nanosheets.[68, 152] The resultant spectral shape change can be described quantitatively via the ratio of extinction values between the plateaus at long wavelengths versus the peak at short wavelengths. This disparity can be quantified as shown in Fig. 3.4(b) where the ratio between the extinction at 250 nm and 500 nm is plotted against <L> as calculated from the TEM. Fitting this curve to an empirical equation yields an expression which related <L> to the ratio mentioned above:

$$< L >= \frac{143}{\frac{Ext_{250nm}}{Ext_{500nm}} - 0.97}$$

where <L> is in nm. This relationship can prove useful as it can be used to determine the average nanosheet dimensions of a dispersion and avoids the need to use statistical microscopy which can be time-consuming.

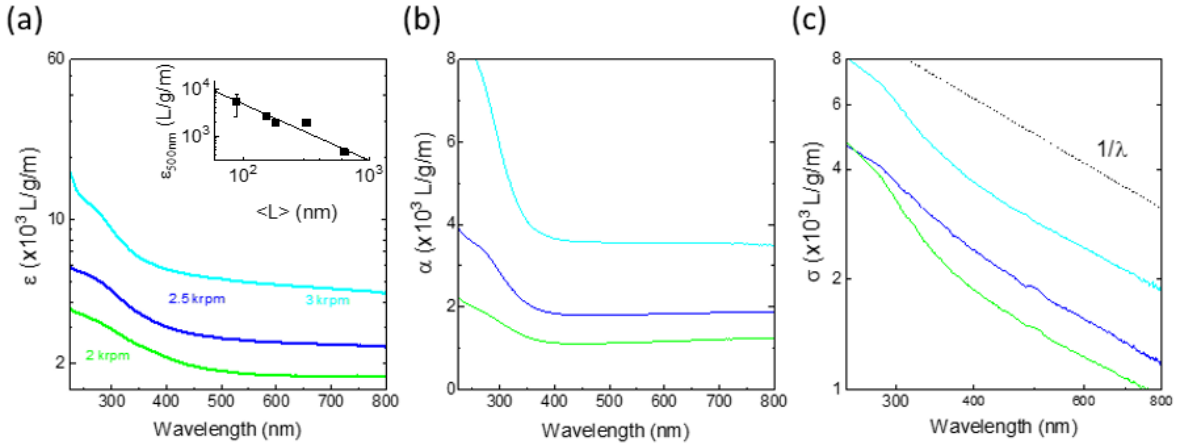

Figure 3.5: Representative samples of extinction (a), absorption (b) and scattering (c) spectra for three size fractions.

Having also measured the concentration of each size fraction the spectra could be converted to coefficient spectra using the following relations: Extinction, $Ext = \varepsilon Cl$, Absorption, $Abs = \alpha Cl$ and Scattering, $Sca = \sigma Cl$. Shown in Fig. 3.5 are ε, α and σ spectra respectively for three fractions, 1-2krpm, 2.5-3krpm and 3-3.5krpm. Despite the scattering contributions which increase for larger nanosheets, the extinction coefficient is greater for smaller nanosheets than larger ones, which implies that a large contribution to the extinction spectra is due to absorption. This can be seen in Fig. 3.5 where the absorption spectra (b) look similar in shape to the extinction spectra (a). Despite the material absorbing light across all wavelengths Fig. 3.5(c) still shows scattering coefficient spectra to display the typical power-law behaviour shown for other materials with a non-resonant regime such as GaS[68, 152] and $Ni(OH)_2$[78]. The inset in Fig. 3.5(a) shows extinction at 500 nm plotted against flake length <L>, showing a well-defined trend which can be fitted with the empirical expression:

$$\varepsilon_{500nm} = \frac{1.2\times10^6}{<L>}$$

This equation can be used to estimate the extinction coefficient once the mean nanosheet length is known (e.g from equation), returning a value in $Lg^{-1}m^{-1}$ when <L> is entered in

nm. Combining these equations with the fact that $Ext_{500nm} = \varepsilon_{500nm} Cl$ yields an expression for the MoO_2 concentration:

$$C = 3.22 \times 10^{-4} \frac{Ext_{500nm}}{l} \left[\frac{Ext_{250nm}}{Ext_{500nm}} - 0.97 \right]^{-1.2}$$

In this manner the concentration of any nanosheet dispersion could be determined once the extinction spectrum was measured.

Centrifugation Study:

An investigation was carried out to examine the effects of centrifugation (both speed and time) on molybdenum dioxide dispersions. The aim of this centrifugation study was to identify the parameters which would optimize the quality of nanosheet dispersions produced. Centrifugation is an essential part of the LPE process, both for size selecting the nanosheets and to remove any unexfoliated material after sonication. Despite this, it is a time-consuming technique, so it is important to identify the optimal centrifugation time for a given dispersion. The centrifugation speed is another parameter that can influence the material content of the exfoliated sample. Generally, at low speed the larger, thicker flakes will sediment out and as the centrifugation speed is increased the smaller nanosheets can be extracted.

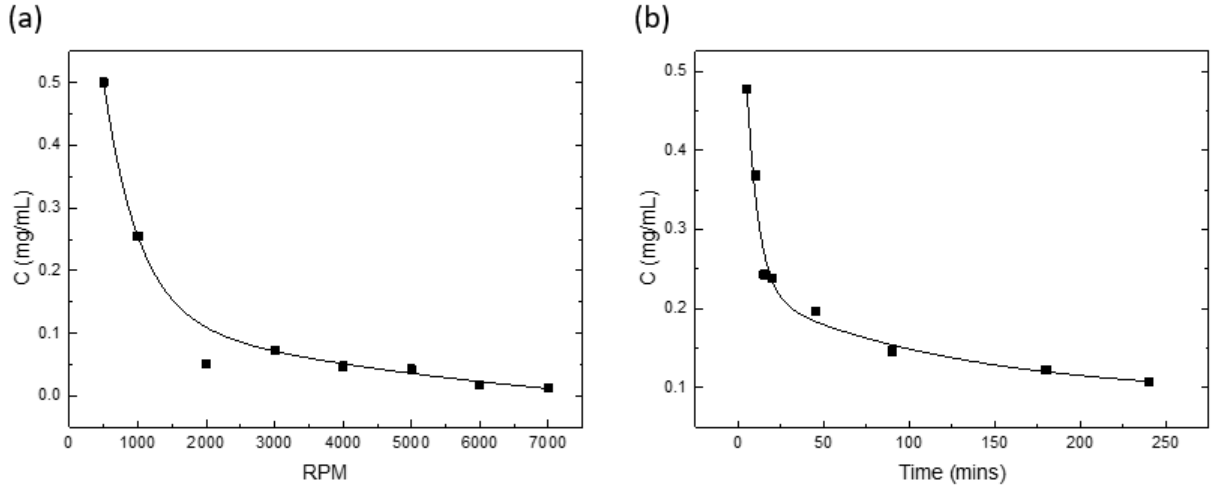

Figure 3.6: Dispersed concentration vs (a) rpm and (b) time.

A dispersion of MoO_2 in N-Cyclohexyl-2-Pyrrolidone (CHP) (80 mL) was prepared by sonicating the material for 3 hours at an initial concentration of 20 mg/mL. CHP was chosen due to its high viscosity. This would suggest centrifugation times in CHP would

be longer for the nanosheets to reach a steady state concentration. If these centrifugation parameters could be identified for CHP it can be assumed they will be suitable for less viscous solvents too. After sonication, aliquots were added to glass vials and each centrifuged at a different rate (500, 1000, 2000, 3000, 4000, 5000, 6000 and 7000 rpm) for one hour. Another dispersion was produced under identical sonication conditions, but this time aliquots were centrifuged at 3k rpm for a range of centrifugation times (5, 10, 15, 20, 45, 90, 180, 240 mins). The supernatant of all centrifuged samples were analyzed using UV-vis spectroscopy, and the dispersed concentration for each was determined from the extinction spectra. Fig. 3.6 shows the concentration plotted vs RPM (a), and centrifugation time (b). In both cases the concentration was observed to follow double exponential behaviour. As discussed in the Materials and Methods Section this behaviour is similar to what has been seen previously for other layered materials. The optimal centrifugation conditions for a stable dispersion were identified as 2500 rpm and 2.5 hours for the centrifugation rate and time respectively. These parameters were used for the all samples in the solvent study. For subsequent dispersions after the solvent study a broader trapping between 500 and 5000 rpm was used to ensure a wider range of nanosheets sizes were obtained.

Solvent Screening:

In order to ascertain the best solvent for exfoliating the MoO_2 powder, a series of exfoliations were carried out. The sonication conditions were identical for each dispersion, with the exception of swapping out the solvent used. MoO_2 was sonicated for 30 minutes in a glass vial containing 20 mL solvent at a concentration of 5 mg/mL using a tapered tip at 25 % amplitude. Solvents with Hildebrand solubility parameters covering a wide range were chosen. The resulting dispersions were centrifuged using the parameters determined in the centrifugation study i.e. 2500 rpm (665 g) for 2.5 hours, and the dispersed concentration was determined from UV vis spectroscopy and showed a significant variation between 0.01 and 2 mg/L. Plotting the dispersed concentration, C, against the Hildebrand solubility parameter, δ, in Fig. 3.7 shows that the dispersed concentration of MoO_2 is maximized for solvents with solubility parameters in the range 18-25 $MPa^{1/2}$. The apex of the Gaussian envelope function fitted with this data suggests that the solubility parameter of the nanosheets to be ~22 $MPa^{1/2}$, which is consistent with

what has been seen previously for other 2D materials. The fact that both acetone and 2-Isopropoxyethanol (IPP) have solubility parameters close to this value and still result in dispersions with low concentrations is indicative of the fact that this is an imperfect system, and merely functions as a rough guide. It is for this reason that it is difficult to simply prescribe an optimal solvent from its Hildebrand solubility parameter alone.

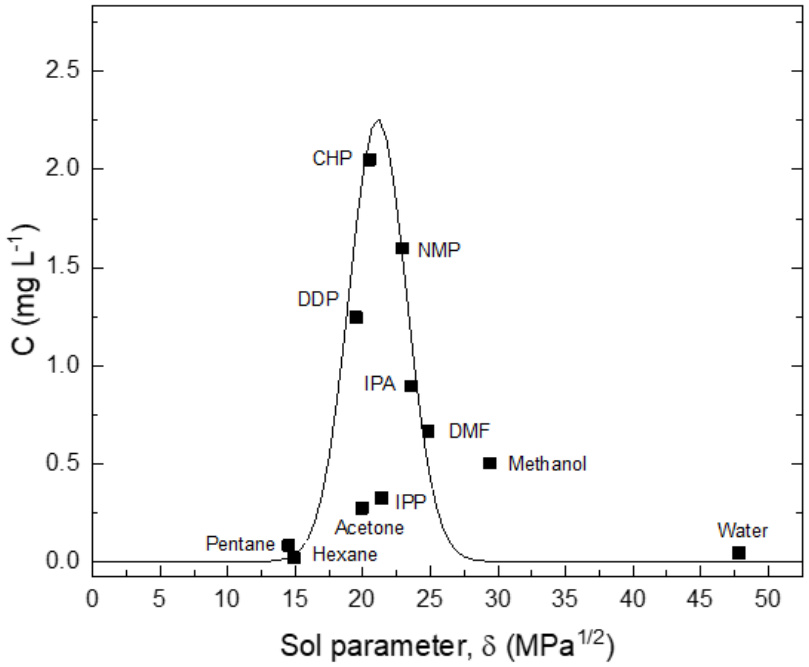

Figure 3.7: Dispersed concentration of MoO_2 nanosheets vs Hildebrand solubility parameter for a range of solvents. R-square = 0.94. (IPP and Acetone omitted from fit as outliers). See appendix for fitting data.

It is important to note that the concentration obtained during exfoliation is not the only factor that needs to be considered during solvent selection. Of the solvents tested cyclohexyl-pyrrolidone (CHP) and N-methyl-pyrrolidone (NMP) resulted in the highest dispersed concentrations. However, both of these solvents are quite hazardous to work with and have very high boiling points. Isopropanol (IPA) on the other hand is a low boiling point solvent compatible with most characterization methods and application testing techniques and manages to yield a reasonably high nanosheets concentration (~1 mg L^{-1}). For these reasons IPA was chosen for all subsequent dispersions. List of solvents used: Deionised Water (δ = 47.5 $MPa^{1/2}$), Isopropanol (δ = 23.6 $MPa^{1/2}$), Acetone (δ = 19.9 $MPa^{1/2}$), N-Cyclohexyl-2-pyrrolidone (CHP) (δ = 20.5 $MPa^{1/2}$), N-Methyl-2-pyrrolidone (NMP) (δ = 23 $MPa^{1/2}$), n-Pentane (δ = 14.4 $MPa^{1/2}$), Dimethylformamide (δ = 24.9 $MPa^{1/2}$), Methanol (δ = 29.6 $MPa^{1/2}$), n-Hexane (δ = 14.9 $MPa^{1/2}$), 2-Isopropoxyethanol (IPP) (δ = 21.4 $MPa^{1/2}$), 1-Dodecyl-2-pyrrolidinone (δ = 18.8 $MPa^{1/2}$).

Sonication Conditions:

Having identified isopropanol as a suitable solvent for exfoliating MoO_2, a sonication study was carried out to examine the effects of the initial concentration of material and the sonication time on the concentration of nanosheets in the dispersion.

A series of MoO_2 dispersions were prepared using a tapered sonic tip in 20 mL IPA, with the starting concentration of material being different for each (C_i = 0.5, 1, 2, 4, 8, 10, 20, 30 and 50 mg/mL). Every dispersion was sonicated for 1 hour and then centrifuged between 500 and 5000 rpm, each for 1 hour. The sediment from the 5000 rpm step was redispersed in an equal volume of fresh IPA and the concentration of each sample was measured using extinction spectroscopy. Plotting the dispersed concentration C against initial concentration C_i shows linear scaling. (Fig 3.8(a)) Although it is desirable to maximize the concentration of nanosheet dispersions, one must consider the cost efficiency of increasing the initial concentration. A starting concentration of 20 mg/mL was chosen for optimal exfoliation of MoO_2 dispersions.

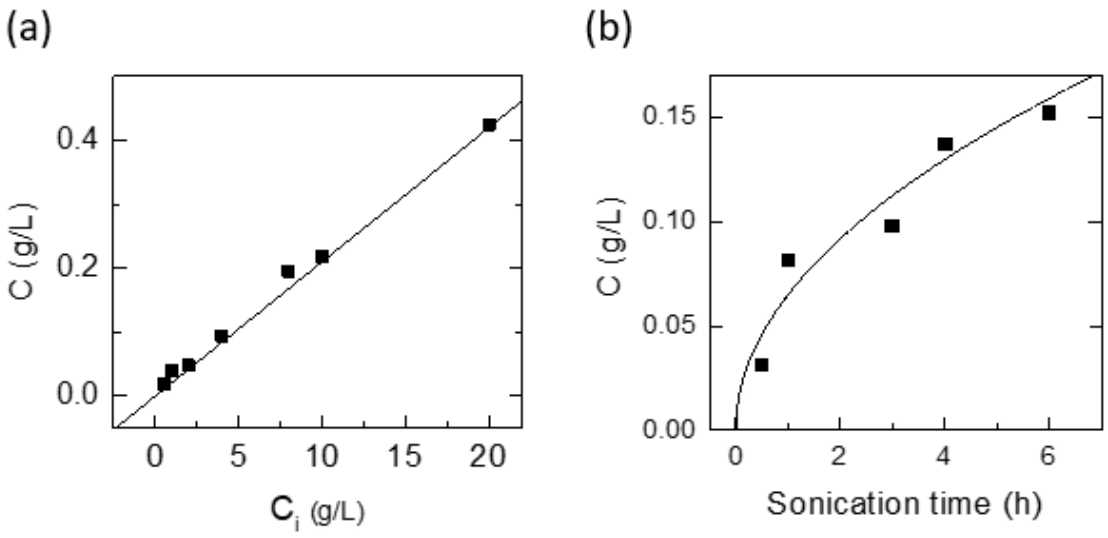

Figure 3.8: Dispersed concentration vs (a) initial concentration and (b) sonication time. R-square = 0.99 and 0.92, respectively. See appendix for more details on fitting.

To investigate the effect of sonication time a MoO_2 dispersion was prepared with 80 mL IPA and a starting concentration of 20 mg/mL. Aliquots were removed from the dispersion at fixed intervals during sonication (0.5, 1, 3, 4, 6, 8 and 24 hours). As with the initial concentration study each sample was centrifuged between 500 and 5000 rpm and the dispersed concentration was extracted from extinction spectra. Plotting this

against the sonication time showed that the resultant nanosheet concentrations displayed square-root scaling. (Fig. 3.8(b)) Such behaviour is as expected and has been observed in many studies with liquid exfoliation. In particular, the fact that $C \propto \sqrt{t_{sonic}}$ has been attributed to the effect of the diffusion of solvent molecules between the layers.[153] Extending the sonication time significantly would result in more concentrated dispersions, but with diminishing returns. Additionally, sonication for a protracted period increases the chances of degradation for materials unstable in ambient conditions. 6 hours was determined to be the optimal sonication time for production of MoO_2 nanosheet dispersions.

3.3 Standard Sample Preparation:

The next step was to exfoliate MoO_2 using the exfoliation parameters deemed to be the most effective from the experiments described in the previous section. MoO_2 powder was sonicated in an aluminium cup with 80 mL isopropanol (IPA) using a horn-probe sonic tip at 60 % amplitude at a MoO_2 concentration of 20 mg/mL. The dispersion was sonicated for 6 hours with a 6s/2s on/off pulse ratio and constant cooling used to prevent the solvent from boiling off. This cooling is merely to counteract the heating from the sonic tip. Once sonicated the dispersion was centrifuged using a Hettich Mikro 220R centrifuge equipped with a fixed angle rotor (where RCF = $106.4(\text{kRPM})^2$). The dispersion was centrifuged for one hour at 500 rpm (26.6 g) to extract unexfoliated material and then at 5000 rpm (2660 g) to remove extremely small nanosheets. The sediment from the 5000 rpm step was then redispersed using bath sonication. A dispersion produced in such a manner contains nanosheets with a broad distribution of sizes and thicknesses and is referred to as the 'standard' sample in this work.

An aliquot of the standard sample was drop casted on holey carbon TEM grids and imaged using a JEOL 2100 series TEM. These images serve both to confirm that the material in the dispersion is composed of delaminated nanosheets, and to highlight the polydispersity of the standard sample. It can be seen from these images (Fig. 3.9) that MoO_2 nanosheets produced by LPE tend to be a few hundred nanometers in size and display a range of thicknesses.

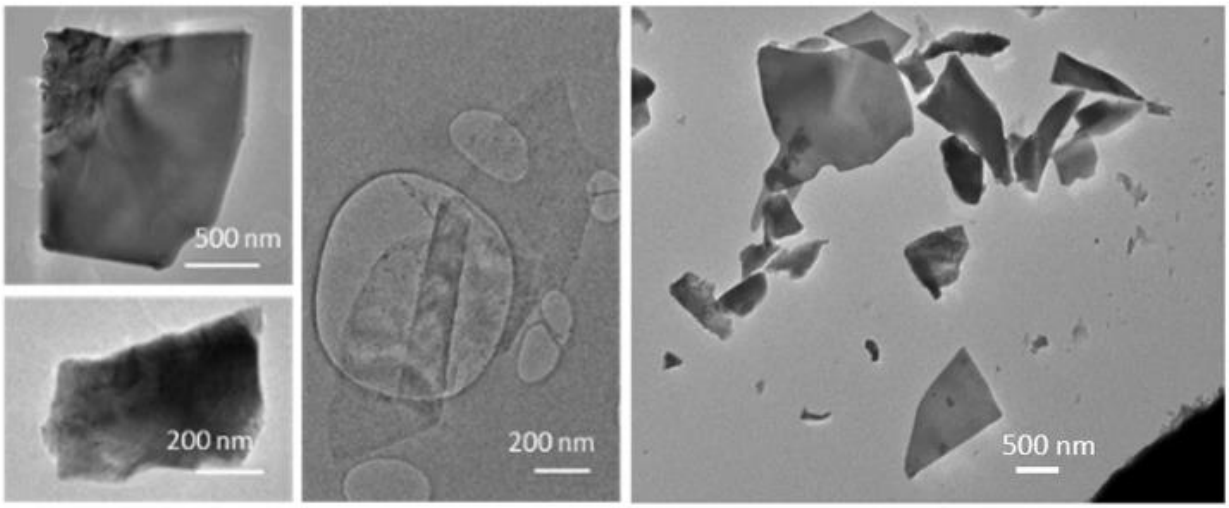

Figure 3.9: Representative bright-field TEM images of a standard sample dispersion.

The lengths (defined as the longest dimension) of individual nanosheets were measured from TEM images using ImageJ software. A histogram representing the flake size distribution was compiled and showed that the nanosheet lengths ranged between ~25 and 800 nm, with an average flake length of 360 ± 19 nm. AFM analysis of the same dispersion was carried out and determined the average length to be 340 ± 80 nm, consistent with the value from TEM. The AFM data can also be used to measure nanosheet thicknesses (expressed as layer number, N) with the resultant histogram shown in Fig. 3.10(c) This graph shows the nanosheets produced in the standard sample to be on average relatively thick (<N>=58), and to display a very broad range of thicknesses, up to N>100 monolayers. However, as will be shown later, size selection can be used to extract fractions with much lower mean thicknesses.

All AFM imaging and analysis was carried out by Aideen Griffin and Beata Szydlowska.

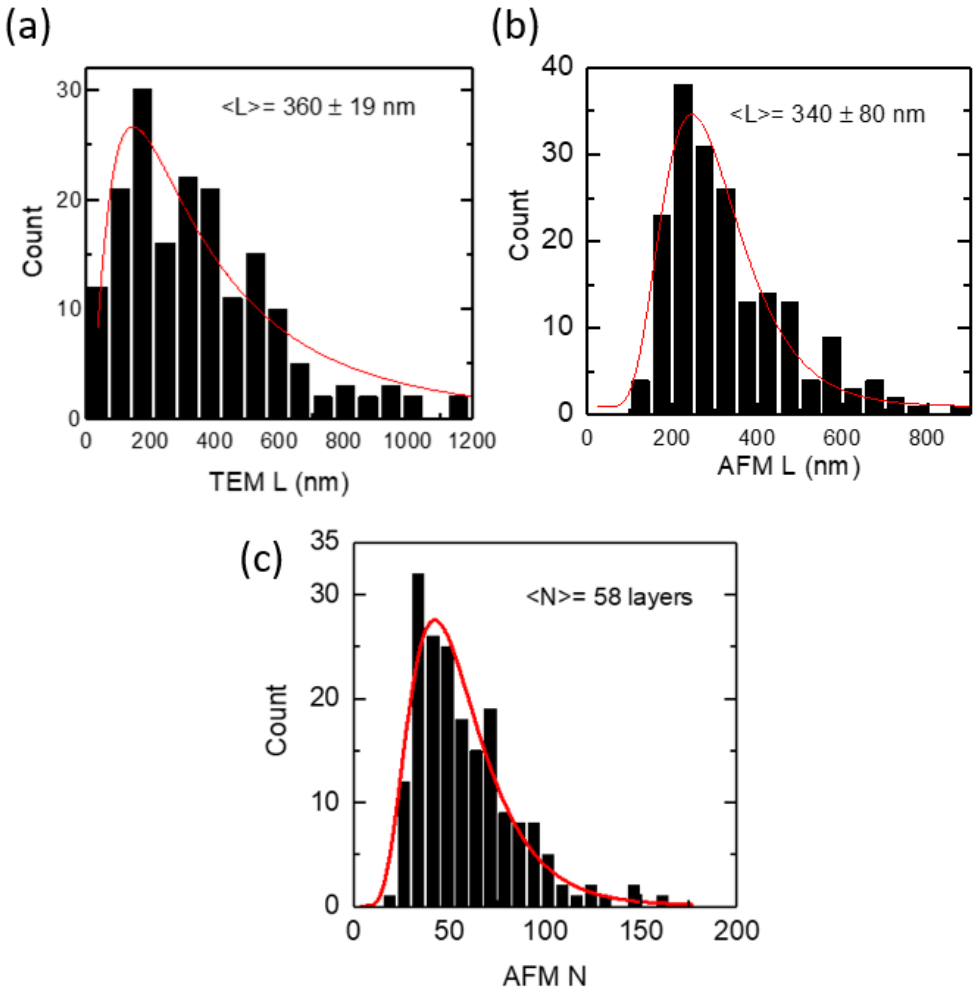

Figure 3.10: Flake size distributions from (a) TEM and (b) AFM. (c) Thickness of material in terms of layers, from AFM analysis.

The optical extinction spectrum of a standard sample dispersion of MoO_2 nanosheets in IPA is plotted in Fig 3.11(a)(black). This curve displays a peak at low wavelength combined with a plateau at high wavelength with the latter feature expected for a metallic material. However, it is noted that in nanoparticle dispersions, the extinction spectrum is often not a good representation of optical absorption because of the presence of strong scattering effects.[68, 152, 154] In general, the extinction (Ext) is the sum of absorption (Abs) and scattering (Sca) contributions, $Ext(\varepsilon) = Abs(\alpha) + Sca(\sigma)$, which can be separated using an integrating sphere.[68, 152, 154] The resulting absorbance and scattering spectra are shown in Fig 3.11(a)(blue and red respectively). Importantly, the high wavelength plateau persists in the absorption spectrum, confirming the nanosheets to be metallic in character.

To confirm the identity of the exfoliated material, Raman spectroscopy was performed on both the starting powder as received and a vacuum-filtered film of exfoliated nanosheets from a standard sample dispersion (Fig. 3.11(b)). Both spectra were similar and showed a significant number of peaks (at 203, 228, 350, 362, 459, 495, 568, 587 and 742 cm^{-1}), all of which have been assigned to MoO_2.[155] No other compounds have been observed in freshly prepared samples such as these.

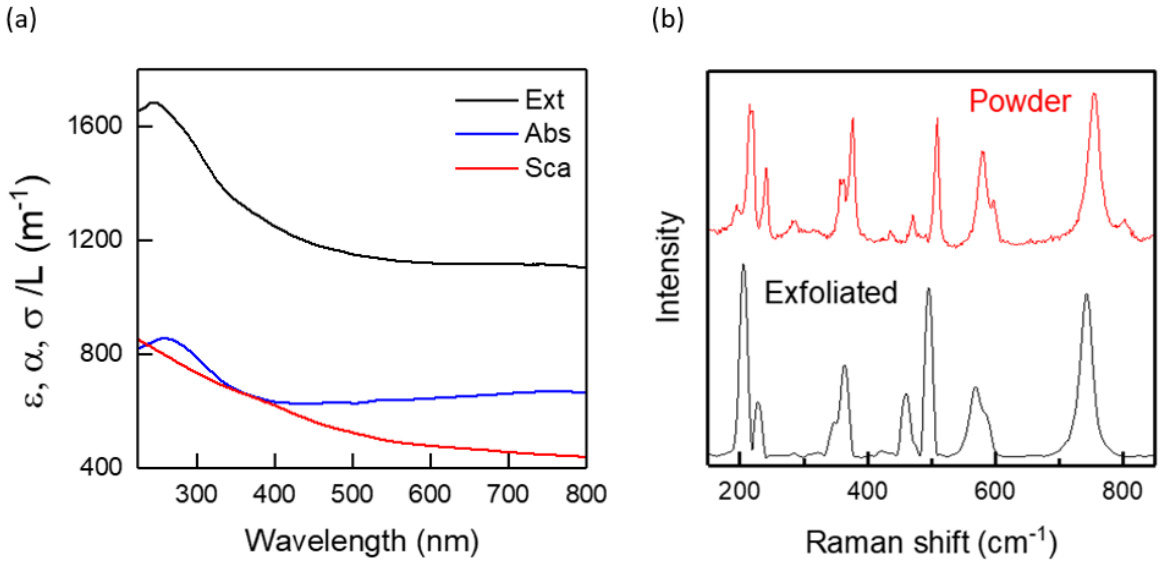

Figure 3.11: (a) Extinction, absorption and scattering spectra for MoO_2 standard sample dispersion. (b) Raman spectra comparison between bulk powder as received (red) and exfoliated nanosheets (black).

3.4 Size Selection of MoO_2 Nanosheets:

A great advantage of liquid phase exfoliation is that the nanosheets can be readily size selected and thus separated into fractions containing nanosheets of distinct length/thickness.[68, 78, 92, 94, 150-152, 154] This is of great importance as most applications require control of the lateral dimensions and thickness of nanosheets, e.g. small nanosheets for catalysis[151, 156] and large nanosheets for mechanical reinforcement.[157] To achieve this, liquid cascade centrifugation[94] was performed on the standard sample of MoO_2. This method involves a number of sequential centrifugation steps, each using an increased centrifugation speed, to isolate nanosheets in different size ranges (see Experimental section).[94] Here, we produced six distinctive sizes of nanosheets.

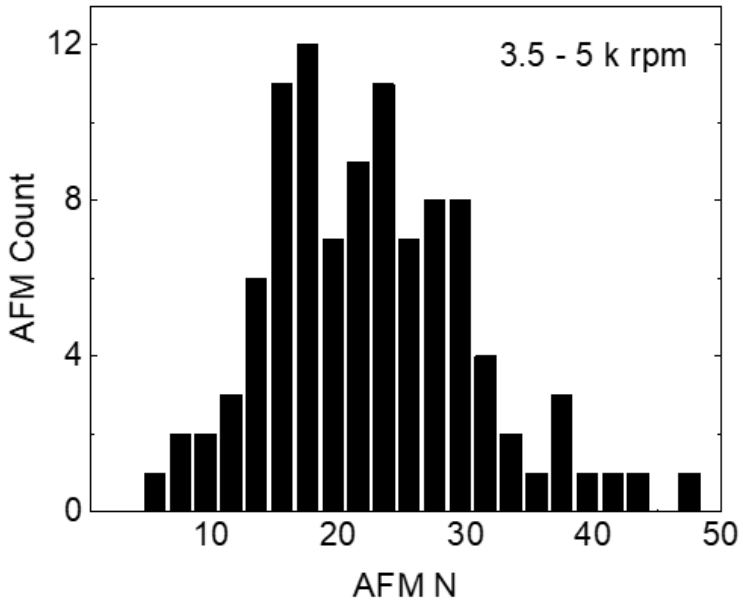

Figure 3.12: Thickness distribution of nanosheets in the 3.5 – 5 k rpm size fraction.

Initially, AFM was performed on the smallest fraction to demonstrate the lower limit of the size distribution of the standard sample. To do this 0.1 ml of dispersion was deposited on to a silicon wafer placed on a hot plate to remove residual solvent. A histogram is shown in Fig. 3.12 showing nanosheets with <N>=25. We note that while this value is considerably thinner than the standard sample (Fig 3.10(c)), these nanosheets are not particularly thin compared to results obtained for other 2D materials produced in a similar manner,[150, 154] suggesting MoO_2 to be a relatively difficult material to exfoliate.

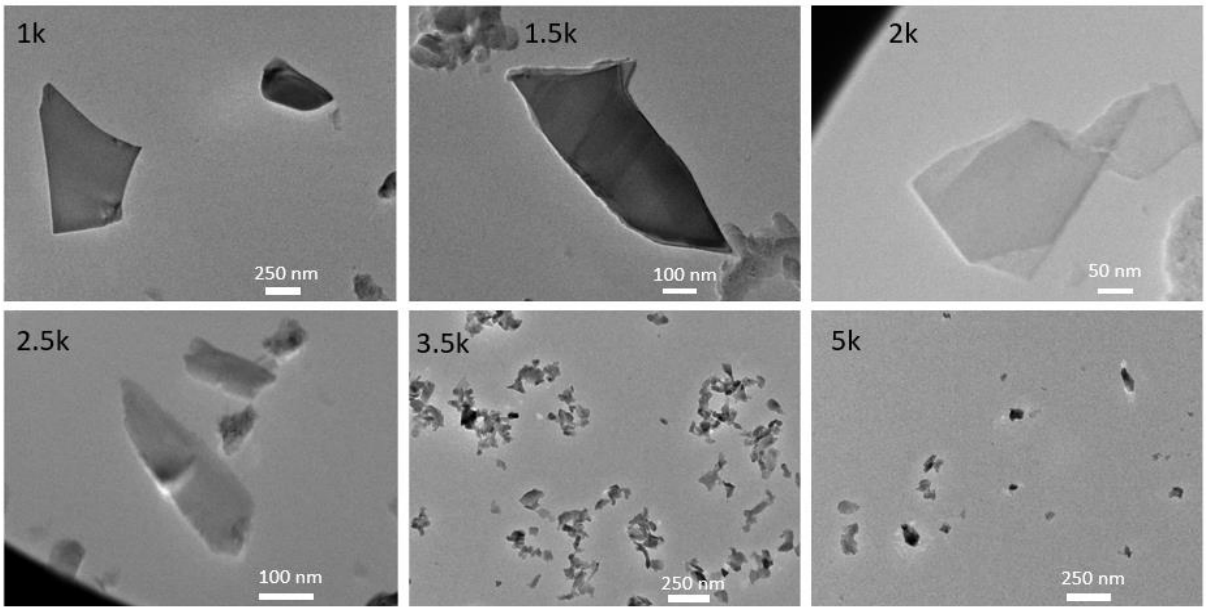

Figure 3.13 Representative TEM images for different size selected samples.

To ensure that the cascade had been successful in creating a range of sizes, as well as determining the average length of the nanosheets for each fraction, TEM was performed by pipetting a few drops of each dispersion onto holey carbon grids. As demonstrated in

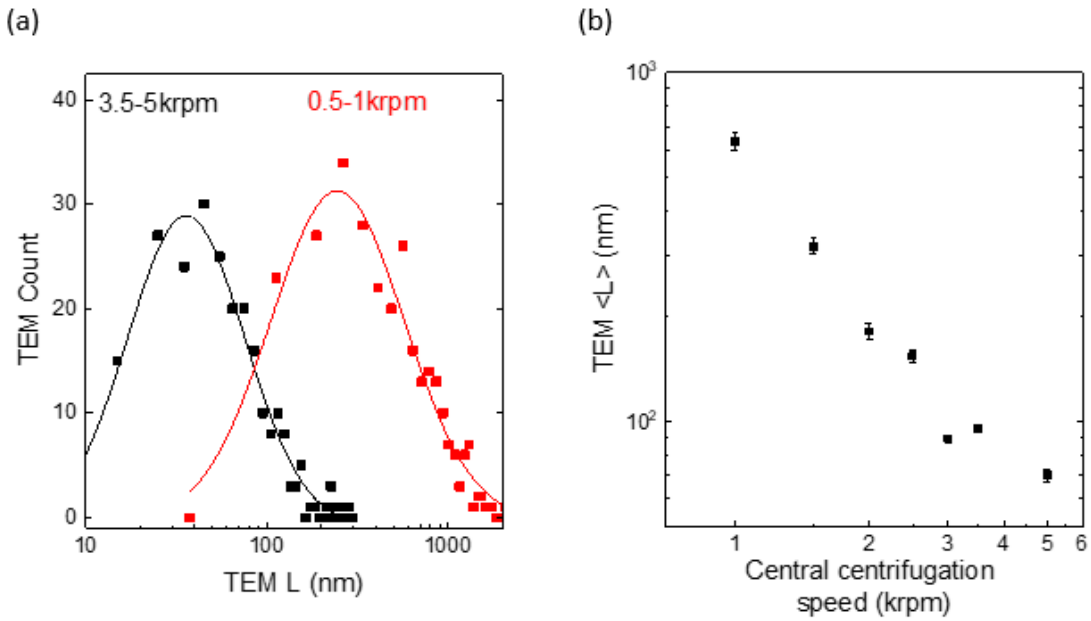

Figure 3.14: (a) Flake size distributions for the 3.5 – 5 k rpm and 0.5-1 k rpm, (b) Average flake length from TEM vs central centrifugation speed.

Fig. 3.13 where representative images of the different size fractions are shown, this resulted in well-exfoliated nanosheets ranging in size from microns to tens of nanometers.

For each of the size fractions the lengths of individual flakes were measured using software called ImageJ. Statistical analysis was also performed, shown in Fig. 3.14(a) are representative of the 0.5-1 krpm and 3.5-5 krpm fractions. Both show a log-normal distribution with the average shifted to much larger lengths for 0.5-1 krpm compared to the 3.5-5krpm sample, as expected. To demonstrate the success of the centrifugation process a graph of mean nanosheet length, <L>, (as measured by TEM) plotted vs central centrifugation speed is shown in Fig. 3.14(b) This shows <L> to vary by over an order of magnitude over the range of speeds explored. The individual size distributions are represented in histograms in Fig. 3.15. Sequential steps of cascade centrifugation result in a significant reduction in the width of flake length distribution due to the extraction of nanosheets of a similar size and thickness.

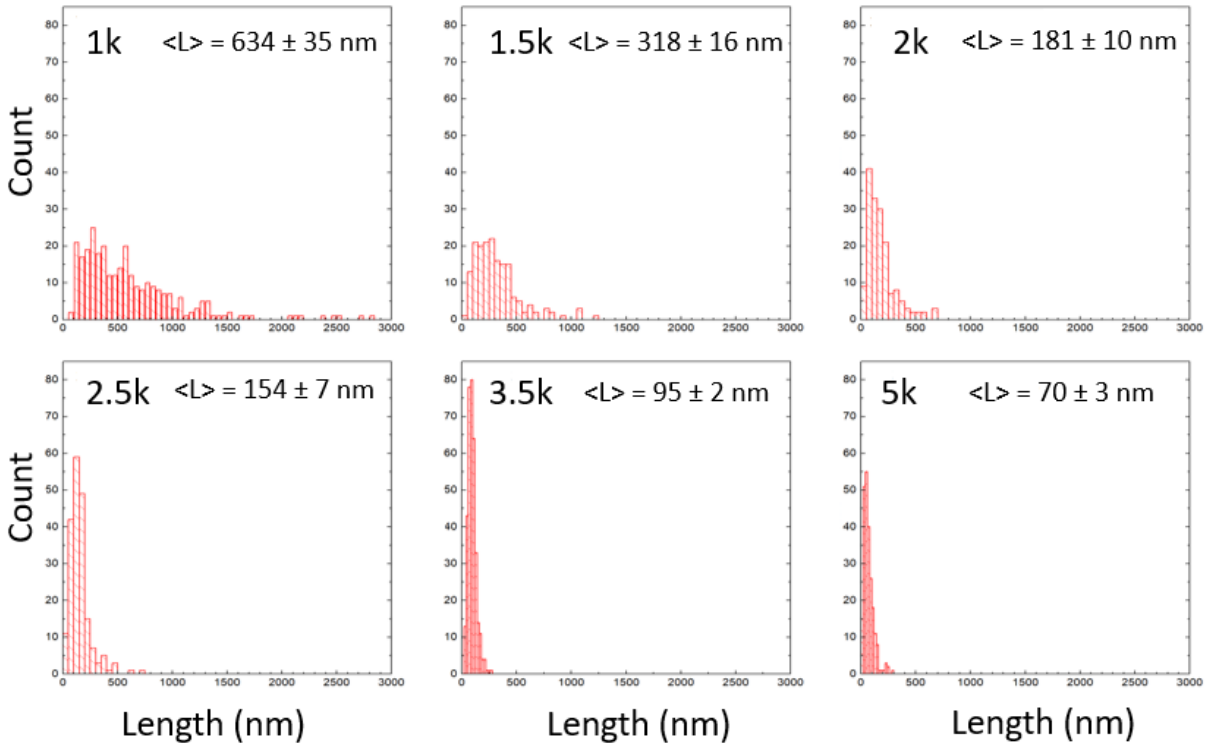

Figure 3.15: Histograms describing flake size distribution for size selected samples.

As discussed in Section 2.3, the optical properties of 2D materials are influenced greatly by the dimensions of the nanosheets. The extinction (ε), absorption (α) and scattering (σ) spectra were measured for each fraction using a uv-vis spectrometer with an integrating sphere attachment, and the normalized spectra are shown in Fig. 3.16 There is a clear change in shape for the extinction spectra with increasing size of the nanosheets in dispersion. Scattering effects are significantly more pronounced in samples containing larger nanosheets, consistent with previous works. Additionally, the absorption coefficient is also dependent on the size of the nanosheets. For smaller size fractions the ratio of edge sites to bulk is much higher than for the larger sizes. As a result these edge sites have a larger significant contribution to the absorption coefficient.[68, 152]

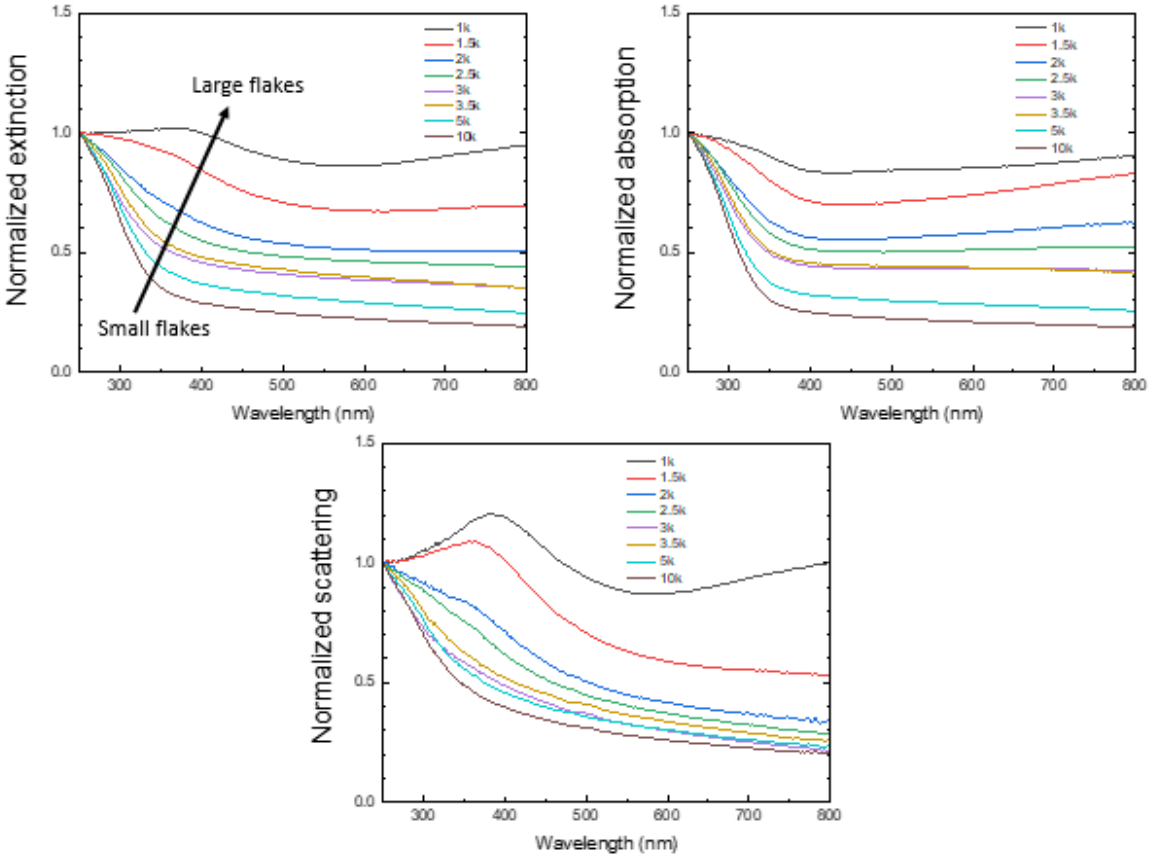

Figure 3.16: Normalized extinction, absorption and scattering spectra for size selected MoO_2 dispersions.

The development of spectroscopic metrics using the method described in section 3.2 ensures that for all subsequent dispersions of MoO_2 nanosheets, an estimation of the length and concentration can be readily acquired from UV-vis analysis alone, reducing the need for the more expensive and labour intensive determination from electron microscopy and filtration respectively.

3.5 Stability:

In some cases, the chemical composition of materials exfoliated and stored in liquid have been observed to change over time through reactions with water or oxygen, either from storage in ambient atmospheric conditions or contact with these species present in the solvent.[152] With the exfoliation of any new layered material it is important to examine the composition of the dispersed sample both immediately after production (fresh) and after the passage of time (aged). X-ray photoelectron spectroscopy (XPS) is a technique which provides an insight into the composition of a given material, and so was used to analyze a film of MoO_2 produced via vacuum filtration of a standard sample dispersion.

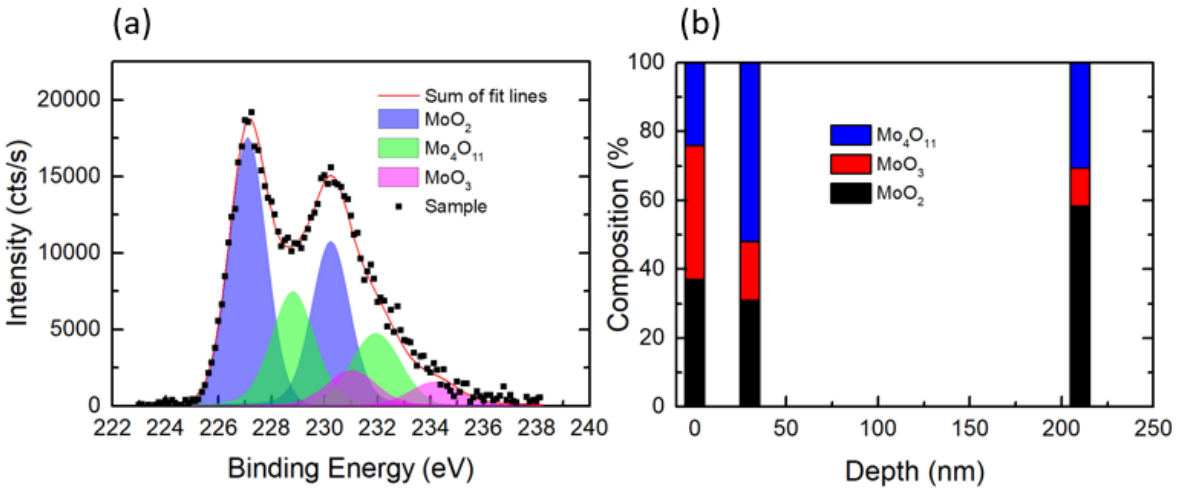

Figure 3.17: (a) XPS spectrum of MoO_2 film showing contributions of Mo oxides. (b) Variation of material composition with depth.

Fig. 3.17(a) shows the measured XPS spectrum of the sample and its fitted components. The sum of these fits is also shown for comparison with the observed spectrum. It is immediately apparent that there are oxides of molybdenum other than MoO_2 present in the material. XPS is a surface sensitive technique so the film was sputtered to give an indication of the compositional change with depth. This variance is shown in Fig. 3.17(b), showing that the MoO_2 content is increased significantly below the exposed surface of the film.

This XPS measurement was carried out approximately one week after the film was made because the group performing the analysis were not based in TCD. Additionally, the MoO_2 dispersion used was days old, having been subjected to other tests prior to sample preparation for XPS. Naturally, any delay between the film preparation and measurement

is problematic when attempting to track any degradation or compositional change. Combining this with the inability of XPS to accurately provide analysis beyond the surface layer it was decided that other characterization methods such as Raman and UV-vis spectroscopies would be used.

Shown in Fig 3.18(a) (black curve) is a Raman spectrum of a newly prepared film of MoO_2 nanosheets prepared from a fresh (1 day old dispersion). A number of lines can be seen in the range of ~200 to ~800 cm^{-1}, all of which can be assigned to MoO_2. However, this situation changes somewhat when the dispersion is allowed to stand in ambient conditions for a number of days before film preparation. As illustrated by the red curve, which shows a spectrum collected from a freshly-made film prepared from a 10 day old dispersion, aging results in the appearance of multiple new lines. This can be most clearly seen in the 800-1100 cm^{-1} spectral window, where a series of new features appear. These features can be assigned to high oxides of molybdenum with the peaks at 796 and 896 cm^{-1} for example associated with Mo_4O_{11}.[158]

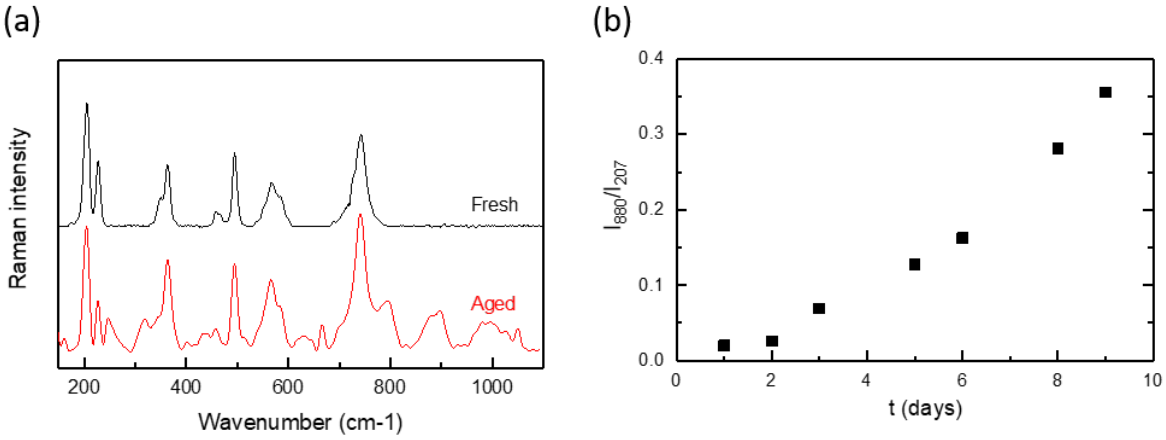

Figure 3.18: (a) Raman spectra of film prepared from a fresh (black) and aged (red) MoO_2 dispersions. (b) Ratio of intensity of peak at 880 cm^{-1} to that at 207 cm^{-1} plotted vs time.

The appearance of these new peaks is indicative of the oxidation of MoO_2 to higher oxides such as Mo_4O_{11} and MoO_3.[159] The evolution of this process can be tracked by measuring Raman spectra on freshly prepared films, made from dispersions which had stood in ambient conditions for various times. Plotted in Fig. 3.18(b) is the ratio of the intensity of the 880 cm^{-1} peak (representing Mo_4O_{11}) to that at 207 cm^{-1} (representing MoO_2),[160] plotted versus the time the dispersion spent standing after exfoliation. This shows a well-defined increase, indicating a continuous oxidation process.

An attempt was made to confirm the oxidation of MoO_2 to higher oxides over time using XRD, shown in Fig. 3.19. The bulk powder and freshly dispersed nanosheets display the expected MoO_2 lines. In addition to these MoO_2 lines, very weak signals consistent with Mo_4O_{11} were seen in an aged sample which had been allowed to stand in IPA for 60 days. It is unclear why the higher oxides are only weakly observable using XRD. However, it may be that they actually contribute a smaller mass fraction than suggested by optical spectroscopy.

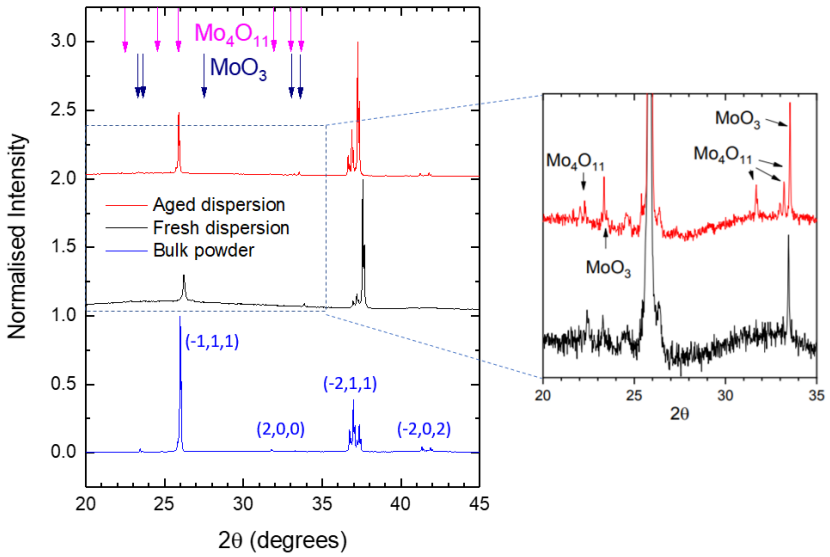

Figure 3.19: XRD spectra of bulk powder (blue), a fresh dispersion (black) and an aged dispersion (red).

The magenta and navy arrows at the top represent the positions of the main lines for Mo_4O_{11} and MoO_3 as reported in literature.[78]

The oxidation process can be tested quantitatively by measuring the optical absorption spectra (with scattering removed) of MoO_2 dispersions as a function of time after dispersion preparation (the dispersion was shaken before each measurement to remove any sedimentation effects). A subset of such absorption spectra (normalized to cell length, *l*) are shown in Fig. 3.20(a). From this data, it is apparent that subtle shape changes are occurring over time. This can be seen more clearly by plotting the spectra collected after 1 and 504 h together in Fig. 3.20(b), with both curves normalized to the absorbance at 800 nm. It is clear from this plot that the spectral shape is invariant with time in the range ~350 to >800 nm. However, for λ<350 nm, there is a clear increase in absorbance over

time. This can be seen clearly by plotting the difference between these (normalized) spectra in Fig. 3.20(b) inset.

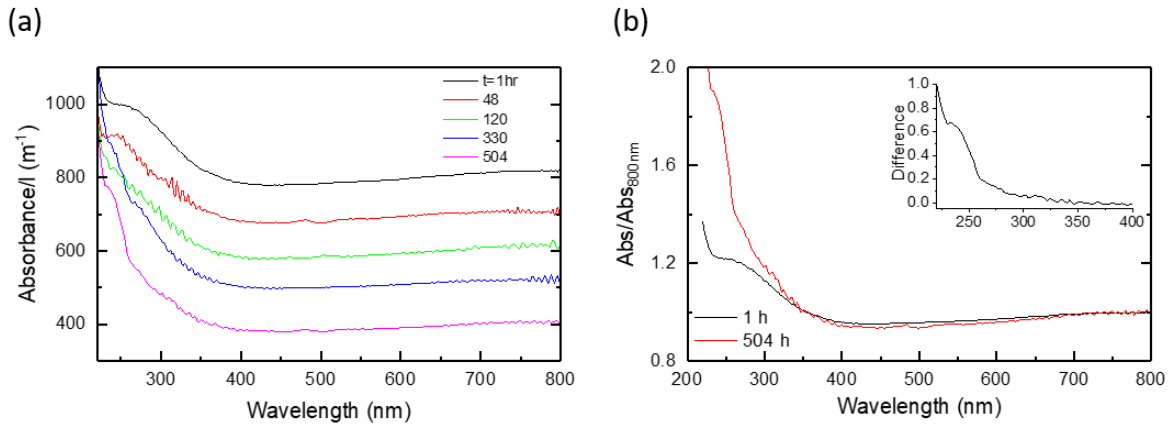

Figure 3.20: (a) Multiple absorbance spectra for a standard sample dispersion taken over a period of approx. 500 hours. (b) Absorbance spectra at 1 hour and 504 hours, each normalized to 800 nm, and difference between the spectra (inset).

This data is interpreted as follows. MoO_2 is expected to be metallic[161] as evidenced by the plateau in absorbance at high wavelength.[23] However, oxidation of MoO_2 should result in the formation of structures such as MoO_3 which is semiconducting[162]. Thus, one would expect oxidation to result in the transfer of absorbance from the high wavelength regime to the low wavelength regime. This is exactly what is observed in Fig. 3.20. The time dependence of this process can be analyzed by plotting the cell-length-normalized absorbance at 800 nm, which we label $A_{M,800nm}(t)/l$ (representing metallic MoO_2), versus time in Fig. 3.21. A clear exponential-like decay is seen, indicating that the concentration of MoO_2 falls with time. If this is due to the oxidation of MoO_2 to give semiconducting higher oxides, then this mass loss should be balanced by an increase in oxide concentration as evidenced by the relative absorbance increase at low wavelength. To quantify this it is noted that at t~0, the absorbance at 250 nm was 1.2 times the absorbance at 800 nm. Assuming this relationship is representative of MoO_2, this means the absorbance due to the growing concentration of higher oxides can be represented by

$$A_{O,250nm}(t)/l = A_{250nm}(t)/l - 1.2A_{M,800nm}(t)/l \qquad (1)$$

This parameter is plotted versus time in Fig. 3.21 and shows a well-defined increase with time.

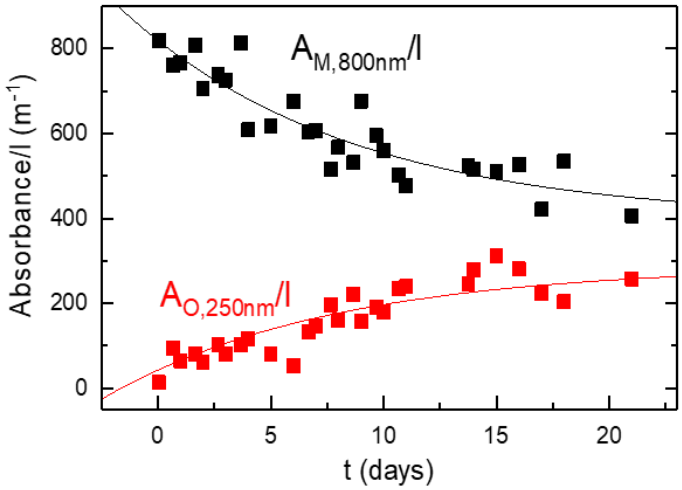

Figure 3.21: Absorbance at 800 nm corresponding to metallic MoO_2 (black) and oxide content (red) normalized to path length plotted against time. R-square = 0.82. See appendix for fitting data.

This data can be analysed as follows.

Assume that there are two populations of Mo atoms, those incorporated into MoO_2 (M) and those in higher oxides (O). Assuming the total number of Mo atoms, *n*, is constant allowing us to write:

$$n = n_M + n_O \tag{2}$$

For both MoO_2 and higher oxides, it is assumed that the absorbance per unit cell length scales with the total number of Mo atoms in each material type via a proportionality constant, σ, $A_M / l = \sigma_M n_M$ and same for O such that

$$n = \frac{A_M / l}{\sigma_M} + \frac{A_O / l}{\sigma_O} \tag{3}$$

This allows the absorbance associated with the oxide content to be written as

$$A_O / l = \sigma_O n - \frac{\sigma_O}{\sigma_M} A_M / l \tag{4}$$

This predicts that the absorbance of the oxide component should scale linearly with that of the metallic MoO_2, which is found to be true as shown in Fig. 3.22 for the $A_{O,250nm}/l$ vs $A_{M,800nm}/l$ data. From the slope of this graph, the ratio $\sigma_{O,250nm}/\sigma_{M,800nm}$ = 0.58 is found.

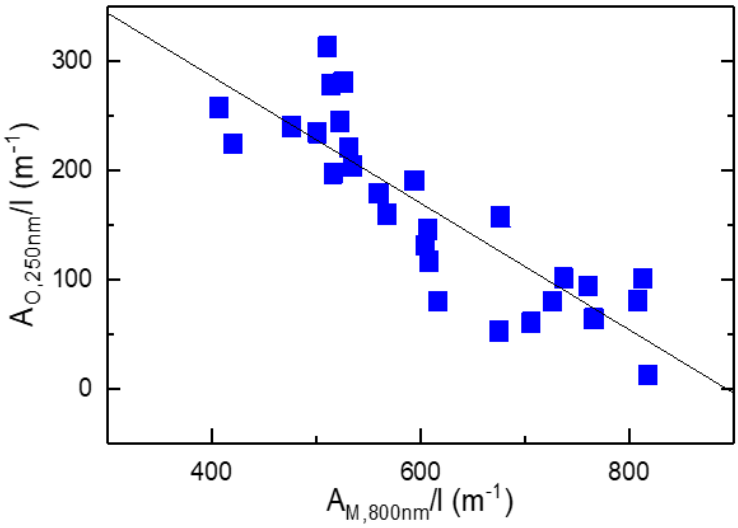

Figure 3.22: Higher oxide absorbance at 250 nm vs metallic absorbance at 800 nm, both normalized to path length. R-square = 0.74. See appendix for fitting data.

Then, approximating the $A_{M,800nm}/l$ data using an exponential decay:

$$A_{M,800nm}/l = a + be^{-t/\tau} \tag{5}$$

Allows an expression for the higher oxide absorbance at 250 nm to be written:

$$A_{O,250nm}/l = \sigma_O n - \frac{\sigma_O}{\sigma_M}(a + be^{-t/\tau}) \tag{6}$$

The last two equations have been used to fit the data in Fig. 3.22 and loosely tracks the trend of the experimental results in both cases with the same time constant of 243 h and yielding b=423 m^{-1} and a=396 m^{-1}. These results show that the absorbance spectra are consistent with the idea that the metallic MoO_2 converts to a semiconducting product over time. However, the process is slow enough to allow exfoliation and processing to be

carried out before any significant oxidation has occurred (Loss of approximately 15 % after 100 hours).

The data above implies that MoO_2 is unstable against oxidation when suspended in IPA. However, this does not necessarily mean that MoO_2 nanosheets are unstable when removed from the solvent. To test this, a fresh dispersion was prepared and rapidly filtered through a porous membrane to form a film which was then dried and stored in ambient conditions i.e. with full exposure to air and without any form of temperature regulation.

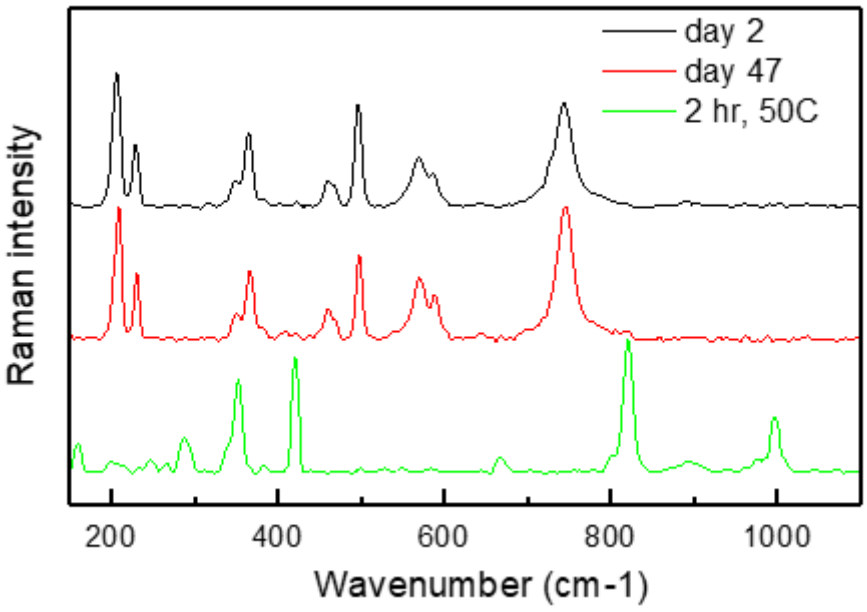

Figure 3.23: Raman spectra for MoO_2 films at 2 days (black) and 47 days (red) stored at ambient conditions, and the spectrum for a film heated for 2 hours at 50 °C.

Shown in Fig. 3.23 are Raman spectra measured on this film 2 days (black) and 47 days (red) after film formation.

Both spectra were found to be consistent with MoO_2 with no evidence of higher oxide formation. However, when a freshly prepared film is heated to 50 °C for 2 h in ambient conditions, strong evidence of higher oxides is found (above 800 cm^{-1}) as illustrated by the green spectrum. This indicates that air-stable MoO_2 nanosheets can be produced once the exfoliation/preparation process is performed rapidly and the resultant structures are not exposed to high temperatures.

3.6 Batteries:

A number of papers have demonstrated MoO_2 to be a promising lithium storage material which has a theoretical capacity of 836 mAh/g MoO_2 based on phase transitions and a conversion reaction.[163-165] The theoretical storage capacity is calculated as follows:

$Capacity = \frac{Q}{M} = \frac{nF}{M}$ where M is molecular mass, F is the Faraday constant and n is the number of charges from the lithium intercalation equation.[166]

In the past, films of MoO_2, which were synthesised in various ways, have been formed into lithium ion battery anodes with maximum capacities[163, 165, 167, 168] as high as ~1200 mAh/g, considerably beyond theoretical expectations. The theoretical capacity is calculated from the Li-ion intercalation reaction and the conversion reaction. However, there is often more surface area available in nano-materials and the Li might also be stored in the surface of some materials which functions almost as "extra capacity". In addition, two papers[142, 164] report "anomalous" capacity of up to 1800 mAh/g which has been explained via a Li-storage mechanism consisting of a Li-ion intercalation reaction and the formation of a metallic Li-rich phase between the Li-ion-intercalated MoO_2 phase. It has been suggested that this mechanism strongly depends on the amount of accessible surface area present.[164]

However, in all previous reports the MoO_2 was prepared by chemical methods such as hydrothermal synthesis.[167] Because of its simplicity and scalability, liquid phase exfoliation is an attractive alternative method for producing MoO_2 for electrode applications. This method has advantages in that it facilitates the addition of nano-conductors by solution mixing and allows simple, liquid-based film formation techniques. As liquid-exfoliated MoO_2 nanosheets have never been tested for Li storage, their potential for use in this application area is unknown.

To test this, lithium ion battery anodes were produced using liquid-exfoliated MoO_2 nanosheets. All battery measurements and analysis were carried out by Dr Ruiyuan Tian. To promote electrical conductivity as well as mechanical robustness,[169] 20 wt% single wall nanotubes were added as both conductive additive and mechanical binder. Basic electrochemical characterization was performed with galvanostatic charge−discharge curves and capacity versus cycle number data shown in Fig. 3.24(a) and (b). It was found that MoO_2–based electrodes (with a mass loading of 0.2 mg/cm^2 MoO_2) showed good

lithium storage capability. Measuring at a specific current of 0.1 A/g, the initial discharge and charge capacity were 1150 and 546 mAh/g, respectively, yielding a 47.5% Coulombic efficiency. The discharge and charge capacities were 635 and 531 mAh/g respectively for the 2nd cycle (with 83.7% CE) with the irreversible capacity loss after the first cycle being due to the formation of a solid electrolyte interface.[163, 165, 167] Interestingly, the discharge and charge capacities gradually increased to 1141 and 1085 mAh/g (with 95% CE) over 170 cycles (Coulomb efficiency is plotted versus cycle number in the inset). The low coulombic efficiency observed in the first cycle is typical of transition metal oxides,[163-165, 167, 170] and is due to the formation of a solid electrolyte interface and electrolyte degradation.

After about 120 cycles, the capacitance values are comparable with those of the best non-anomalous MoO_2 electrodes reported (up to 1200 mAh/g).[163, 165, 167, 168] It is particularly interesting that the capacity increases steadily with cycling. This has been observed by a number of authors for MoO_2[165, 168] and has been attributed to the increase in and activation of surface area, which happens in discharge/charge and is caused by the separation of stacked layers during the process, improving the ability to store lithium ion and Li metal.[164]

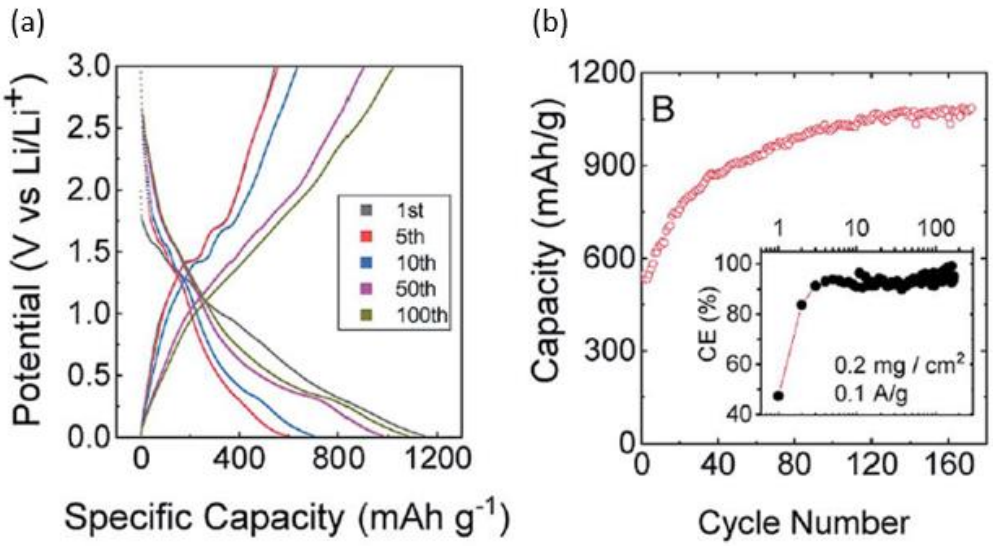

Figure 3.24: (a) Galvanostatic charge-discharge curves up to 100 cycles. (b) Capacity vs cycle number, with coulombic efficiency vs capacity inset.

The performance can be understood in more detail by studying differential capacity curves (dQ/dV) obtained by differentiating charge/discharge curves such as those shown

in Fig. 3.24(a). Both dQ/dV and cyclic voltammetry data have been reported and discussed in detail for MoO_2.[168, 171, 172] Shown in Fig. 3.25(a)-(e) are differential curves associated with cycles 1, 5, 10, 50 and 100. This evolution of the differential capacity with cycle number is closely aligned with previous reports,[171] with the main features being oxidation peaks at 1.4 and 1.7 V and reduction peaks at 0.3, 1.3, and 1.6 V. The two sets of redox peaks at 1.3 V/1.4 V and 1.6 V/1.7 V are associated with the insertion of lithium into MoO_2 to yield $LiMoO_2$ and the accompanying monoclinic to orthorhombic to monoclinic phase transition.[173] In addition, there is a sharp reduction peak at 0.3 V (accompanied

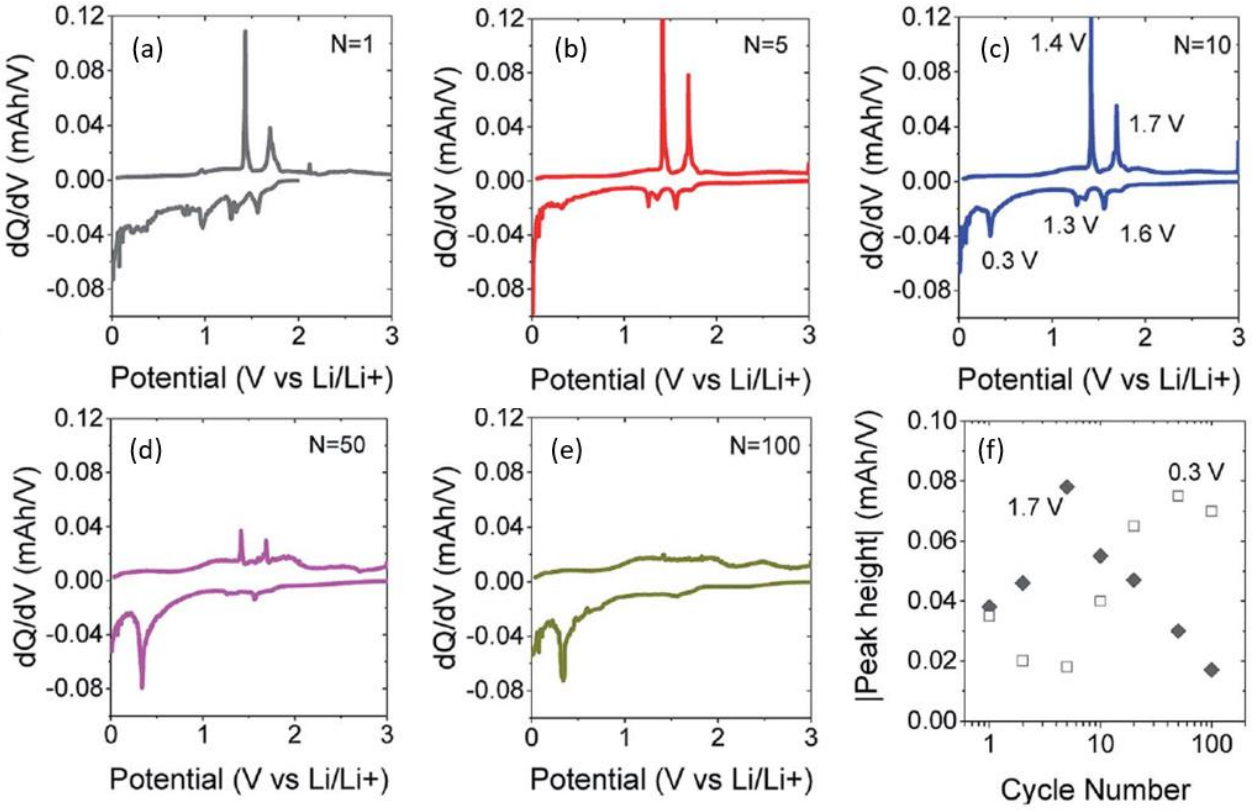

Figure 3.25: (a)-(e) Differential capacity curves from differentiation of charge-discharge curves for various cycle numbers(N). (f) Insertion peak vs cycle number.

by a broad oxidation peak at approx. ~0.5 V) associated with the conversion of $LiMoO_2$ to Li_2O ($LiMoO_2 + 3Li^+ + 3e^- \rightarrow Mo + 4Li_2O$). While the insertion reaction has a theoretical capacity of 209 mA h g^{-1}, the conversion reaction has a significantly larger theoretical capacity of 627 mA h g^{-1}.[171] In line with previous results,[168, 171, 172] it was found that the insertion peaks decrease with cycling while the conversion peak increases with cycling (Fig. 3.25(f)). It has previously been suggested that cycling opens up the layered

crystal, increasing the active surface area and hence the capacity.[164] This process may also be responsible for the simultaneous changes in insertion and conversion peaks. For example, a more open material with greater surface area may be more amenable to conversion.

The rate performance of the electrodes was also tested, as shown in Fig. 3.26, although such data is complicated by the increase in capacity with cycle number shown in Fig. 3.24(b). These electrodes exhibited an initial performance of 943 mAh/g for discharge and 679 mAh/g for charge at 0.05 A/g. At 0.1 A/g, the capacity is 673 mAh/g for discharge and 632 mAh/g for charge, with an increase to 978 and 950 mAh/g after 30 cycles. Furthermore, the composite electrode is capable of fast charge and discharge. When the specific currents were increased to 0.2, 0.4, and 0.8 A/g, specific charge capacities of 928, 898, and 851 mAh/g respectively, are reversibly delivered. And when the current rate went back to 0.1 A/g, the specific charge capacities could even achieve 983 mAh/g. Again, these results are competitive with the best reports of non-anomalous MoO_2.[168]

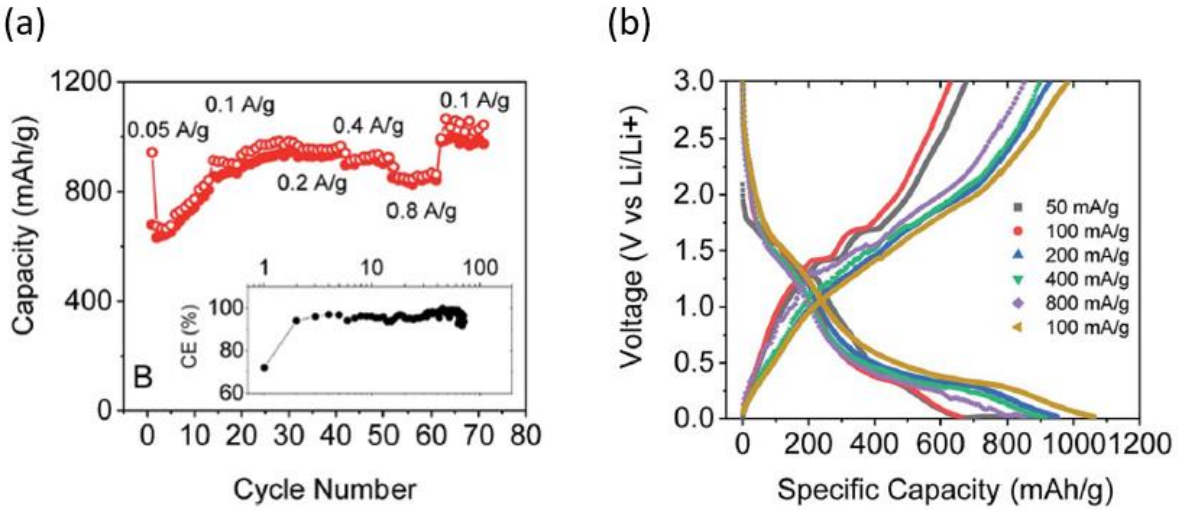

Figure 3.26: Rate performance of MoO2 electrodes.

All the battery data above indicates that the exfoliated MoO_2 flakes with CNTs are capable of high specific capacity and excellent cyclability. We attribute the outstanding lithium storage performance of the MoO_2/CNTs nanocomposite to the following factors:

(1) High surface area leads to a large lithium storage capacity. (2) The pathway for Li^+ diffusion is significantly reduced on exfoliation compared to bulk MoO_2, thus the rate capability is improved. (3) The CNT network not only provides good conductivity, but also keep the structure of the electrode films stable upon cycling, hence the excellent cycling stability observed is achievable.

3.7 Conclusions

In conclusion, the production of MoO_2 nanosheets using liquid phase exfoliation has been demonstrated. It is apparent that the resulting nanosheets are somewhat unstable and are oxidized over a period of days when dispersed in isopropanol under ambient conditions. However, it was found that processing the nanosheets into films quickly after exfoliation dramatically slows oxidation (unless the films are heated under ambient conditions). In addition, it has been shown that molybdenum dioxide nanosheets can be size selected via controlled centrifugation. The optical properties were observed to vary significantly with nanosheets size, as with other 2D materials. This allowed the development of spectroscopic metrics for the estimation of concentration and mean nanosheet size from extinction spectra. Finally, MoO_2 dispersions tested for application in Li ion batteries exhibited good storage capacity (up to 1140 mAh/g), comparable to that of the best non-anomalous MoO_2 electrodes.

3.8 Experimental Approach

Material:

Molybdenum dioxide powder (99%) was purchased from Sigma Aldrich and was used as received. When not in use, the MoO_2 powder was stored in a glovebox in Argon to prevent exposure to O_2/H_2O and subsequent oxidation.

Production of MoO_2 Nanosheets:

MoO_2 powder was sonicated in a solvent using a horn-probe sonic tip (Vibracell CVX, 750 W) at 60 % amplitude in an aluminium cup with 80 mL isopropanol (IPA) at a MoO_2 concentration of 20 mg/mL. The dispersion was sonicated for 6 hours with a 6s/2s on/off pulse ratio and ice cooling was used to prevent boiling off of the solvent. Once sonicated the dispersion was centrifuged using a Hettich Mikro 220R centrifuge equipped with a fixed angle rotor (where RCF = 106.4(kRPM)^2). The dispersion was centrifuged for one hour at 500 rpm (26.6 g) to extract unexfoliated material and then at 5000 rpm (2660 g) to remove extremely small nanosheets. The sediment from the 5000 rpm step was then redispersed using bath sonication. A sample produced in such a manner is referred to as a standard sample.

A comparative experiment was carried out to identify the optimal solvent for exfoliating the material. Aliquots of each solvent (20 mL) were used to exfoliate MoO_2 with an initial concentration of 5 mg/mL for 30 minutes using a tapered tip at 25 % amplitude. The resulting dispersion was then centrifuged at 2500 rpm (665 g) for 2.5 hours, and the sediment was discarded. Spectroscopic analysis of each dispersion using UV Vis allows the concentration of the dispersions to be measured and plotted as a function of Hildebrand solubility parameter. List of solvents used: Deionised Water (δ = 47.5 MPa$^{1/2}$), Isopropanol (δ = 23.6 MPa$^{1/2}$), Acetone (δ = 19.9 MPa$^{1/2}$), N-Cyclohexyl-2-pyrrolidone (δ = 20.5 MPa$^{1/2}$), N-Methyl-2-pyrrolidone (δ = 23 MPa$^{1/2}$), Pentane (δ = 14.4 MPa$^{1/2}$), Dimethylformamide (δ = 24.9 MPa$^{1/2}$), Methanol (δ = 29.6 MPa$^{1/2}$), Hexane (δ = 14.9 MPa$^{1/2}$), 2-Isopropoxyethanol (δ = 21.4 MPa$^{1/2}$), 1-Dodecyl-2-pyrrolidinone (δ = 18.8 MPa$^{1/2}$). To determine the optimal sonication time a dispersion of MoO_2 in IPA (80 mL) at an initial concentration of 20 mg/mL was prepared and sonicated. Aliquots were removed after fixed sonication times (0.5, 1, 3, 4, 6, 8, 24 hours) and each was centrifuged between 500 and 5000 rpm. The concentration of each sample was attained from absorption spectroscopy and plotted against sonication time.

Size Selection:

Dispersions of MoO_2 in IPA were size selected using Liquid Cascade Centrifugation,[94] a technique consisting of multiple centrifugation steps with incremental increases in rpm. After each centrifugation step the supernatant was decanted and was used for the subsequent centrifugation step. The sediment was redispersed and labelled as appropriate. Note that the 1k sample refers to the redispersed sediment from the sample centrifuged at 1k rpm.

Film Preparation:

Preparation of the films for battery electrodes was carried out by Dr Ruiyuan Tian.

The MoO_2 dispersions mixed with SWCNTs[174] were vacuum-filtered using porous cellulose filter membranes (MF-Millipore membrane mixed cellulose esters, hydrophilic, 0.025 μm, 47 mm) to give thin films with 20 wt.% SWCNTs. 0.1 $mg.mL^{-1}$ dispersions of SWCNT were prepared by dispersing 10 mg of P3-SWCNT in 100 mL of IPA for one hour in a Fisherbrand Ultrasonic Dismembrator (30 W, 40 % amplitude). The mass loading of these films was controlled by the volume of dispersion filtered.

The resulting films (diameter, 36 mm) were cut to the desired dimensions for electrochemical testing and then transferred to Cu foil using IPA to adhere the film to the substrate. The cellulose filter membrane was removed by treatment with acetone vapour and subsequent acetone liquid baths. The mass loading of MoO_2 is 0.5 mg/ cm^2 for rate capability measurement, and 0.2 mg/ cm^2 for cycling performance measurement.

Characterisation:

Optical characterisation was performed using a Perkin Elmer Lambda 1050 ultraviolet-visible spectrometer, equipped with an integrating sphere for measuring the absorption (the extinction with scattering effects removed), and a quartz cuvette with a path length of 4 mm.

A Horyba Yvon LabRam HR800 was used to acquire the Raman spectra. 632nm was chosen as laser line. Laser power was set to 0.2 mW in order to avoid sample degradation. No heating or degradation effects were observed at such power. A 100x objective focused

the beam in a ~2 μm diameter spot, a diffraction grating of 600 grooves per mm was used, obtaining a spectral resolution of ~1.2 cm^{-1}. All Raman analysis was carried out by Dr Victor Vega-Mayoral.

For solid samples, measurements were performed at room temperature. Due to the low Raman cross section 1200 s was chosen as acquisition time, and two spectra were averaged in order to obtain a single spectrum. Each map has an area of 20 μm × 20 μm and a step of 10 μm was used (25 measurements per map, 20 × 2 min per single spectra, 16.6 hours per map).

In situ liquid sample measurement was impossible. As long integration times were needed, the solvent evaporated during measurement causing defocusing. Instead a few hundred μL were drop casted and 8 to 10 spectra from manually selected spots were averaged to obtain the final spectra. 1500 s was chosen as measurement integration time and 3 spectra were averaged in each spot (10-12.5 h per sample).

AFM imaging was performed using a Veeco Nanoscope-IIIa from Digital Instruments. An E-head in tapping mode was used for all measurements. MoO_2 nanosheets dispersed in Isopropanol (IPA) were further diluted with IPA at a ratio of 1:5 (old sample) and 1:20 (fresh sample) and drop casted (10uL) on preheated (140C) Si/SiO2 wafers (0.25 cm2) with an oxide layer of 300 nm. After deposition wafers were rinsed with IPA and dried with compressed air prior to measurement. Typical image size taken was 8 um2 with 512 lines/ image and scan rates of 0.6 Hz. Measured thickness was corrected and then converted to number of layers based on conducted steep height analysis. AFM analysis was performed by Aideen Griffin and Dr Beata Szydlowska.

The nanosheets were imaged using a JEOL 2100 series Transmission Electron Microscope (TEM). Dispersions of MoO_2 were prepared for imaging by drop casting on holey carbon TEM grids (Agar Scientific). During the drop casting process the grids were placed on filter paper to absorb excess solvent. After imaging the lengths of nanosheets were recorded using ImageJ software and histograms of the flake size distribution were compiled. The longest dimension observed was designated as the flake length.

For X-ray photoelectron spectroscopy (XPS) measurements, a PHI VersaProbe III instrument equipped with a micro-focused, monochromated Al K-α source (1486.6 eV) and dual beam charge neutralization was used. XPS measurements were taken by Tanja Stimpel-Lindner. Core level spectra were recorded with a spot size of 100 μm and a pass

energy of 69 eV using PHI SmartSoft VersaProbe software, and processed with PHI MultiPak 9.8. Sputter depth profiling was conducted using 1 keV Ar^+ ions. Binding energies were referenced to the adventitious carbon signal at 284.8 eV. After subtraction of a Shirley type background, the spectra were fitted with Gaussian-Lorentzian peak shapes.

X-ray diffraction (XRD) measurements were performed in a Bruker Advance Powder X-ray diffractometer equipped with a Cu-Kα emission source in Bragg-Brentano configuration. Bulk MoO_2 powder was finely ground and directly deposited in a sample holder, and dispersion measurements were carried out on thin films prepared on a glass substrate. XRD was carried out by Sonia Jaskaniec.

Li-ion Battery Testing:

For the electrochemical measurements, metallic lithium foils (diameter: 14 mm, MTI Corp.) were used as the negative electrodes. The electrolyte used was 1 M $LiPF_6$ in a 1:1 (volume ratio) mixture of ethylene carbonate (EC) and dimethyl carbonate (DMC). A Celgard 2320 was used as the separator. The cells were assembled in a glovebox filled with highly pure argon gas (O_2 and H_2O levels < 1 ppm), and the electrochemical properties of the electrodes were measured within a voltage range of 3.0−0.01 V using constant current (CC) mode on an automatic batteries tester (VMP 3, Biologic). For rate capability measurement, cells were running at different current rates of 0.05 A/g, 0.1 A/g, 0.2 A/g, 0.4 A/g, 0.8 A/g, and then went back to 0.1 A/g. There is only 1 cycle at 0.05 A/g for activation, followed by 30 cycles at 0.1 A/g. Then there are 10 cycles for the next steps at different current rates. For cycling capability tests, the cells were performed at 0.1 A/g. All battery testing was performed by Ruiyuan Tian.

4

Liquid Phase Exfoliation of Germanium (II) Sulfide

4.1 Introduction

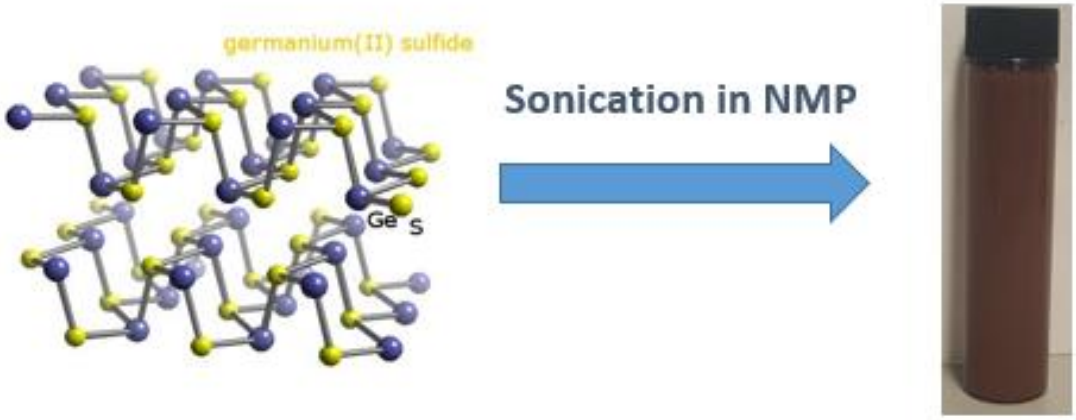

Figure 4.1: Structure of GeS monolayer and photo of a GeS dispersion in NMP.

The narrow band gap IV-VI semiconductor monochalcogenides with the formula MX where M = Sn/Ge and X = S/Se have attracted interest recently for applications in a number of areas.[175, 176] Germanium sulfide (GeS) is a compound of this family which is isoelectronic with and structurally similar to black phosphorus.[31] GeS has shown promise as a material for solar cells[175] and photodetectors.[32, 34] In particular,[37] because of its high theoretical lithium storage capability and solid state Li diffusion coefficient, GeS shows great promise for battery applications.[31, 177] The work described in this Chapter demonstrates the production of GeS nanosheets via liquid phase exfoliation in ambient conditions for the first time and their use as lithium ion battery electrodes.

Fig. 4.2 shows SEM images of the GeS bulk powder as received, showcasing its flake-like structure.

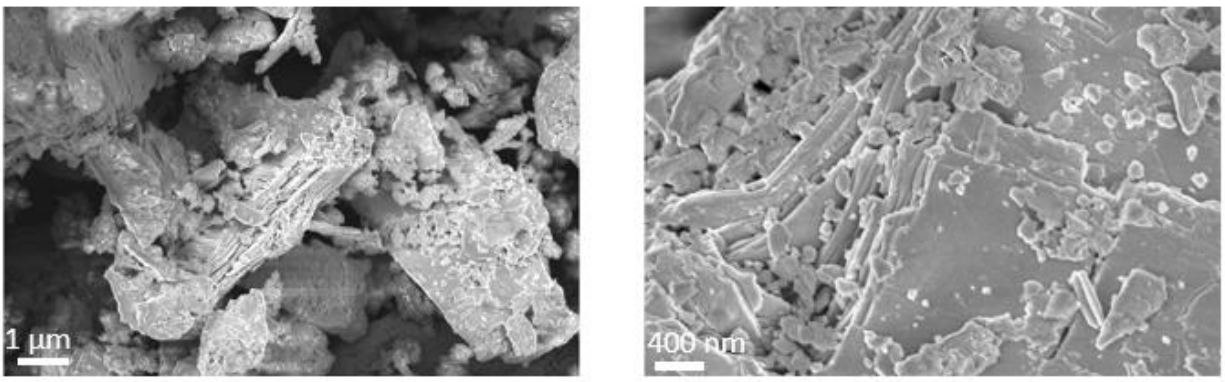

Figure 4.2: SEM images of bulk GeS powder.

Despite its potential, this material has not been studied comprehensively, most likely because of concerns about its stability. While there are conflicting reports about the stability of GeS in air, it is generally accepted that the presence of water causes the material to hydrolize[30], as discussed earlier. Such oxidative instability is often not a problem with layered materials as oxidation tends to be limited to the surface, leaving the bulk of the crystal unaffected.[178] Unfortunately, after exfoliation the extremely thin nature of nanosheets means that oxidation can proceed at an accelerated rate due to the increased available surface area.[179] To avoid this, Lam et al demonstrated liquid phase exfoliation of GeS in an inert atmosphere leading to high quality nanosheets[37]. However, the stipulation of sample preparation in argon makes the exfoliation process much more difficult and severely limits the scalability of the technique. It would be advantageous to demonstrate a viable method to produce GeS nanosheets by liquid phase exfoliation in ambient conditions. Previous work in our group showed that black phosphorous (BP) nanosheets could be produced by ambient liquid phase exfoliation in certain solvents such as NMP[152]. Under such circumstances, oxidation of the BP was much slower than expected, possibly because the NMP solvation shell acts as a protective layer. A similar approach was used for GeS, in the hope that these stabilizing effects could be replicated.

In a similar manner to the previous Chapter, the specific details of the experiments are included at the end, Section 4.7.

4.2 Exfoliation and Basic Characterization:

The previously established exfoliation protocol in the earlier work on MoO_2 resulted in stable dispersions, and so these same sonication and centrifugation parameters were used as a template for the exfoliation of GeS, with a few minor changes for optimization (see methods section). Briefly, 400 mg of GeS was sonicated in an aluminium vessel with 80 mL solvent. This lower initial concentration of 5 mg/mL for GeS (compared to 20 mg/mL for MoO_2) was chosen to offset the higher cost of the material. Following sonication, the dispersion was centrifuged twice, once at a low RPM to remove overly large unexfoliated material and at a high RPM to remove very small nanosheets.[94] A dispersion with a broad range of nanosheets sizes prepared in such a manner will be referred to as the 'standard sample' for the remainder of this work, as described in the previous Chapter.

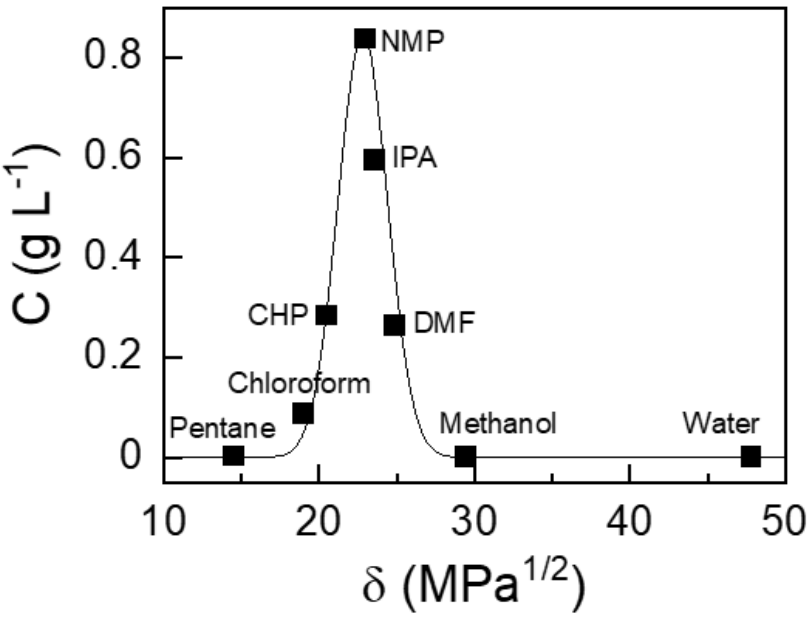

Figure 4.3: Dispersed concentration of GeS nanosheets vs Hildebrand solubility parameter for a range of solvents. R-square = 0.99. See appendix for fitting data.

To determine the best possible solvent a series of dispersions were made with different solvents in order to identify the optimal one for exfoliation. The concentration of the resultant dispersions was estimated using UV-vis extinction spectra (relationship devised in a similar manner to MoO_2, discussed in more detail in 4.4), yielding values between 0.01 and 0.84 mg/mL, with CHP, NMP and IPA showing the highest concentrations. Plotting this concentration versus the Hildebrand solubility parameter (Fig. 4.3) shows that the concentration is maximized when using solvents with a Hildebrand solubility

parameter between 20 and 23 $MPa^{1/2}$. This is similar to other liquid phase exfoliated 2D materials [68, 180].

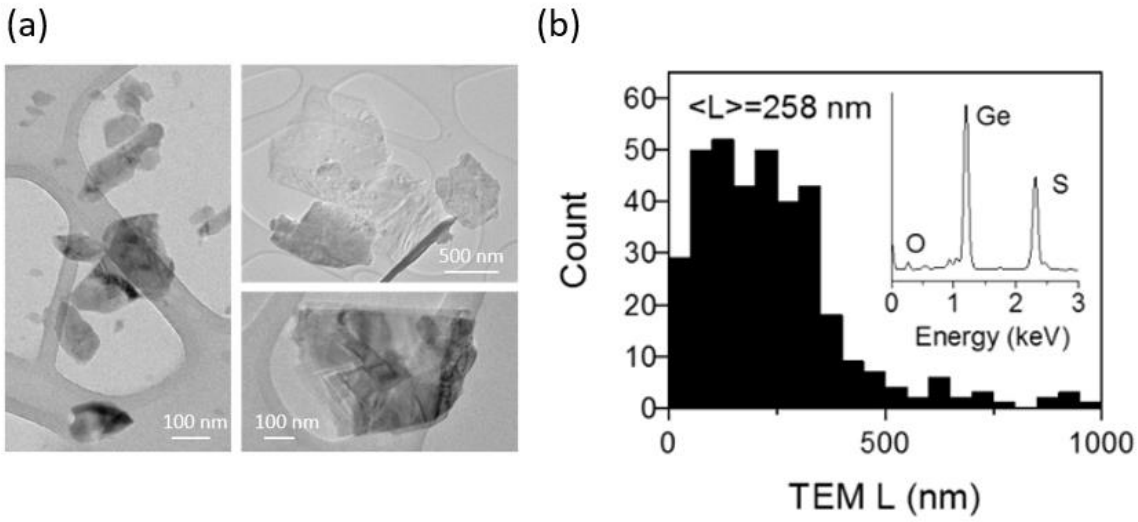

Figure 4.4: (a) Representative TEM images of standard sample dispersion. (b) Flake size distribution of nanosheets in the dispersion from TEM analysis, and EDX spectrum for 5-10 nanosheets (inset).

Previous work[152] has shown that NMP suspended nanosheets can be partially stabilized against oxidation, thus this solvent was used for all GeS dispersions produced thereafter.

To investigate the nature of the dispersed material, the standard sample of GeS in NMP was analyzed in more detail. TEM imaging determined that the dispersion contained well exfoliated, electron transparent nanosheets, with well-defined edges (Fig. 4.4(a)). Measurements of nanosheet length (the longest dimension) are plotted as a histogram in Fig. 4.4(b). The histogram shows the standard sample is quite polydisperse, containing nanosheets ranging in size from ~ 50 nm up to 1 μm with an average length of 258 ± 9 nm. A number of energy dispersive x-ray (EDX) spectra were also measured in the TEM with 5-10 nanosheets contributing to each spectrum (Fig. 4.4(b) inset). Averaging over all spectra, a Ge:S atomic ratio of 1.05 was found, with a small oxygen content, implying the freshly exfoliated flakes to be near pristine GeS.

In order to assess the degree of exfoliation, AFM analysis was performed on the standard sample. The flake length histogram (Fig. 4.5(a)) was reasonably consistent with the findings from TEM data although the mean was slightly lower at 209 nm. The nanosheet thickness, expressed as average number of stacked monolayers per nanosheet, as measured by AFM, is plotted as a histogram in Fig. 4.5(b). The thickness distribution was extremely broad, with layer numbers ranging from 1 to 98 observed and an average layer

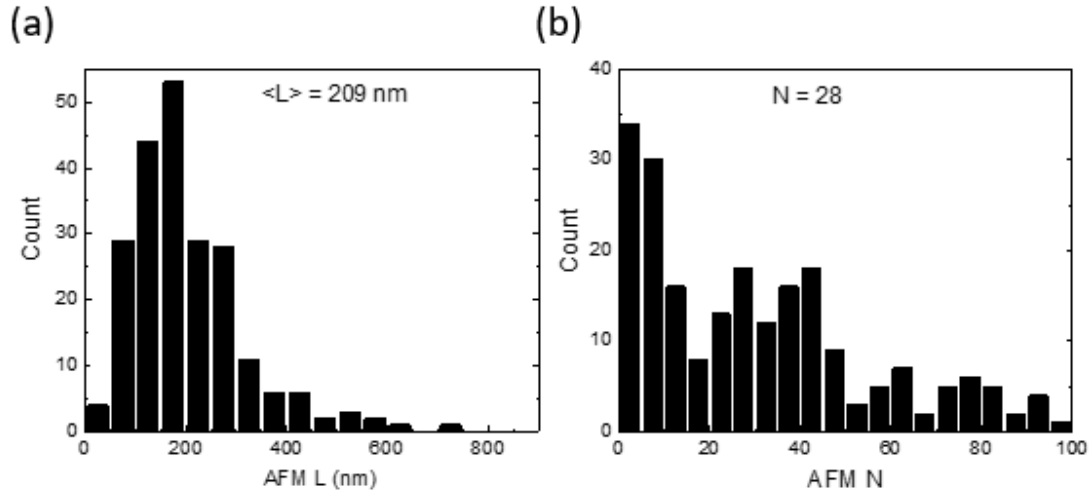

Figure 4.5: (a) Flake size distribution of nanosheets in the dispersion from AFM analysis. (b) Number of layers present.

number of <N> = 30. Assuming the monolayer thickness to be ~0.35 nm,[177] this AFM data yields a length/thickness aspect ratio of ~20. As reported in the group recently, such a low aspect ratio suggests the ratio of nanosheet tearing energy (E_E) to exfoliation energy (E_S) to be relatively small.[181] In fact the aspect ratio should be very roughly equal to twice this ratio,[181] allowing the estimation: E_E/E_S~10, a value which is roughly in the middle of the range for 2D materials.[181]

Optical characterization of the standard sample dispersion was performed using UV-vis spectroscopy. For colloidal dispersions in liquid the extinction spectrum often does not give an accurate representation of the true absorption, as the dispersed nanoparticles can display strong scattering effects.[182] Therefore, it is necessary to use an integrating sphere to remove the scattering component and isolate the absorption spectrum.[154] This can be seen in Fig. 4.6(a) where the extinction, absorption and scattering spectra have been

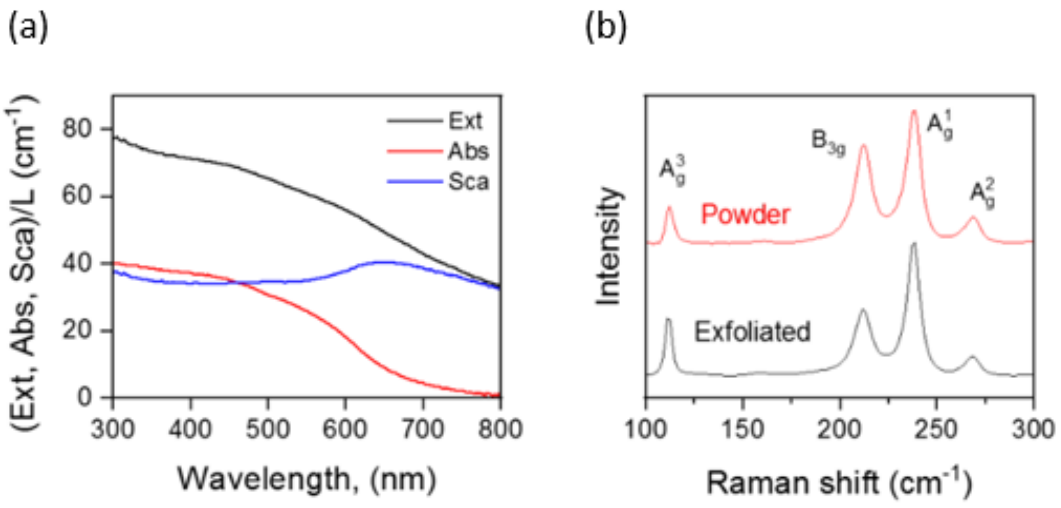

Figure 4.6: (a) Extinction, absorption and scattering spectra for GeS, normalized to path length. (b) Raman spectra for bulk powder (red) and film prepared from exfoliated nanosheets (black).

plotted for the standard sample of GeS. While the extinction does not fall to zero at high wavelength, it is clear from this graph that this is due to a large light scattering contribution. Once this is subtracted from the extinction, the true absorbance spectrum is obtained. This shows a clear band-edge around 700-800 nanometres consistent with the semiconducting nature of GeS.[33]

Raman spectroscopy was also performed on a thin film of nanosheets, which had been prepared by vacuum filtration, as well as the starting powder for comparison (Fig. 4.6(b)). The nanosheet spectrum was noted to be very similar to that of the powder, indicating that the basal planes of the nanosheets have not been significantly damaged during exfoliation. In both cases the Raman modes are in agreement with previous reports on GeS[37]. The assignments are included in Fig. 4.6(b).

4.3 Stability of GeS nanosheet dispersions:

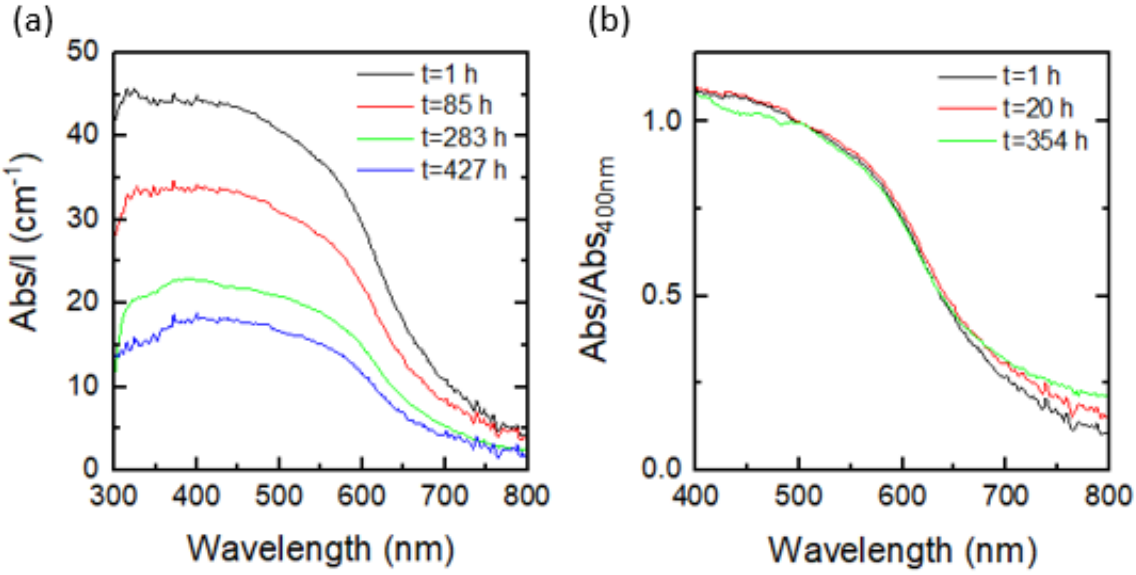

Figure 4.7: (a) Absorption spectra normalized to path length measured periodically. (b) Absorption normalized to the value at 400 nm at three points over the measurement period.

The apparent lack of stability of GeS[29, 30, 183] is arguably one of the contributing factors for the reduced amount of research carried out with this material, and the chief source of concern over its viability as a material for Li ion batteries. Thus, in an attempt to assess the rate of degradation of the GeS dispersion over time when stored in ambient conditions, the absorption spectrum of the standard sample was recorded periodically, in the same manner as for MoO_2. These measurements were carried out over approximately

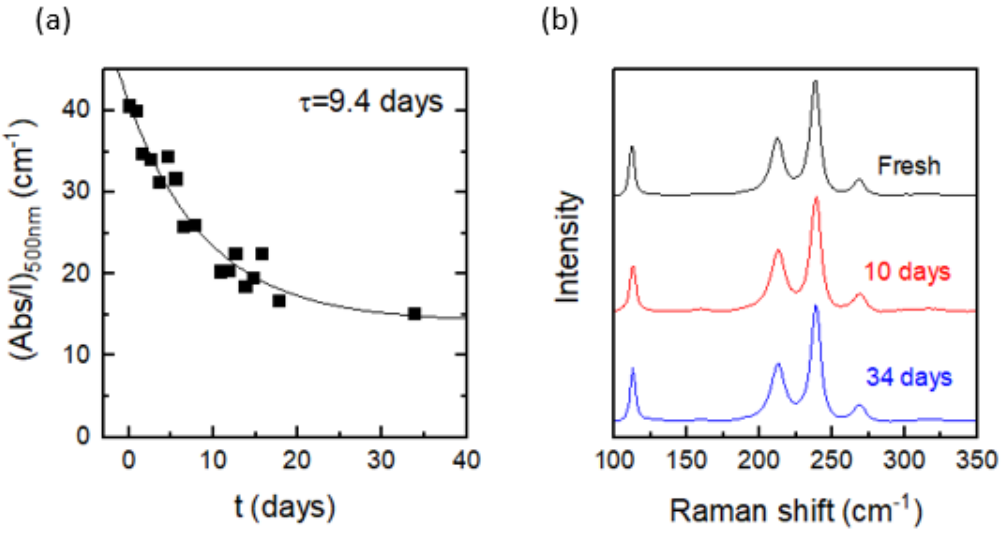

Figure 4.8: (a) Absorption at 500 nm normalized to path length. R-square = 0.95. See appendix for fitting data. (b) Raman spectra of GeS nanosheets, both for a freshly prepared sample and the same sample after storage in ambient conditions.

one month and show that the intensity decreases with increasing time (Fig. 4.7(a)). The measured aliquot was at room temperature for the entire duration and was shaken gently prior to each measurement to ensure any observed changes were not caused by sedimentation of the material.

There is no significant spectral shape change over the measurement period (Fig. 4.7(b)), indicating no major structural changes as was previously observed for MoO_2. However, the absorption intensity is observed to decay exponentially with time (time constant 9.4 days), indicating a reduction in dispersed mass (Fig. 4.8(a)). In addition to the UV-vis characterization, Raman analysis of the same sample was carried out periodically after exfoliation. Raman spectra remained unchanged over at least 34 days (Fig. 4.8(b)).

The exponential decay shown in Fig. 4.8(a) is consistent with ~35 % of the sample remaining after an extended period, indicating that a significant portion of the GeS does not oxidize. In order to compare, similar measurements were performed on GeS exfoliated in exactly the same manner except using an aqueous surfactant (sodim cholate, 2 g/L) solution instead of NMP. It was found that there was a considerably more rapid and complete loss in mass (red data, Fig. 4.9), illustrating the benefits of using NMP.

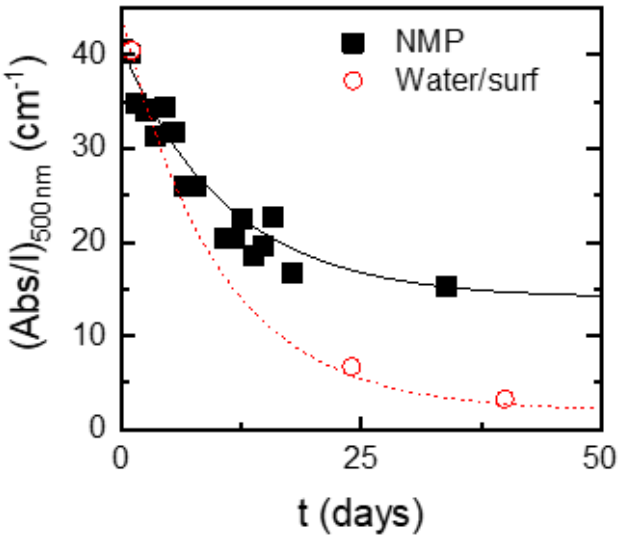

Figure 4.9: Comparison of stability in NMP (black) vs Surfactant solution (red). Absorption at 500 nm measured regularly over an extended period.

The nanosheets were also imaged using TEM at multiple intervals to provide alternative means to track the degradation of the sample (Fig. 4.10). The average length of nanosheets present in the dispersion was observed to decrease over time from 240 nm to ~180 nm. Taken together, these facts are consistent with reactions occurring at the flake edge, making nanosheets smaller and reducing the dispersed mass. This accounts for the diminishing intensity of the absorption and the reduction in average length. The interior of the flakes remains intact, so the Raman spectra and the shape of the absorption spectra do not change.

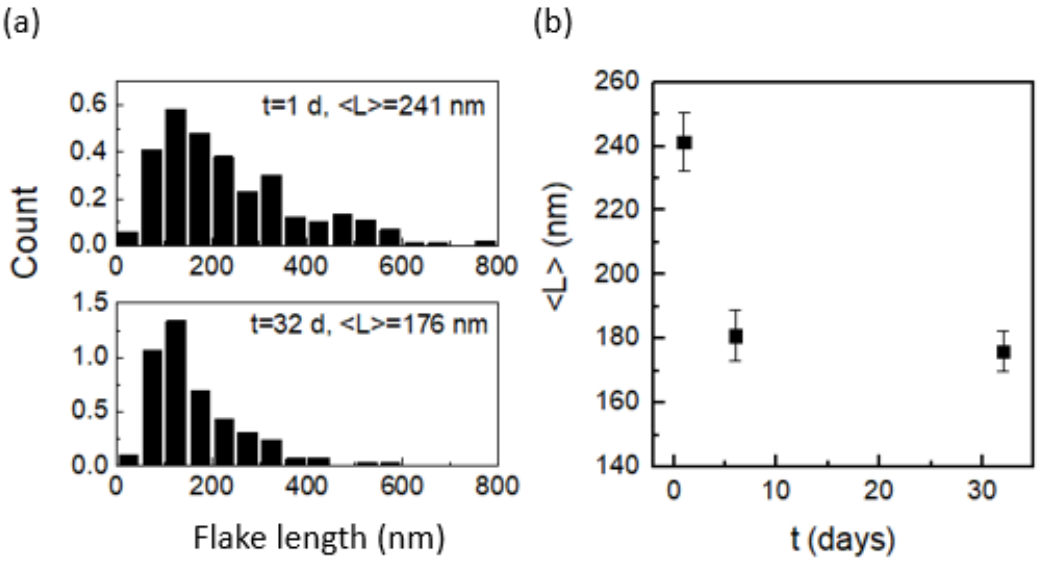

Figure 4.10: (a) Flake size distribution for freshly prepared GeS standard sample dispersion and the distribution for the same sample measured 32 days later. (b) Average nanosheet length from analysis of TEM images for the sample measured 3 times over approximately 1 month.

4.4 Size Selection:

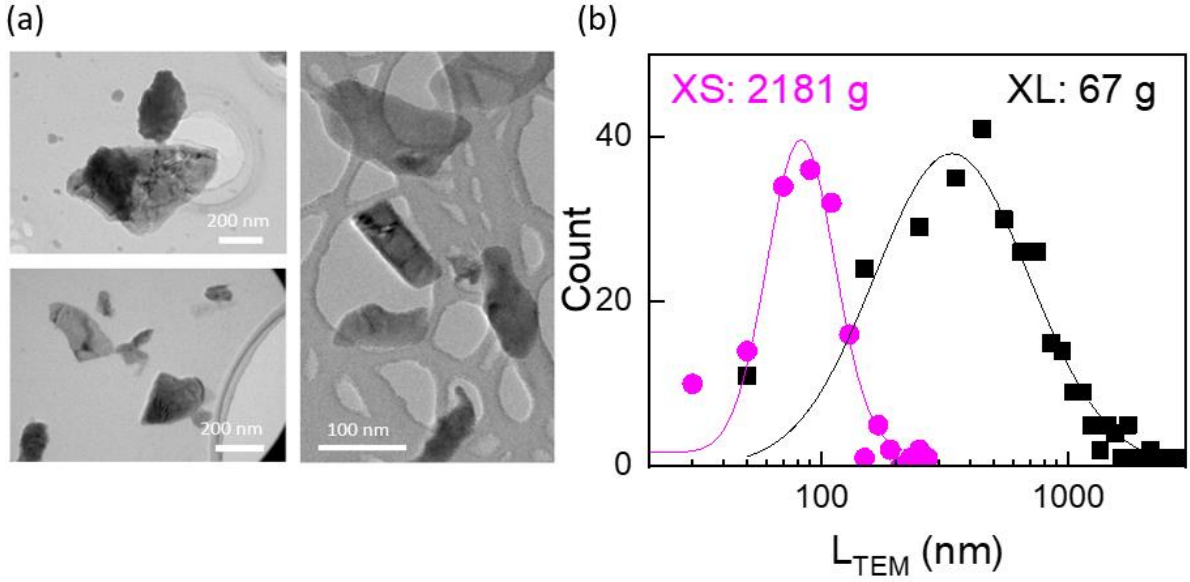

Figure 4.11: (a) Representative TEM images for the XL and L size fractions. (b) Flake size distributions for the 5 krpm (XS) and 1 krpm (XL) samples.

As mentioned previously, one advantage of LPE is the ability to loosely control the size of nanosheets produced. This ability to tailor the size of flakes is invaluable in that applications may require nanosheets of varying sizes. For example, large nanosheets are ideal for mechanical reinforcement[157], and smaller flakes are more suitable for an application that is dependent on surface area, such as catalysis[184]. The size selection process involves subjecting the dispersion to a series of controlled centrifugations, a process termed liquid cascade centrifugation[94] (discussed in Chapter 1). Using this

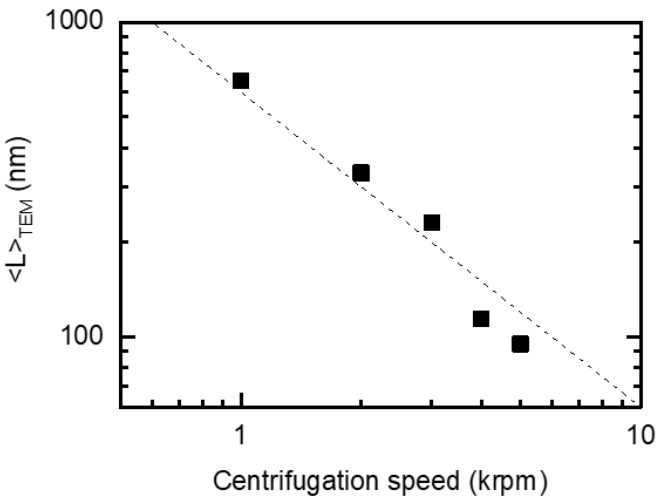

Figure 4.12: Log-log plot of mean nanosheet length from TEM vs centrifugation speed.

method, each size selected fraction is prepared by centrifuging twice, at low speed to remove large flakes and at high speed to remove small flakes. Each fraction can be labelled by the combination of the applied centrifugation rates (expressed as relative centrifugal force, RCF, units of g), or more simply by their average which we denote the central RCF. For clarity we also label the fractions XL, L, M, S, XS (1k, 2k, 3k, 4k and 5k rpm) depending on size (from largest to smallest). In this particular case, the central RCFs were 67 g (XL), 266 g (L), 692 g (M), 1330 g (S) and 2181 g (XS). In order to confirm that the cascade was successful in creating distinct size fractions, an aliquot from each was dropped on holey carbon grids and imaged using TEM. A representative sample of images from fractions XL and L are shown in Fig. 4.11(a).

The recorded flake length distributions for the XL and XS fractions are shown in Fig. 4.11(b). Both exhibit log-normal distributions with the mean length, $\langle L \rangle_{TEM}$, decreasing with increased centrifugation speed as $(RCF)^{-1/2}$ as expected.[21] (Fig. 4.12)

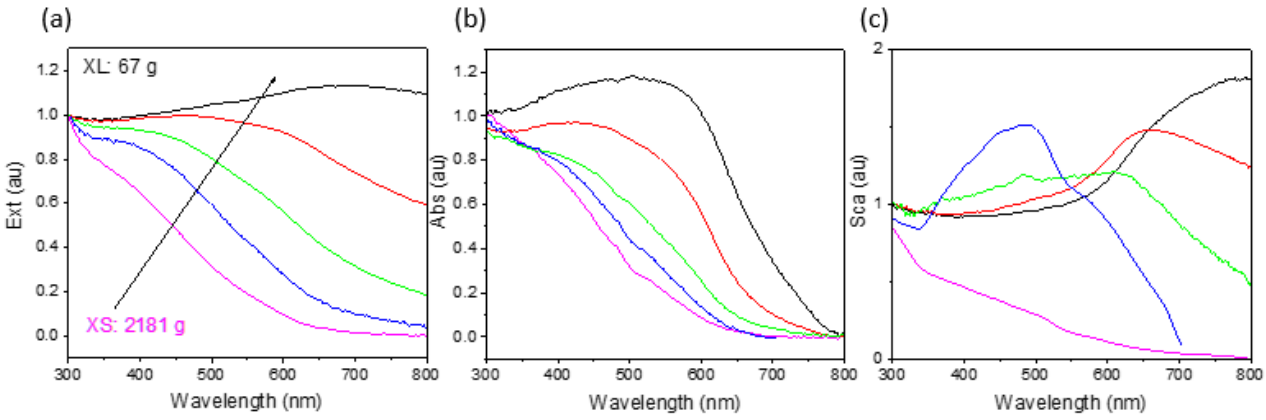

Figure 4.13: (a) Extinction, (b) absorption and (c) scattering spectra for size-selected samples, normalized to 300 nm.

Spectra for the size selected samples were obtained using UV spectroscopy. (Fig. 4.13)

Fig. 4.13(a) shows the normalized extinction spectrum for the size selected GeS dispersion. It can be seen that the spectral shape changes drastically with nanosheet length. The origins for this will be discussed in more detail below. We can quantify this shape change via the ratio of extinction at two wavelengths, chosen arbitrarily at 550 and 300 nm. This ratio (Ext_{550nm}/Ext_{300nm}) is plotted against $\langle L \rangle_{TEM}$ in Fig. 4.14 and shows significant variation. By fitting an empirical function to the data (black line), we can extract a quantitative relationship between Ext_{550nm}/Ext_{300nm} and $\langle L \rangle_{TEM}$, allowing the nanosheet length to be estimated from extinction spectra in future:

$$\langle L \rangle_{TEM} = 150 \times \ln\left[\frac{1.6}{1.1 - Ext_{550nm} / Ext_{300nm}}\right] \qquad 4.1$$

which returns a value of <L>$_{TEM}$ in nm. This Equation would be expected to hold for nanosheet ensembles with mean lengths between ~100 and ~700 nm.

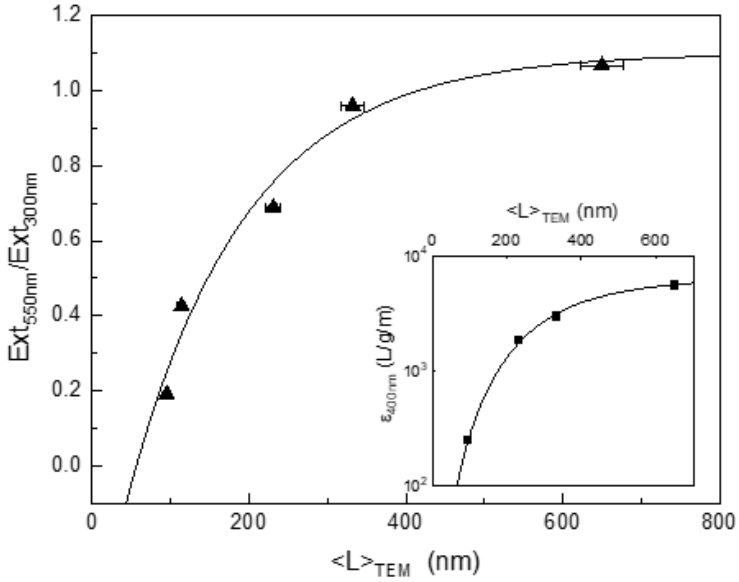

Figure 4.14: Ratio of Ext at 550 nm to Ext at 300 nm vs average nanosheet length from TEM analysis. R-square = 0.97. See appendix for fitting data. Inset: extinction coefficient at 400 nm vs average nanosheets length.

Not only do the shapes of the extinction spectra change with nanosheet size but their absolute values do as well. This means the extinction coefficient (at any wavelength) is nanosheet length dependent. To measure this, the concentration of different size-selected fractions were carefully measured by drying and weighing, and using this data the extinction spectra can be converted to extinction coefficient spectra. Shown in Fig. 4.14 (inset) is the extinction coefficient at 400 nm, plotted against <L>$_{TEM}$. Again, significant variation is noted, which can be quantified by fitting to an empirical function leading to

$$\varepsilon_{400nm} = \left[14.6 \times 10^{-5} + 350 / \langle L \rangle_{TEM}^{2.5}\right]^{-1} \qquad 4.2$$

Inserting <L>$_{TEM}$ in nanometres then yields ε_{400nm} in $Lg^{-1}m^{-1}$. Taken together, these two Equations allow both length and concentration to be obtained from an extinction spectrum of GeS. The length can be obtained easily using equation 1 with the result inserted into equation 2 to give ε_{400nm}. This value can then be combined with the measured extinction at 400 nm to give the concentration, C, using the Lambert-Beer law:

$$C = Ext_{400nm} / (\varepsilon_{400nm} l) \qquad 4.3$$

where l is the cell length.

As mentioned previously, extinction spectra are often quite different to absorption spectra because the nanosheets present in dispersion exert strong scattering effects. It was necessary therefore to use a UV-vs spectrometer equipped with an integrating sphere to separate the extinction into its absorption and scattering components. The resultant scattering spectra, normalized to their values at 300 nm, are plotted in Fig. 4.13(c) for five different size selected fractions. These scattering curves show very large variations with nanosheet size as might be expected from previous reports.[182] It is noted that scattering spectra are expected to be particularly sensitive to nanosheet length.[182] In most cases, these scattering spectra contain a peak at intermediate wavelength followed by a fall-off in scattering intensity at high wavelength. The position of the peak tends to redshift as nanosheet size increases. In previous investigations of MoS_2 dispersions, this peak was observed to occur near the band-edge.[154] The observed shift implies the optical bandgap of GeS nanosheets to shift with nanosheet dimensions. This can be seen more clearly by plotting the actual absorbance (found by subtracting scattering from extinction) spectra in Fig. 4.13(b). This plot clearly shows significant changes in spectral shape with nanosheet size. Most obviously, the band-edge appears to shift to lower wavelength as nanosheet size decreases, consistent with the scattering data. From these plots, the optical

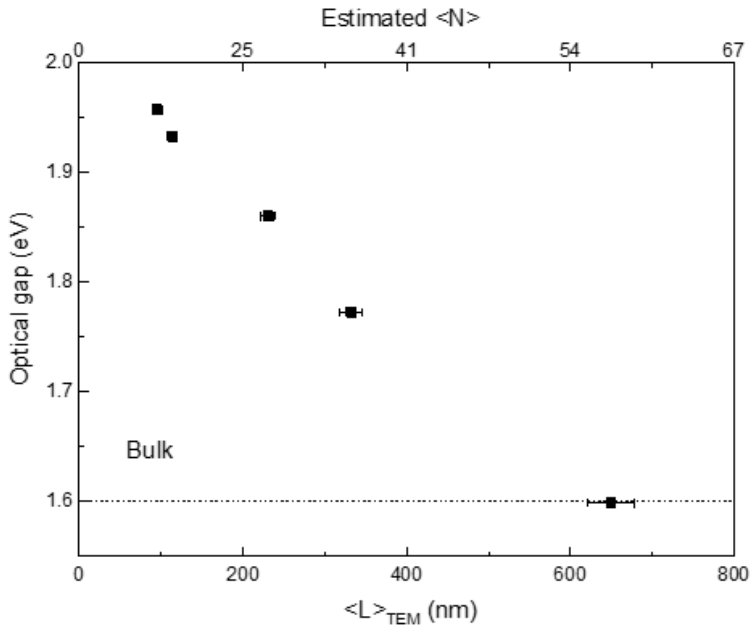

Figure 4.15: Optical gap plotted against Average nanosheet length from TEM fir different size fractions.

gap is estimated (a measure of the first excitonic transition) for each nanosheet size. This is plotted in Fig. 4.15 against $\langle L \rangle_{TEM}$ showing a well-defined trend with optical gap falling from ~1.95 eV for the smallest nanosheets to ~1.6 eV for the largest ones.

While Fig. 4.15 implies the optical gap to scale with nanosheet length, this is probably not the case. It has recently been shown that, for liquid exfoliated nanosheets, the nanosheet length and thickness are closely correlated and scale with each other.[181, 185] It is more likely that the optical gap is related to the nanosheet thickness and is controlled by effects such as quantum confinement[186, 187]. Using the fact that $\langle L \rangle \propto \langle N \rangle^b$, where b~1.4 for a range of 2D materials,[181] combined with the measured values of $\langle L \rangle_{TEM}$ and <N> for the standard sample of GeS, allows the estimation of the values of <N> corresponding to $\langle L \rangle_{TEM}$ as shown on the top axis of Fig. 4.15. This shows that the size-selected fractions have mean nanosheet thicknesses between ~15 and 60 layers corresponding to actual nanosheet thicknesses in the range of ~5-20 nm. It is extremely interesting that thickness dependent effects are seen in the thickness range. This data implies the optical gap to reach its bulklike value of ~1.6 eV [188] at <N>~60, which is considerably thicker than for other materials previously studied. For comparison, the optical gap of TMDs tends to reach bulk values for <N>~10-15 layers.[187] However, it is noted that these results are not without precedent as the wavelength associated with peak luminescence of GeS nanowires has been observed to scale with the diameter (analogous to nanosheet thickness) for diameters beyond 100 nm.[183] The data in Fig. 4.15 implies a shift in optical gap from monolayer to bulk of >350 meV. This is much larger than shifts of 50 to 70 meV found for TMDs,[187] and as far as I know is the largest thickness-dependent shift for any 2D material.

4.5 Applications of Liquid-exfoliated GeS Nanosheets in Battery Electrodes:

While GeS has potential for use in a number of applications,[189, 190] the area possibly most suited to liquid exfoliated nanosheets would be use as an anode material in lithium ion batteries. Based on elemental lithium storage capabilities (1620 mAh/g for Ge[177] and 1675 mAh/g for S[191]), GeS has a theoretical specific capacity of 1635 mAh/g, considerably higher than the value of 370 mAh/g associated with graphite. Indeed GeS nanoparticle based electrodes have achieved close to 1800 mAh/g,[192] albeit with poor cycling stability and 1100 mAh/g with very good stability.[177] Thus, one challenge appears to be to achieve near-theoretical capacity coupled with good cycling stability.

This problem has been encountered a number of times with lithium-storing layered materials. For example, while poor cycling stability is common in lithium ion battery electrodes incorporating bulk MoS_2, this problem could largely be solved by exfoliating the MoS_2 to give nanosheets rather than particles of bulk layered crystal.[193] Indeed, anodes fabricated from liquid exfoliated GeS nanosheets have demonstrated 1000 mAh/g with reasonable cycling stability.[37] In addition, it has been shown that adding carbon nanotubes to the electrode can allow electrodes based on both 2D[86, 149] and particulate materials[194] to approach their theoretical capacity due to the high conductivity and mechanical robustness imparted by the nanotube network.[169, 174, 194] Thus , it is proposed that stable electrodes based on GeS could be achieved using mixtures of carbon nanotubes and liquid exfoliated nanosheets prepared in ambient conditions.

To test this, lithium ion battery anodes were produced via solution mixing of liquid-exfoliated GeS nanosheets (i.e. the standard sample described above) with 20 wt.% single wall nanotubes added with the latter material acting as both conductive additive and

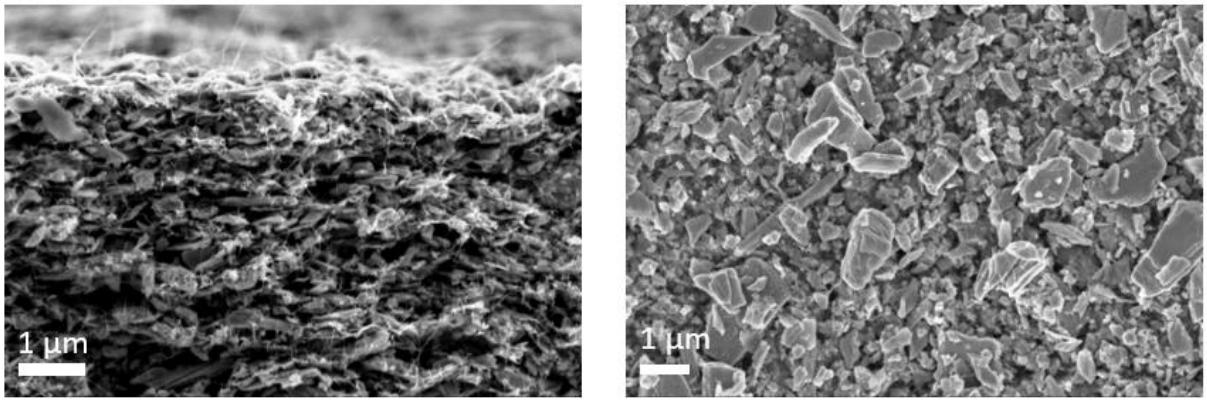

Figure 4.16: SEM images of fiom containing exfoliated GeS nanosheets with 20 wt % CNTs.

mechanical binder.[86, 180] All battery measurements and analysis were carried out by Dr Ruiyuan Tian.

These dispersions were fabricated into films by vacuum filtration and transferred onto copper current collectors. SEM images of the surface of such a composite electrode are shown in Fig. 4.16. In addition, the in-plane conductivity of the film was measured to be

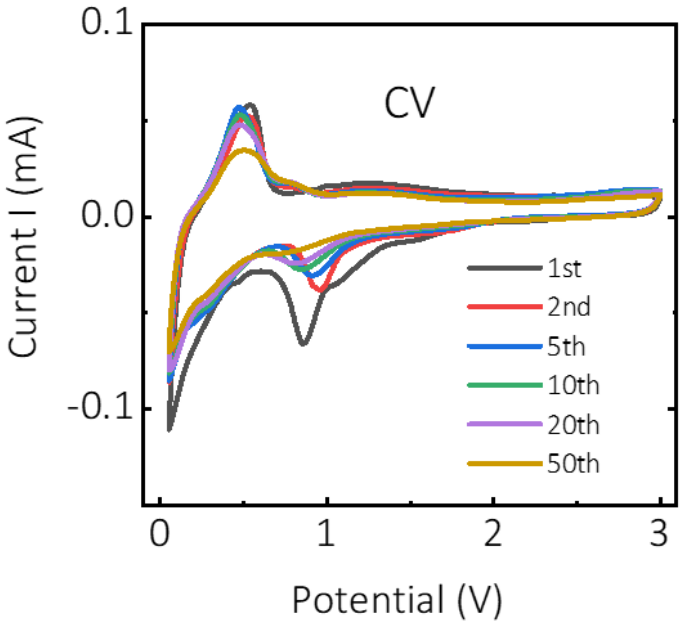

Figure 4.17: Current-voltage curves for Li ion batteries using the GeS-CNT film.

~890 S/m.

To study the electrochemical lithium storage mechanism, cyclic voltammetry (CV) data was measured at a scanning rate of 0.1 mVs^{-1} and shown in Fig. 4.17.

There were two pairs of redox peaks over a voltage range of 0.05-3.0 V. The reduction peak at 1.0 V is related to the conversion reaction to form Li_2S:[192]

$$2Li^+ + 2e^- + GeS \rightleftarrows Ge + Li_2S$$

while the reduction peak at ~0.15 V can be assigned to the further alloying reaction forming $Li_{4.4}Ge$:[192]

$$4.4Li^+ + 4.4e^- + Ge \rightleftarrows Li_{4.4}Ge$$

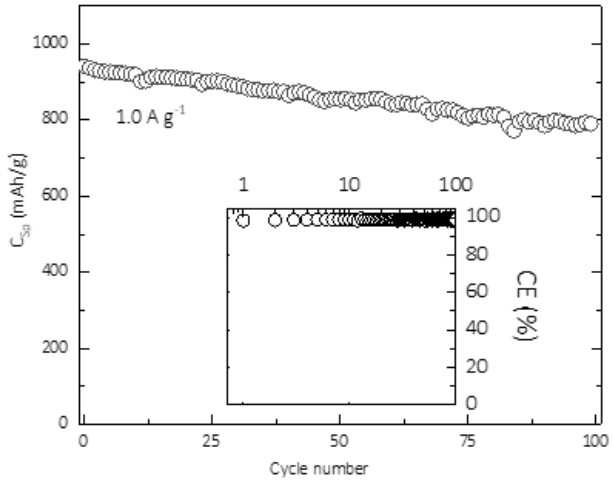

Figure 4.18: Charge capacity vs cycle number for GeS-CNT batteries. Inset: Coulombic efficiency during cycling.

As mentioned above, these reactions have an associated theoretical capacity of 1635 mAh/g. The oxidation peaks at 0.5 V and 1.2 V can be assigned to the delithiation from $Li_{4.4}Ge$ and Li_2S, respectively.[192] It is noted that the reduction peak at about 1.0 V gradually shifts to a lower potential and fades away during 50 cycles, suggesting a slight degradation of the conversion reaction.

Basic electrochemical characterisation with galvanostatic charge capacity versus cycle number was performed, measured at 1 A/g and the data is shown in Fig. 4.18. Under these circumstances, the GeS/CNT electrodes showed good lithium storage capability with an initial charge capacity of 942 mAh/g, with a Coulombic efficiency (CE) of 98.4%. (Fig. 4.18 inset) The capacity was reasonably stable, falling to 791 mAh/g (with 98.9% CE) over 100 cycles. This stability is significantly better than that observed by Wei et al.[192] but doesn't quite match that of Cho et al.[177]

The rate performance of the electrodes was also tested with voltage profiles and rate dependent cycling data in Fig. 4.19 These electrodes exhibited an initial performance of

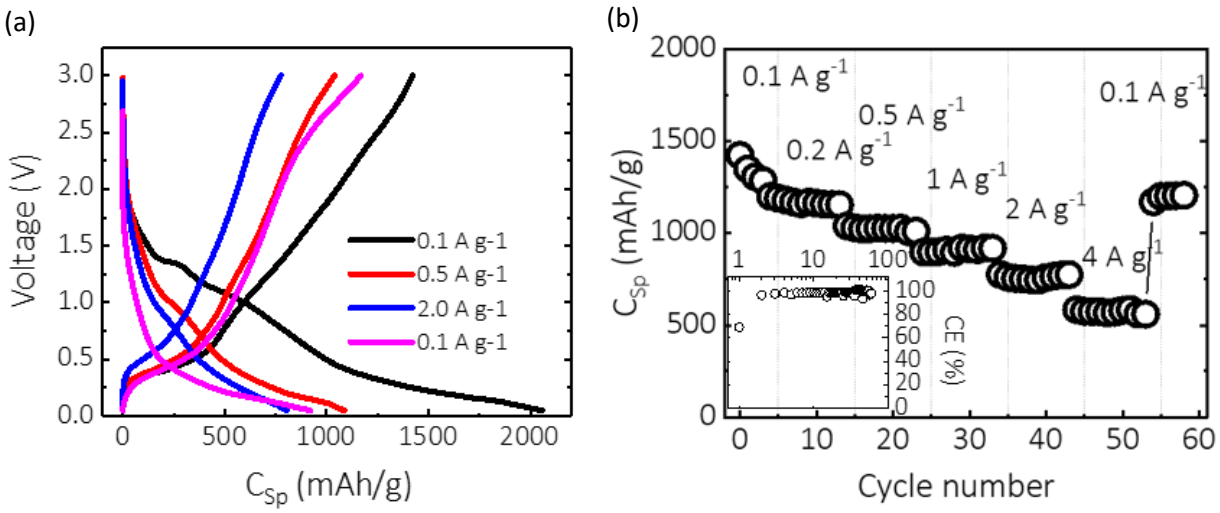

Figure 4.19: (a) Voltage profiles for various values for specific current. (b) Rate dependence of specific capacity against cycle number. Inset: Coulombic efficicency.

2059 mAh/g for discharge and 1423 mAh/g for first cycle charge at 0.1 A/g with Coulomb efficiency approaching 99 % for subsequent cycles. For higher specific currents of 0.5, 1.0, 2.0 and 4.0 A/g, the specific charge capacities fell off to 1039, 897, 776 and 584 mAh/g respectively. On returning the current back to 0.1 A/g, the specific charge capacities reached 1200 mAh/g, showing reasonably good stability. This rate performance is quite similar to that recently reported by Lam et al., also for GeS nanosheets.[37]

Lam et al. pointed out that the rate performance found for GeS, assessed via the combination of achieved specific capacitance and applied current density, compares very well with electrodes based on other 2D materials. This is not an unreasonable assessment given the high diffusion coefficient of Li ions within GeS.[195]

4.6 Conclusions:

To conclude, it was demonstrated that layered GeS can be exfoliated via LPE in ambient conditions to give near-pristine nanosheets. Although oxidation does occur over a period of days, it appears to be limited to the edges of the nanosheets, leaving the basal plane intact. The relatively slow rate of the oxidation process means that the nanosheets can be processed before significant oxidation occurs. For example, it was possible to size-select the nanosheets and measure the dependence of flake size on the optical properties of the dispersions. Additionally, the dispersions were processed into thin films for use as lithium ion battery anode material. Adding carbon nanotubes to enhance the electrical and mechanical properties of the film allowed these anodes to show lithium storing capability of 1523 mAh/g (93% of theoretical value) and relatively good stability. However, the analysis found poor intrinsic rate performance suggesting that this may be due to problems general to 2D materials such as nanosheet alignment.

4.7 Experimental Methods:

Dispersion Preparation:

Germanium sulfide powder was ordered from Sigma Aldrich (5 g, 99 %), and used as received. When not in use the powder was stored in an argon atmosphere in a glovebox. GeS was sonicated numerous times times using different solvents in order to choose the optimal candidate for exfoliating the material. 100 mg GeS was added to a glass vial containing 20 mL solvent and was sonicated for 1 hour using a tapered tip at 25 % amplitude, with an on/off pulse ratio of 6s/2s. After sonication the dispersions were centrifuged for 2.5 hours at 2500 rpm (665 g). UV vis spectroscopy analysis of each dispersion allows the concentration to be measured and plotted as a a function of the Hildebrand solubility parameter. Only the candidates with the highest dispersion concentration were considered, and NMP was ultimately chosen as the best option. All dispersions for further testing were made using NMP as solvent.

Solvents used in this study: Cyclohexyl-pyrrolidone (δ = 20.49 $MPa^{1/2}$), dimethyl formamide (δ = 24.86 $MPa^{1/2}$), isopropanol (δ = 23.58 $MPa^{1/2}$), deionized water (δ = 47.81 $MPa^{1/2}$), methanol (δ = 29.41 $MPa^{1/2}$), pentane (δ = 14.5 $MPa^{1/2}$), 1-methyl-2-pyrrolidone (δ = 22.96 $MPa^{1/2}$), chloroform (δ = 18.95 $MPa^{1/2}$).

GeS (400 mg) was added to NMP (80 mL) in a cooled aluminium vessel and sonicated using a horn-tip sonic probe (Vibracell CVX, 750 W) at 60 % amplitude for 6 hours with an on/off pulse ratio of 6s/2s. After sonication, the resulting dispersion was centrifuged (using a Hettich Mikro 220r with a fixed angle rotor), for one hour at 500 rpm (26.6 g) to remove unexfoliated material. The sediment was discarded, and the supernatant centrifuged at 5000 rpm (2660 g) for one hour to separate the extremely small nanosheets. The sediment from this second centrifugation step was redispersed in fresh NMP. The GeS dispersion produced in this manner is referred to as the standard sample and contains a range of flake sizes.

Size Selection:

It is possible to exert a level of control on the size of nanosheets by subjecting a dispersion to a process called liquid cascade centrifugation. After sonication, the GeS dispersion was centrifuged at 500 rpm. The sediment consisted of large unexfoliated material and was discarded, while the supernatant was centrifuged at 1000 rpm. After this step, the supernatant was decanted and subjected to further centrifugation. The sediment represents the material from the 500-1000 rpm fraction and can be redispersed to any

desired concentration. Repeating this process with incremental increases in the centrifugation speed allowed the initial dispersion with a range of sizes present to be segregated into distinct size fractions. The average length of nanosheets in any given fraction can be ascertained from TEM analysis. In this manner, through a combination of exfoliation and selective centrifugation, samples of GeS nanosheets can be produced to the length range desired.

Characterization:

The nanosheets were imaged using a JEOL 2100 series Transmission Electron Microscope (TEM). Dispersions of GeS were prepared by drop casting on holey carbon TEM grids (Agar Scientific) placed on filter paper to absorb any excess solvent. After imaging, the lengths of nanosheets were ascertained using ImageJ software and histograms of the flake size distribution were compiled. The longest dimension observed for any given nanosheet was designated as the flake length.

Optical characterization was performed in a quartz cuvette (path length 4 mm), using a Perkin Elmer Lambda 1050 series ultraviolet-visible spectrometer, equipped with an integrating sphere for isolating the absorption spectrum (extinction with scattering effects removed).

A Veeco Nanoscope-IIIa system (Digital Instruments) was used in tapping mode for AFM measurements. Samples were prepared by drop casting 15 μL of diluted dispersion (O.D. approx. 0.4) onto a preheated, cleaned Si/SiO 2 (285 mn oxide layer) at 180 ° C. Individual nanosheets were then analysed using previously established length corrections for pixilation effects and tip broadening. Step height analysis as reported for previous materials was used to convert the apparent thickness of nanosheets to the number of layers. AFM imaging and analysis was performed by Aideen Griffin.

Raman spectra were acquired by Dr Victor Vega-Mayoral using a Horiba Jobin Yvon LabRam HR800. A green laser (532 nm) was chosen as excitation laser line. Signal was collected using a 100x objective (0.8 N.A.). 600 grooves per mm grating has been chosen in order to obtain ~1 cm^{-1} spectral resolution. Measurements were done in air at room temperature. Beam size on sample is approximately 2 μm diameter and the laser power was kept below 0.2 mW. No degradation or heating effects were observed at the chosen fluence. Each plotted spectra is the result of acquiring signal for 60 seconds and the average of 15 spectra is displayed.

Electrochemical Characterization:

All battery measurements and analysis were carried out by Dr Ruiyuan Tian.

The GeS dispersions were mixed with SWCNTs (20 wt %), which both increases conductivity and functions as a binder. The SWCNTs were prepared by adding 10 mg P3-SWCNT to 100 mL IPA and sonicating for one hour in a Fisherbrand Sonic Dismembrator (30 W, 40 % amplitude). The combined dispersion was vacuum-filtered using a porous cellulose membrane (MF-Millipore membrane, mixed cellulose esters, hydrophilic, 0.0025 µm pore size, 47 mm diameter) to give thin films. The films produced were cut to the desired dimensions for electrochemical testing and then transferred to copper foil using IPA to adhere the film to the substrate. The cellulose membrane was removed by treatment with acetone vapour and subsequent immersion in multiple acetone baths. The mass loading of GeS is 0.5 mg cm^{-2}, with 20 wt.% SWCNTs (0.125 mg cm^{-2}). For the electrochemical measurement, metallic lithium foils (diameter: 14 mm, MTI Corp.) were used as the negative electrodes. The electrolyte used was 1.2 M $LiPF_6$ in a 1:1 (volume ratio) mixture of ethylene carbonate (EC) and dimethyl carbonate (DMC) with 10wt% fluoroethylene Carbonate (FEC). A Celgard 2320 was used as the separator. The cells were assembled in a glovebox filled with highly pure argon gas (O_2 and H_2O levels < 0.3 ppm), and the electrochemical properties of the electrodes were measured within a voltage range of 3.0−0.05 V using constant current (CC) mode on an automatic battery tester (VMP 3, Biologic). For rate capability measurement, cells were running at different current rates of 0.1 A g^{-1}, 0.2 A g^{-1}, 0.5 A g^{-1}, 1 A g^{-1}, 2 A g^{-1}, 4 A g^{-1}, and then went back to 0.1 A g^{-1}. There are only 4 cycles at 0.1 A g^{-1}, then there are 10 cycles for the next steps at different current rates. For cycling capability tests, the cells were performed at 1 A g^{-1}. For cycling capability tests, the cells were performed at 1.0 A g^{-1} for 100 cycles. Cyclic voltammetry of the cells was carried out using a galvanostat–potentiostat between 0.05 and 3.0 V at a scanning rate of 0.1 mV s^{-1} for 50 cycles. Unless otherwise stated all capacity values are normalized to the active (GeS) mass.

5

Light-Emitting Electrochemical Cells

5.1 Light-emitting Electrochemical Cells (LECs):

The previous two chapters described the preparation of nanosheet dispersions for incorporation into lithium ion batteries. However, the versatility of LPE is such that dispersions produced in this manner have been used for a variety of different applications. Since the development of this technique in 2008, LPE derived nanosheets have been shown to be effective in a number of different devices such as supercapacitors[21], catalysis[80] and sensors[152] for example.

This chapter details preliminary research on the extension of LPE for the first time to light emission technology, and more specifically, to light emitting electrochemical cells (LECs).

Up until the end of the 20th century, incandescent bulbs made up the majority of artificial lighting. Since then, the development of solid-state lighting has been a huge breakthrough in illumination. In the case of incandescent bulbs, light emission occurs as a secondary effect of heating the filament, a highly inefficient process.[196] Conversely, in the case of light-emitting diodes (LEDs) or more recently, organic light-emitting diodes (OLEDs), light generation via electroluminescence (EL) is the main product. As a result, these devices have potentially longer lifetimes with lower energy consumption.[196]

LEDs are composed of compound semiconductor materials and emit light from a p-n junction when current flow through them.[196] Recombination of an electron from the n-type zone and a hole from the p-type results in radiative emission, the wavelength of

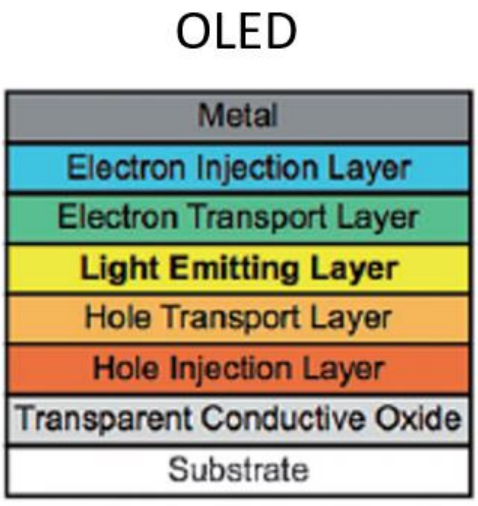

Figure 5.1: Schematic for typical OLED device [194].

which depends on the bandgap of the semiconductor. LEDs are used extensively in electronics, displays and lighting.

An OLED is essentially an LED which uses a layer composed of an organic compound for emission.[197, 198] They are typically complex multi-layer devices, with the active layer stacked between two electrodes and often accompanied by hole/electron injection layers. The anode is usually a transparent conductive oxide such as ITO[197], and the cathode can be a metal such as aluminium. The complicated structure of an OLED is necessary to ensure the carrier injection is balanced, but it hinders scaling up of area processing and increases production costs.[199] Shown in Fig. 5.1 is an example of the structure of a typical OLED device.

Compared to an OLED, LECs have a much simpler design.[196, 197, 199-202] They often consist of just an active layer sandwiched between two electrodes, on the condition that the active layer contains sufficient added ionic species to allow doping and subsequent junction formation in response to an applied voltage.[203] Electrolytes or ionic liquids can be used to provide the necessary ionic species if required. Commonly used active materials in LECs include conjugated polymers and ionic transition metal complexes. One of the regularly cited advantages of LECs is the capacity for solution processing, which makes them potentially ideally suited for fabrication from LPE dispersions. Shown in Fig. 5.2 is the structure for a typical LEC device.

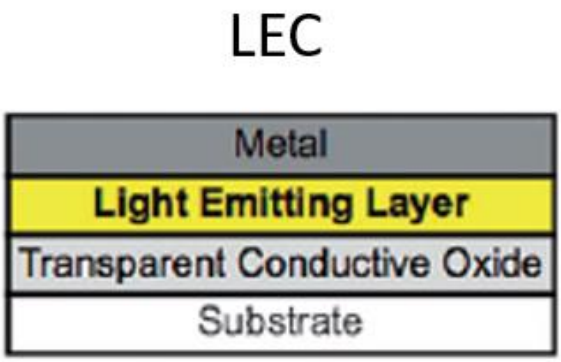

Figure 5.2: Schematic for typical LEC device [194].

5.2 Operation Mechanism:

After the first demonstration of an LEC device in 1995 by Pei et al.[203], two independent mechanisms were proposed to describe how the device functions: the electrodynamic model (ED) and the electrochemical doping model (ECD).[196]

The ED model makes the assumption that accretion of ions at the electrodes occurs in response to an applied voltage, causing electric double layers (EDL) to form at the active layer/electrode interface. This results in a large drop in electric potential near the interface and causes charge injection from the electrodes. These charge carriers recombine in the active layer and light is emitted from the bulk, in what is called the "field free region".

Conversely, the ECD model predicts that the aforementioned accumulation of ions at the electrodes leads to the development of two distinct doped regions, p-type near the anode and n-type near the cathode respectively. Over time these regions widen forming a p-i-n junction, with 'i' referring to the undoped intrinsic zone between the n-type and p-type regions.[203] In this case there is a significant voltage drop across the intrinsic zone, facilitating the recombination of the electrons and holes in this region, and subsequent light emission.

In essence, the main difference between the two is the proposed position of the electric field concentration.[204] The ED model predicts high electric fields closer to the electrodes whereas the ECD model suggests a high electric field in the bulk of the active material.

Both models have been supported in numerous publications[196]. The operational mechanisms of these models are shown in Fig. 5.3 below.

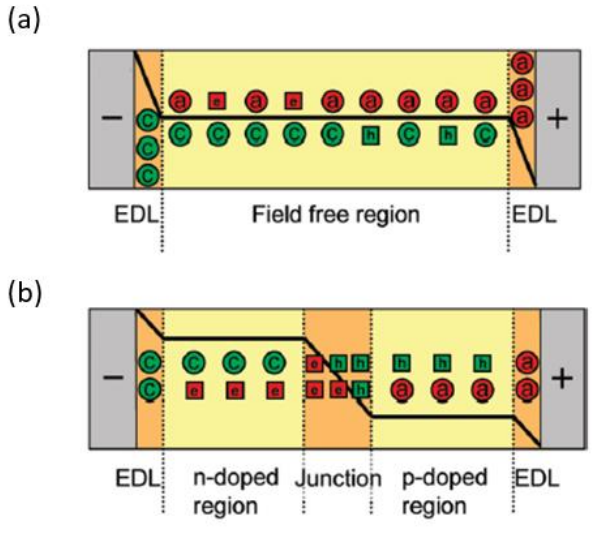

Figure 5.3: Proposed mechanism for LEC operation. (a) ED model, (b) ECD model.

Over time, the community has tentatively concluded that these models are both demonstrated to be descriptions of different circumstances of the same over-arching mechanism governing LEC function.[200, 202, 205]

Application of a voltage across the device instigates a redistribution of the ionic species in the active material.[206] The electric field directs anions and cations to the respective electrodes where they form EDLs. At low bias, only a small amount of charge carriers are injected, and in this case the voltage drops over the EDLs, leaving the majority of the active layer field free. This behaviour is similar to that suggested in the ED model, and results in low emission. A higher voltage forces the injection of more charge carriers which travel through the active material and start to build up doped regions as predicted by the ECD model. These highly conductive doped zones slowly build towards each other, and the potential drops across the intrinsic zone between them. Radiative recombination of electrons and holes in this region results in light emission, whose colour is defined by the bandgap energy of the material.[201] However, the device is self-limiting in that the continuous growth of the doped regions (assuming sufficient ionic material present) results in quenching of the excitons as the intrinsic zone gets narrower, reducing electroluminescence.[200] Fig. 5.4 shows the a depiction of the development of the p-i-n junction in an LEC device.

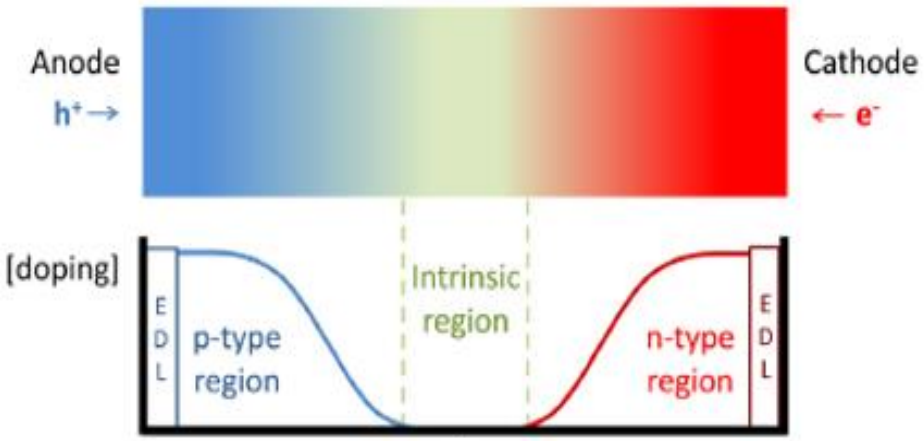

Figure 5.4: Operation mechanism of an LEC device after the formation of the EDLs and doped regions. Adapted from [198].

While generally accepted, this model presents numerous challenges for using LECs. Given that the light emission is reliant on the transport of ionic species, the ion mobility

of the active material is important for the process. As a result, there is an inherent 'turn-on time' (t_{on}) for the device before light emission,[196, 200] which can range from minutes to days depending on the device composition. The t_{on} suggests that LECs may not be well suited to applications in displays or electronics and may be more appropriate for use in artificial lighting instead.[204] There are a number of methods to reduce the t_{on}, the simplest of which is to increase the applied voltage. While this can lead to significantly shorter activation times, the stability of the device may be compromised and the reduction of the intrinsic zone may be accelerated, thus reducing the lifetime. Another alternative is the addition of an ionic liquid to the active layer, to provide an abundance of mobile ions and speed up the development of the EDLs. Although this addition can negatively affect the stability, it has been shown to massively reduce the t_{on} for the device.[196, 200]

As mentioned earlier, LEC devices have the unfortunate trait of being self-limiting.[200] The propagation of the doped regions and subsequent reduction of the intrinsic zone causes quenching of the electroluminescence.[206] Encouragingly, recent work has shown that the growth of the doped regions can be restricted through temperature control or by a pulsed driving current during device operation.

Although the majority of work on LECs involves the use of conjugated polymers or transition metal complexes as active material, there is the potential for using other semiconductor materials that exhibit electroluminescence. Additionally, the necessity for a transparent electrode to allow the generated light to be transmitted has meant that the majority of LECs contain a transparent conductive oxide such as ITO as electrode material.[206] More recently however, graphene has attracted interest in this role, and could potentially be used for both anode and cathode. Research with 2D materials has shown that few-layer or monolayer structures can display a change in bandgap when compared to the bulk material. Exfoliation may therefore increase the number of candidate electroluminescent semiconductor materials for consideration. In this regard the exfoliation of these materials and possibility of incorporation into LEC devices is an exciting concept.

It is important to reiterate at this stage that the work described in this chapter is a preliminary look at the feasibility of using liquid phase exfoliated materials in LEC devices.

5.3 LEC Design:

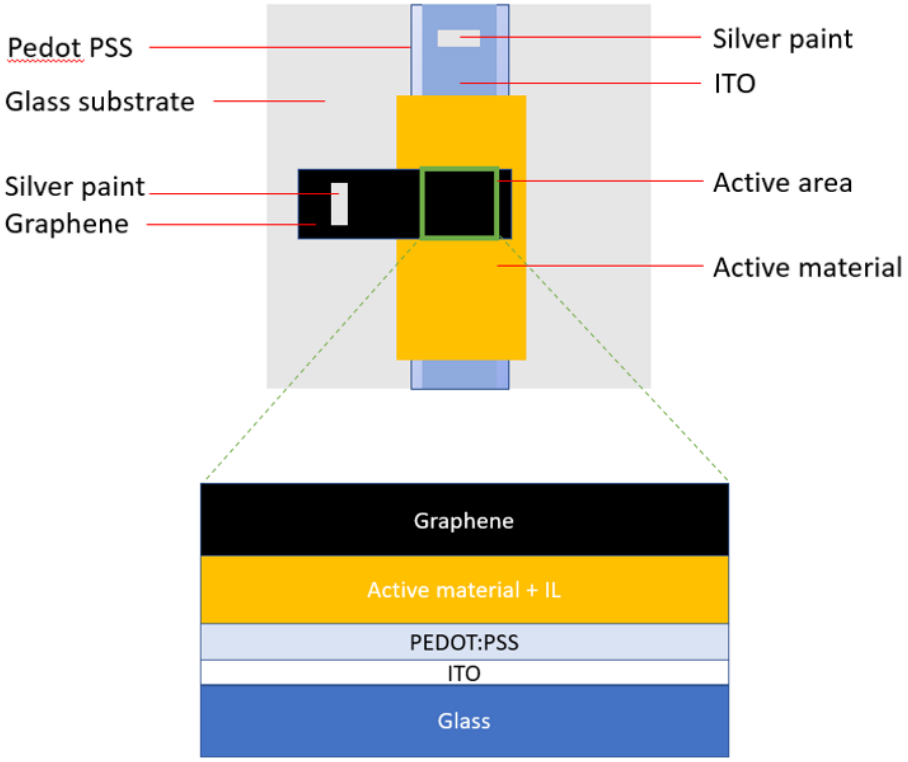

Figure 5.5: Proposed design for sandwiched LEC device, and cross-section of the active area.

Shown in Fig. 5.5 is the design for a LEC device on a glass substrate, which consists of the active material sandwiched between a graphene layer (cathode) and a layer of ITO (anode) coated with PEDOT:PSS (PPSS).

A glass slide coated with ITO was selectively etched to leave a narrow strip 4 mm wide. The PPSS functions as a hole injection layer, and is spin coated onto the slide over the remaining ITO section. The active material is spray coated onto the slide using an airbrush with a suitable mask to pattern the material over the ITO/PPSS. Similarly, the graphene is sprayed on top of the material, forming a strip perpendicular to the direction of the ITO strip. The active area of the device is 4 mm^2. Silver contacts were painted on to the electrodes to facilitate biasing of the device with tungsten probes. The ionic liquid was added to the device immediately prior to testing using a glass Pasteur pipette. The porosity of the sprayed material is advantageous in that the ionic liquid can fully penetrate the internal free volume of the network. As we are in the early stages of this work, only two active materials have thus far been used, cadmium selenide nanoplatelets and zinc oxide.

5.4 Initial LEC tests:

The long-term goal of this work is to fabricate LEC devices composed entirely of LPE-nanosheets derived components, however before this can be realised it is necessary to ensure that the proposed design functions as intended. With this is mind, the first devices prepared consisted of a LPE graphene strip sprayed on an active layer of CdSe nanoplatelets (NPLs). These NPLs have previously been shown to be an effective emissive layer in LEDs. Their emission in the visible spectrum (420-710 nm) can be attributed to strong anisotropic quantum confinement. The CdSe NPLs used in this work were synthesized by collaborators from IST Austria, in the group of Prof. Maria Ibanez, and were dispersed in hexane, a low boiling point solvent which meant they could easily be deposited via spraying. The absorption spectrum of the CdSe sample were provided by our collaborators and is shown in Fig. 5.6 along with TEM images of the NPLs.

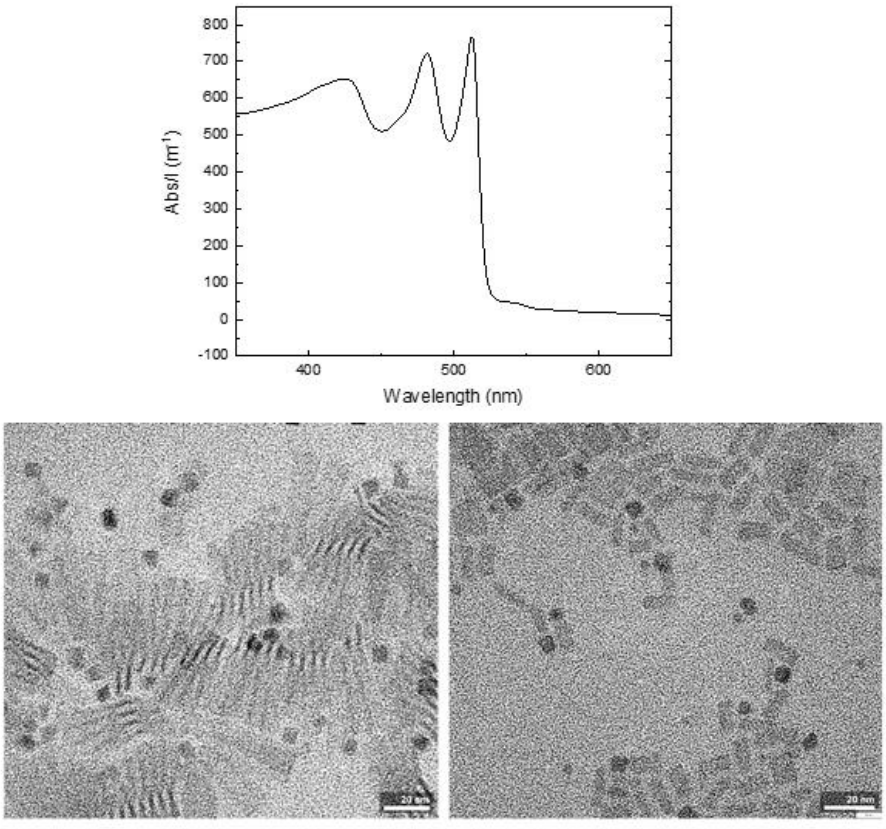

Figure 5.6: Absorption spectrum and TEM images of the CdSe nanoplatelets.

An LEC device was prepared using this material as active layer and was tested using a rather crude improvised set-up. The device was encapsulated in a sealed chamber while in a glove box, to ensure operation in an inert environment. The primary reason for an inert atmosphere was to prevent any water vapour from interacting with the ionic liquid,

as it would reduce the electrochemical window. There was a glass aperture in the top of this chamber to allow any emitted light to escape. The chamber was then placed inside a PL apparatus in order to use the detector therein to record any emission.

A constant voltage of 3 V was applied across the device and numerous spectra of the emitted light were captured over the next 32 hours. After a turn-on time of approx. 1.6 hours a weak electroluminescent signal was detected around the 560 nm mark.

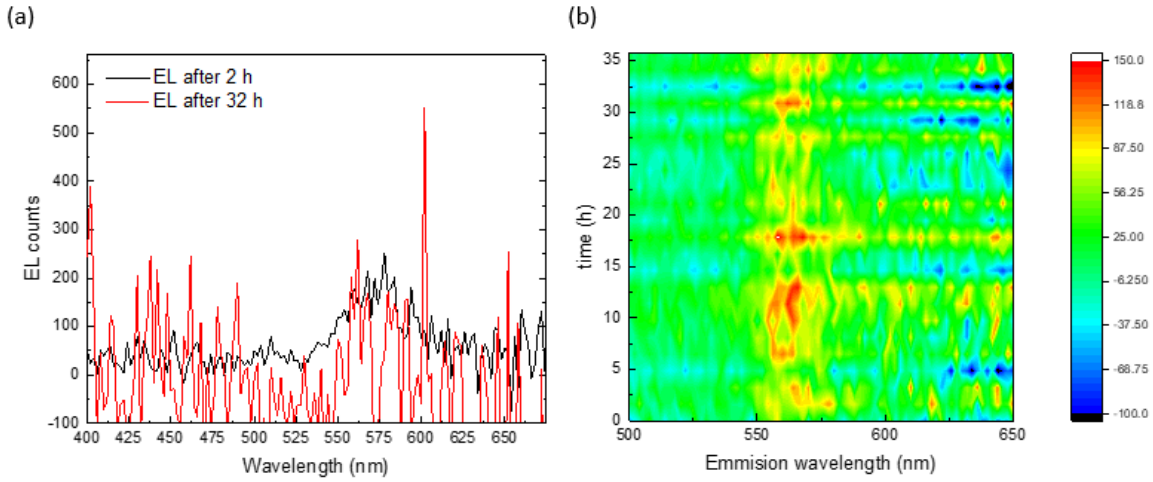

Figure 5.7: (a) EL spectra for the device after 2 and 32 hours of voltage application. (b) Change in emission intensity with time.

Fig. 5.7(a) shows the first and last spectra of the LEC device, whereas (b) depicts the emission intensity change with time. The periodic change in intensity over the 32 hours may be an effect of fluctuations in the power source. A second identical device tested in the same way showed similar behaviour. The normalized intensity of the

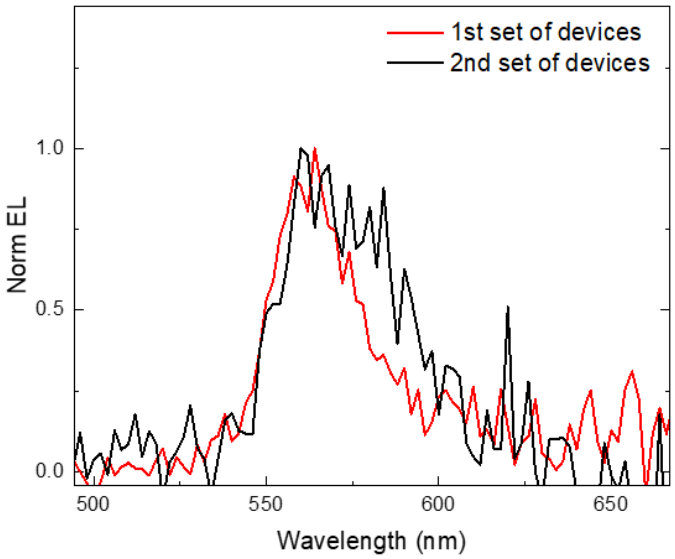

Figure 5.8: Normalized electroluminescence against wavelength for both devices tested.

electroluminescence of the two devices is shown in Fig. 5.8. No signal was observed when using a voltage lower than 3 V.

Comparing the shape of the EL and PL spectra it is evident that they appear to be quite similar, with the exception that the EL appears shifted. (Fig. 5.9) This is consistent with emission seen previously in CdSe[207-211] and ZnO[198, 205, 212] devices.

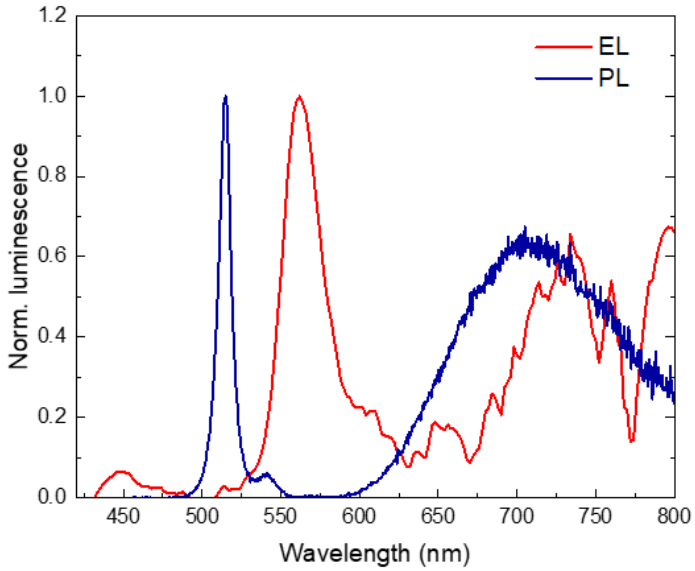

Figure 5.9: Comparison of normalized electroluminescence (red) and photoluminescence (blue) for the CdSe nanoplatelets.

While encouraging that EL was detected with the improvised experimental set-up, it was immediately apparent from these results that in order to improve the intensity or to

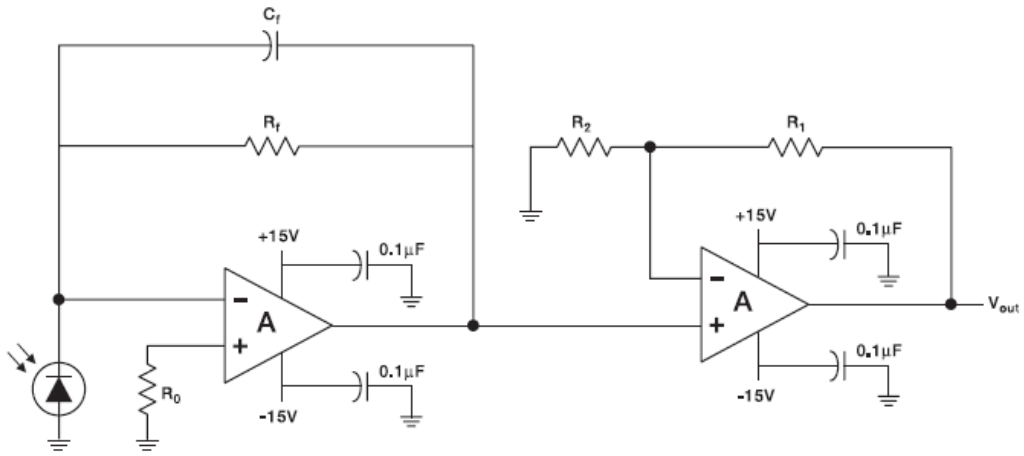

Figure 5.10: Circuit design for incorporation of a photodiode.

extend the work to other materials it was necessary to come up with a means to optimize the emission. A design was implemented to incorporate a photodiode in a circuit with operational amplifiers in order to detect and amplify the signal from any incident photons. This circuit is shown in Fig. 5.10. This circuit was encased in a compact unit with a glass aperture providing access to the photodiode for any emitted light.

Up to this point devices were operated in an inert environment. Unfortunately, due to maintenance for an extended period, access to a glovebox was not available for these initial tests with the photodiode set-up. To mitigate these circumstances, the ionic liquid used for subsequent tests was degassed in a vacuum oven overnight prior to each test, and only administered in the moments before testing was due to commence. The concern with using ionic liquid in ambient conditions is that the water absorbed from the air can reduce its electrochemical window, which essentially limits the voltage range within which the LEC can be expected to function. The following experiments were carried out under the assumption that this reduction in the electrochemical window would proceed slowly enough to allow the devices to be quickly tested.

LECs were prepared with an identical architecture as those previously described, but on this occasion some with zinc oxide (ZnO) as active material were also assembled.

Preliminary operation of the LECs in ambient conditions with low voltages applied did not result in any light emission. Conscious of the effect of water on the ionic liquid, the voltage was increased in an attempt to reduce the turn-on time for the device. Applying a potential difference of 45 V across the ZnO device produced visible light emission after approx. 2.5 minutes, with a corresponding increase in the current through the device.

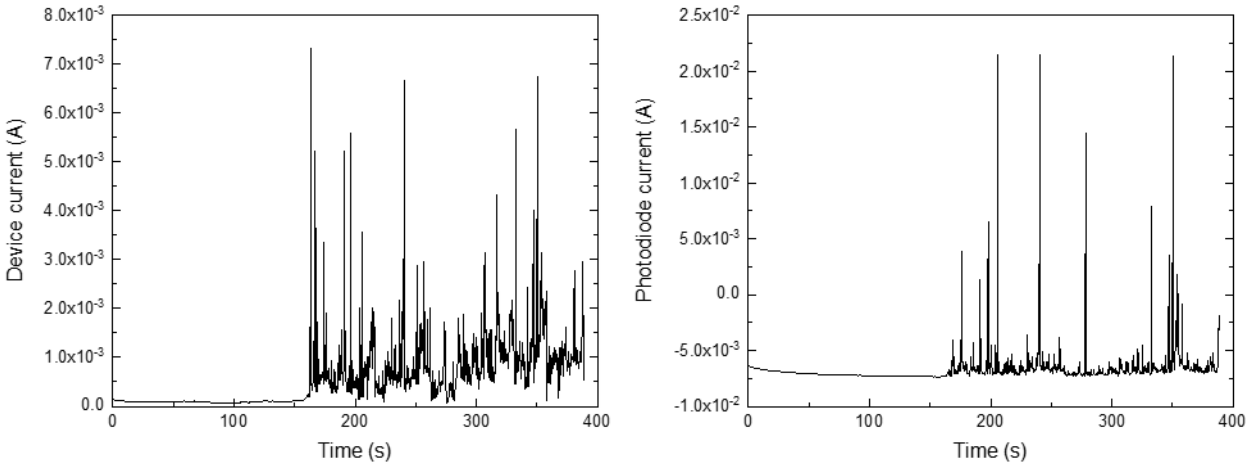

Figure 5.11: Current response over time to application of a constant voltage of 45 V for the device, and photocurrent generated in response to light emanating from the device and impinging on the photodiode.

Operation at such high voltage is well outside the effective range of the ionic liquid, therefore it appears that any emission observed was not due to the device operating as intended. Additionally, after this apparent activation of the device, emission was observed for voltages as low as 18 V (similar to observed turn-on voltage for ZnO OLED devices[198]), with a corresponding decrease in the intensity of the emitted light.

As has been reported for ZnO LED devices previously, voltages higher than 30 V resulted in visible deterioration of the device morphology.

Subjecting the CdSe devices to the same parameters did not result in emission.

5.5 Experimental Procedure

Graphene Preparation:

The graphene dispersions first underwent a cleaning step by sonicating graphite (Asbury, Grade 3763) in 80 mL NMP for 1 hour using a horn probe sonic tip at 60 % amplitude with an on/off pulse ratio of 6s/2s. The initial concentration of graphite used was 40 mg/mL. After sonication the dispersion was subjected to centrifugation at 3218 g for 1 hour. Following this centrifugation step the supernatant was discarded and the sediment was redispersed in fresh solvent (80 mL NMP). The redispersed material was sonicated again using the same conditions, but this time for 6 hours. The resulting sample was size selected by centrifuging between 2 and 6 krpm. After the 6 k step the supernatant (containing very small nanosheets suspended in NMP) was discarded, and the sediment was redispersed in IPA. In order to optimize the spraying process, a portion of the graphene in IPA was diluted to a concentration of 1 mg/mL for spraying, while the remainder was kept in a vial at higher concentration for easier storage.

Substrate Preparation:

Prior to device assembly by spraying, it was necessary to prepare suitable substrates by selective etching of indium-tin-oxide (ITO) coated glass slides. This was achieved by immersing the slides in aqueous acid solution composed of 20 % HCl and 5 % HNO_3, followed by an aqueous basic solution of 10 % Na_2CO_3.

Initially the glass slides were cut into squares with dimensions of 1.5 cm by 1.5 cm to match the specifications for the spin-coater, which would later be used to add a layer of Pedot PSS. The areas where the ITO coating was desired were coated in Kapton tape to shield the ITO from the solutions. All uncovered areas had the ITO completely removed. The acid bath was heated to 55 degrees using a hot plate, and the substrate was then lowered into the bath and remained there for 3 mins. Following this the substrate was transferred to the other bath containing the basic solution to neutralize any residual acid. This step was followed by rinsing using deionised water.

Having concluded the etching process, the slides were cleaned via sonication, first in acetone and then in IPA, each for 5 minutes.

A layer of Pedot PSS (PPSS) was applied to the etched substrates via spin-coating. A pipette was used to drop 30 µL of the PPSS on to the surface of the substrate, which was then allowed to settle for 30 seconds. Two steps of spin-coating were employed to distribute the PPSS evenly. The first step was slow (500 rpm) for 30 seconds and was followed by a much faster step at 6000 rpm, also for 30 seconds. In this case a Kapton tape mask was applied to the areas not to be spin-coated, while the ITO was left exposed and subsequently covered in a layer of PPSS. Excess PPSS that adhered to the underside of the substrate was scraped off using a blade. Immediately after spin-coating the substrates were placed on a hot plate at 100 °C for 1 minute to accelerate the drying of the PPSS.

Using profilometry the thickness of the PPSS coating was determined to be approximately 200 nm.

Device Assembly:

The active material of the device (ZnO/CdSe) was sprayed-deposited on the substrate parallel to and overlapping the conductive strip of ITO and PPSS. After allowing sufficient time for this active layer to dry, graphene was sprayed perpendicular to the direction of the ITO/PPSS strip with the end of the graphene section overlapping the active material. In this manner a region was created that consisted of an ITO/PPSS electrode below the active layer, with graphene on top functioning as an upper electrode.

Contacts were added to both the graphene strip and the ITO/PPSS close to the edge of the substrate in order to facilitate convenient placement of conductive probes for biasing the device.

Immediately before testing a drop of degassed ionic liquid (IL) was pipetted onto the active area of the device to introduce an abundance of charge carriers. Excess liquid was absorbed away using filter paper.

Initial Tests:

The first devices fabricated with CdSe nanoplates were encapsulated in a sealed chamber filled with Argon with a glass window functioning as an aperture for any emitted light.

An external power source applied a voltage across the device, and a PL detector was used to record any emitted light from it.

Photodiode Operation:

Tests were carried out using an Agilent B2912A dual-channel source-measure unit, interfaced with Keysight software. Channel 1 was floated and operated as an ammeter on the photodetector, while channel 2 was used to apply DC voltage across the devices. The electrodes were contacted with tungsten probes controlled by Imina miBot nanomanipulators.

The device was supported on a glass slide directly above the aperture window to a photodiode connected to Channel 1 of the source meter. A schematic of the test setup is shown in Fig.

During testing the set up was covered to avoid any external light source impinging on the photodiode.

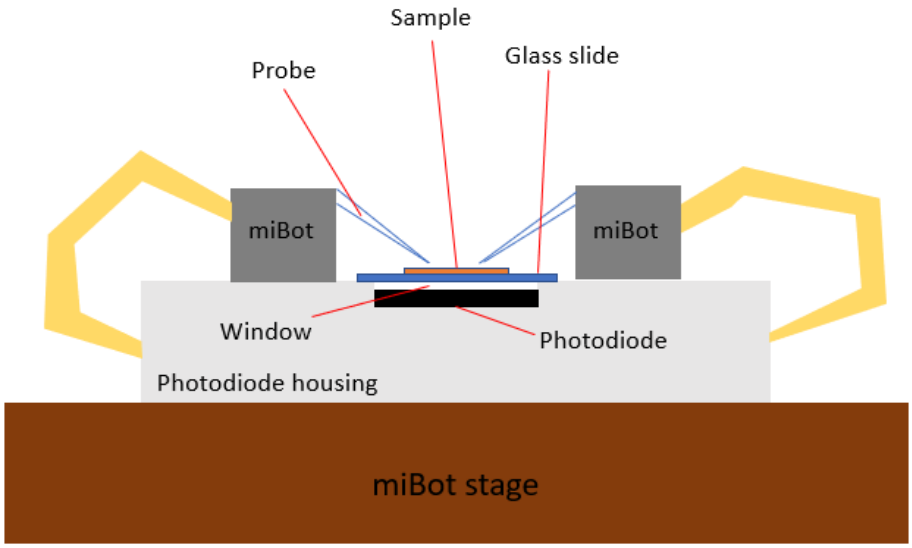

Figure 5.12: Schematic for LEC device testing with photodiode.

6

Contributions to Other Publications

Exfoliation in endotoxin-free albumin generates pristine graphene with reduced inflammatory properties, Filipa Lebre, Damien Hanlon, John B. Boland, Jonathan N. Coleman and Ed C. Lavelle. *Advanced Biosystems*, 2018, 2, 1800102. [213]

&

Pristine graphene induces innate immune training, Filipa Lebre, John B. Boland, Pedro Gouveia, Aoife Gorman, Mimmi Lundahl, Fergal O'Brien, Jonathan N. Coleman and Ed C. Lavelle. Submitted to *Nanoscale* November 2019.

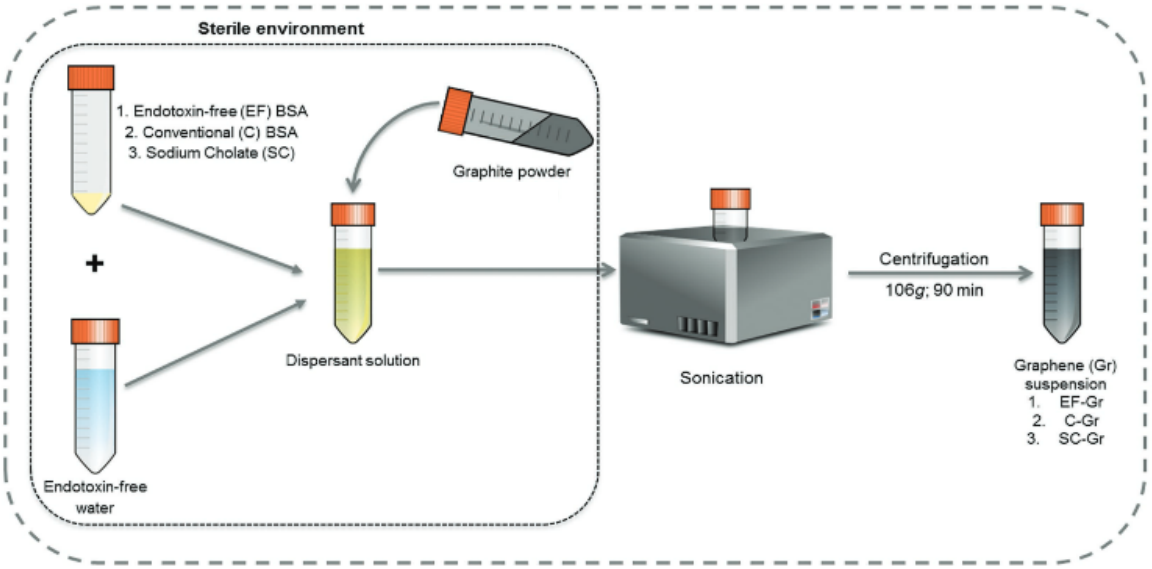

Figure 6.1: Procedure for preparation of endotoxin-free graphene dispersions. [186]

This work describes the use of liquid exfoliation to prepare endotoxin-free graphene dispersed in bovine serum albumin (BSA). These graphene dispersions show potential for use in biomedical applications after demonstrating short-term biocompatibility.

The lead researcher on this project, Dr Filipa Lebre, provided vials of graphite (Asbury Carbons, Grade 3763) in dispersal solutions, each of which consisted of water and one of the following: endotoxin-free BSA, conventional BSA or sodium cholate. These vials were sonicated as received in a bath for 6 hours. A cooling system was employed during

sonication to maintain the temperature at 10 ℃ and a stirrer was used to rotate the vials. This avoids one sample receiving more sonic energy than another due to its position in the bath, and thus keeps the exfoliation process consistent. The resulting dispersions were centrifuged by Dr Lebre and she then provided an aliquot of each for analysis using UV-vis spectroscopy. Early work in this project by Dr Damien Hanlon allowed the determination of the graphene concentration from the extinction spectrum of each sample. It was therefore possible to provide Dr Lebre with the concentration of each dispersion prepared in this manner throughout the duration of the project.

Carbon nanotubes-bridged molybdenum trioxide nanosheets as high performance anode for lithium ion batteries, Haiyan Sun, Damien Hanlon, Duc Anh Dinh, John B. Boland, Antonio Esau Del Rio Castillo, Carlo Di Giovanni, Alberto Ansaldo, Vittorio Pellegrini, Jonathan N. Coleman and Francesco Bonaccorso. *2D Mater.*, 2018, 5, 015024. [214]

&

Dependence of photocurrent enhancements in quantum dot (QD) sensitized MoS_2 devices on MoS_2 film properties, John J. Gough, Niall McEvoy, Maria O'Brien, Alan P. Bell, David McCloskey, John B. Boland, Jonathan N. Coleman, Georg S. Duesberg, A. Louise Bradley. *Adv. Funct. Mater.*, 2018, 28, 1706149. [215]

Multiple dispersions of molybdenum trioxide (MoO_3) were provided using exfoliation parameters previously published by Hanlon et al. Briefly, the starting material was added to an aluminum vessel with 80 mL isopropanol and sonicated for 5 hours using a horn probe sonic tip at an amplitude of 60 % and an on/off pulse ratio of 6s/2s. The vessel was cooled continuously throughout the sonication. Unexfoliated material was removed via centrifugation at 1000 rpm for 20 minutes. The supernatant was decanted and centrifuged at 5000 rpm to remove the smallest flakes. The remaining sediment was then redispersed in fresh isopropanol.

Graphene-coated polymer foams as tuneable impact sensors, Conor S. Boland, Umar Khan, Matthew Binions, Sebastian Barwich, John B. Boland, Denis Weaire and Jonathan N. Coleman. *Nanoscale*, 2018, 10, 5366-5375. [216]

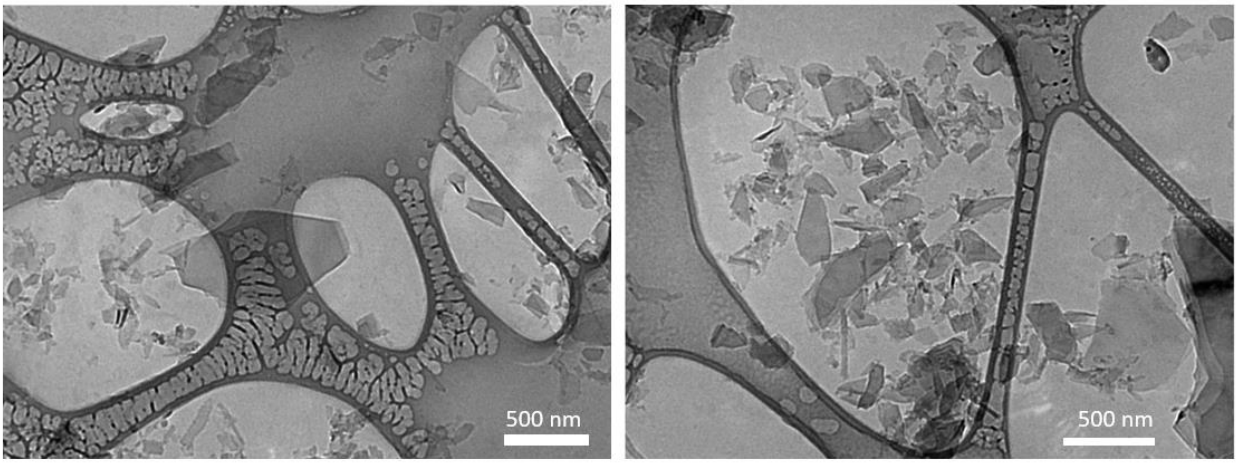

Figure 6.2: TEM images of graphene nanosheets.

Whiskey-phase exfoliation: exfoliation and printing of nanosheets using Irish whiskey, Adam G. Kelly, Victor Vega-Mayoral, John B. Boland and Jonathan N. Coleman. *2D Mater.*, 2019, 6, 045036. [88]

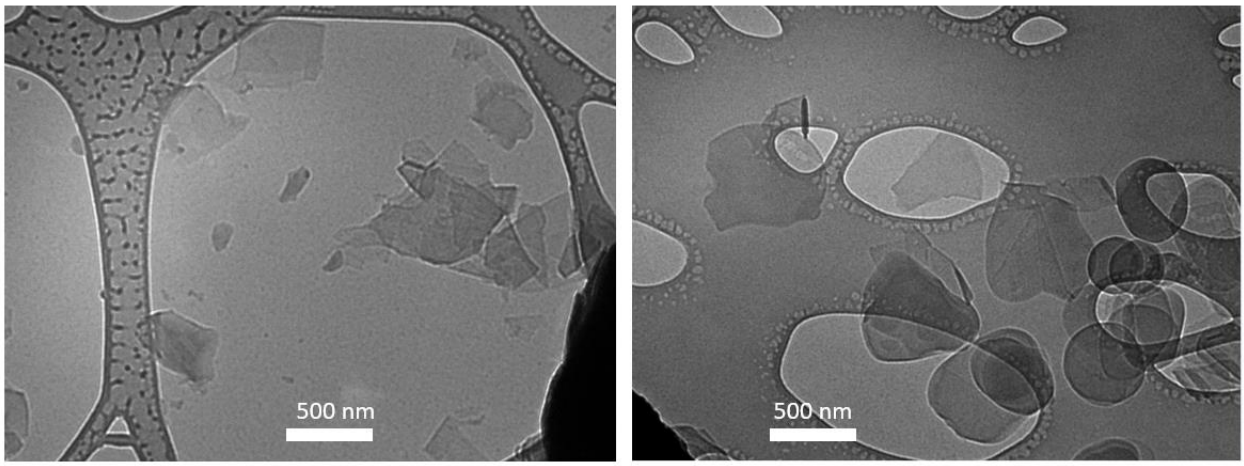

Figure 6.3: Graphene (left) and boron nitride (right) nanosheets produced via exfoliation in whiskey.

Liquid exfoliated $Co(OH)_2$ nanosheets as low-cost, yet high-performance, catalysts for the oxygen evolution reaction, David Mcateer, Ian Godwin, Zheng Ling, Andrew Harvey, Lily He, Conor S. Boland, Victor Vega-Mayoral, Beata Szydlowska, Aurelie A. Rovetta, Claudia Backes, John B. Boland, Xin Chen, Michael E. G. Lyons and Jonathan N. Coleman. *Adv. Energy Mater.,* 2018, 8, 1702965.

Multiple dispersions of cobalt hydroxide ($Co(OH)_2$) were prepared and size selected for testing. The powder was pretreated via sonication in deionised water for 2 hours. This dispersion was then centrifuged at 4500 rpm for 1 hour, retaining the sediment and discarding the supernatant. This pretreated $Co(OH)_2$ was then sonicated in surfactant and deionised water (horn probe sonic tip, 60 % amplitude, 6s/2s on/off pulse ratio, with constant cooling). Liquid cascade centrifugation was used to size select the subsequent exfoliated dispersion, with the following size fractions being isolated: 0.5-1 k, 1-1.5 k, 1.5-2 k, 2-2.5 k and 2.5-3 k rpm.

7

Ongoing and future work

Chapters 3 & 4 describe the extension of LPE to new 2D materials, adding to the list of those previously exfoliated in this manner. However, there remain myriad materials predicted to have a layered structure, all of which are potential candidates for exfoliation using this methodology in the future. The versatility of LPE means that the established protocols used in past research are almost universally applicable to layered materials. Additionally, the observed variations in optical properties with nanosheet size suggests that spectroscopic metrics for mean nanosheet size and concentration can be developed for any materials successfully exfoliated using this technique.

Previous work with air-unstable layered materials such as black phosphorus has been built upon in the exfoliation studies of MoO_2 and GeS. The ability to stabilize these materials to the point where they can be used for applications such as batteries suggests that other materials deemed unstable (and perhaps ignored for that reason) could be utilised in the same manner.

Light emitting devices represent a new direction for LPE material applications. Chapter 5 describes the emission of light from an LEC composed of CdSe nanoplatelets as active material and graphene prepared via LPE functioning as electrode material. This preliminary work provides a first glimpse into a potentially exciting new field for LPE devices, with the long- term goal of fabricating devices composed almost entirely of components processed from LPE dispersions. A new experimental setup for testing LEC devices is currently in development, one which will facilitate easier and more consistent testing of these devices in an inert environment.

The variation in bandgap with changes in thickness from bulk to nanoscale for many layered materials increases the pool of materials potentially available for use in these devices. In the immediate future this research is to be extended to InSe, a semiconductor layered material observed to exhibit luminescence. Given the simplicity of these devices compared to state of the art OLED technology, it is possible that LECs will become a viable alternative in the field of solid-state lighting in future. In order to make this a reality it is first necessary to overcome some of the challenges faced in making LECs, such as

slow turn-on times, their inherent self-limiting nature and the instability introduced by addition of ionic liquids.

8

References

1. K. S. Novoselov, A. K. Geim, S. V. Morozov, D. Jiang, Y. Zhang, S. V. Dubonos, I. V. Grigorieva and A. A. Firsov, *science*, 2004, **306**, 666-669.
2. J. Sun, X. Li, W. Guo, M. Zhao, X. Fan, Y. Dong, C. Xu, J. Deng and Y. Fu, *Crystals*, 2017, **7**, 198.
3. N. J. Coville, S. D. Mhlanga, E. N. Nxumalo and A. Shaikjee, *South African Journal of Science*, 2011, **107**, 01-15.
4. J. Dinsley, *The Complete Handbook of Medicinal Charcoal and its applications. Published by GateKeepers Book (2006) ISBN 10: 0973846402 ISBN 13: 9780973846409*, 2006.
5. B. Selinger, *Chemistry in Australia*, 2019, 37.
6. J. D. Verhoeven, *steel research*, 2002, **73**, 356-365.
7. M. Reibold, P. Paufler, A. Levin, W. Kochmann, N. Pätzke and D. Meyer, *Nature*, 2006, **444**, 286.
8. T. D. Burchell, *Carbon materials for advanced technologies*, Elsevier, 1999.
9. M. Terrones, A. R. Botello-Méndez, J. Campos-Delgado, F. Lopez-Urias, Y. I. Vega-Cantú, F. J. Rodríguez-Macías, A. L. Elías, E. Munoz-Sandoval, A. G. Cano-Márquez and J.-C. Charlier, *Nano today*, 2010, **5**, 351-372.
10. J. W. Zondlo, *Graphite, Graphene, and Their Polymer Nanocomposites*, 2012, 1-56.
11. S. Iijima, *Journal of Crystal Growth*, 1980, **50**, 675-683.
12. H. W. Kroto, J. R. Heath, S. C. O'Brien, R. F. Curl and R. E. Smalley, *Nature*, 1985, **318**, 162.
13. Q.-L. Yan, M. Gozin, F.-Q. Zhao, A. Cohen and S.-P. Pang, *Nanoscale*, 2016, **8**, 4799-4851.
14. E. T. Thostenson, Z. Ren and T.-W. Chou, *Composites science and technology*, 2001, **61**, 1899-1912.
15. L. Boumia, M. Zidour, A. Benzair and A. Tounsi, *Physica E: Low-dimensional Systems and Nanostructures*, 2014, **59**, 186-191.
16. M. Rahmandoust and A. Öchsner, 2011.
17. C. L. Kane and E. Mele, *Physical Review Letters*, 1997, **78**, 1932.
18. M. Meo and M. Rossi, *Composites Science and Technology*, 2006, **66**, 1597-1605.
19. A. K. Geim and K. S. Novoselov, in *Nanoscience and Technology: A Collection of Reviews from Nature Journals*, World Scientific, 2010, pp. 11-19.
20. Y. Hernandez, V. Nicolosi, M. Lotya, F. M. Blighe, Z. Sun, S. De, I. McGovern, B. Holland, M. Byrne and Y. K. Gun'Ko, *Nature nanotechnology*, 2008, **3**, 563.
21. D. Hanlon, C. Backes, T. M. Higgins, M. Hughes, A. O'Neill, P. King, N. McEvoy, G. S. Duesberg, B. Mendoza Sanchez and H. Pettersson, *Chemistry of Materials*, 2014, **26**, 1751-1763.
22. Z. Xiang, Q. Zhang, Z. Zhang, X. Xu and Q. Wang, *Ceramics International*, 2015, **41**, 977-981.
23. K. M. Hercule, Q. Wei, A. M. Khan, Y. Zhao, X. Tian and L. Mai, *Nano letters*, 2013, **13**, 5685-5691.
24. S. Hou, G. Zhang, W. Zeng, J. Zhu, F. Gong, F. Li and H. Duan, *ACS applied materials & interfaces*, 2014, **6**, 13564-13570.
25. N. Dukstiene, D. Sinkeviciute and A. Guobiene, *Central European Journal of Chemistry*, 2012, **10**, 1106-1118.

26. Y. Liang, Z. Yi, X. Lei, X. Ma, S. Yang, J. Sun, L. Yuan and Y. Zhou, *Journal of alloys and compounds*, 2006, **421**, 133-135.
27. F. Wang and B. Lu, *Physica B: Condensed Matter*, 2009, **404**, 1901-1904.
28. L. Wang, G.-H. Zhang and K.-C. Chou, *International Journal of Refractory Metals and Hard Materials*, 2016, **57**, 115-124.
29. J. A. Marinsky, *The radiochemistry of germanium*, National Academies, 1961.
30. E. G. Rochow and E. W. Abel, *The Chemistry of Germanium: Tin and Lead*, Elsevier, 2014.
31. F. Li, Y. Qu and M. Zhao, *Journal of Materials Chemistry A*, 2016, **4**, 8905-8912.
32. P. Ramasamy, D. Kwak, D.-H. Lim, H.-S. Ra and J.-S. Lee, *Journal of Materials Chemistry C*, 2016, **4**, 479-485.
33. D. Tan, H. E. Lim, F. Wang, N. B. Mohamed, S. Mouri, K. Sandhaya, W. Zhang, Y. Miyauchi, M. Ohfuchi and K. Matsuda, *arXiv preprint arXiv:1606.06953*, 2016.
34. C. Lan, C. Li, Y. Yin, H. Guo and S. Wang, *Journal of Materials Chemistry C*, 2015, **3**, 8074-8079.
35. D. D. Vaughn, R. J. Patel, M. A. Hickner and R. E. Schaak, *Journal of the American Chemical Society*, 2010, **132**, 15170-15172.
36. L. Shi and Y. Dai, *Journal of Applied Crystallography*, 2014, **47**, 527-531.
37. D. Lam, K.-S. Chen, J. Kang, X. Liu and M. C. Hersam, *Chemistry of Materials*, 2018, **30**, 2245-2250.
38. G. Eda, H. Yamaguchi, D. Voiry, T. Fujita, M. Chen and M. Chhowalla, *Nano letters*, 2011, **11**, 5111-5116.
39. C.-J. Shih, A. Vijayaraghavan, R. Krishnan, R. Sharma, J.-H. Han, M.-H. Ham, Z. Jin, S. Lin, G. L. Paulus and N. F. Reuel, *Nature Nanotechnology*, 2011, **6**, 439.
40. H. Ramakrishna Matte, A. Gomathi, A. K. Manna, D. J. Late, R. Datta, S. K. Pati and C. Rao, *Angewandte Chemie International Edition*, 2010, **49**, 4059-4062.
41. A. J. Cooper, N. R. Wilson, I. A. Kinloch and R. A. Dryfe, *Carbon*, 2014, **66**, 340-350.
42. L. Chen, Z. Xu, J. Li, Y. Li, M. Shan, C. Wang, Z. Wang, Q. Guo, L. Liu and G. Chen, *Journal of Materials Chemistry*, 2012, **22**, 13460-13463.
43. P. K. Ang, S. Wang, Q. Bao, J. T. Thong and K. P. Loh, *Acs Nano*, 2009, **3**, 3587-3594.
44. J. G. Hooley, *Carbon*, 1980, **18**, 82-92.
45. A. Takagaki, M. Sugisawa, D. Lu, J. N. Kondo, M. Hara, K. Domen and S. Hayashi, *Journal of the American Chemical Society*, 2003, **125**, 5479-5485.
46. M. Adachi-Pagano, C. Forano and J.-P. Besse, *Chemical Communications*, 2000, 91-92.
47. P. Ganter, C. Ziegler, A. T. Friedrichs, V. Duppel, C. Scheu and B. V. Lotsch, *ChemNanoMat*, 2017, **3**, 411-414.
48. T. Hibino and M. Kobayashi, *Journal of Materials Chemistry*, 2005, **15**, 653-656.
49. Y. Liu, P. Chen, Y. Chen, H. Lu, J. Wang, Z. Yang, Z. Lu, M. Li and L. Fang, *RSC Advances*, 2016, **6**, 10802-10809.
50. R. Ma, Z. Liu, L. Li, N. Iyi and T. Sasaki, *Journal of Materials Chemistry*, 2006, **16**, 3809-3813.
51. M. O'brien, N. McEvoy, T. Hallam, H.-Y. Kim, N. C. Berner, D. Hanlon, K. Lee, J. N. Coleman and G. S. Duesberg, *Scientific reports*, 2014, **4**, 7374.
52. K. K. Kim, A. Hsu, X. Jia, S. M. Kim, Y. Shi, M. Hofmann, D. Nezich, J. F. Rodriguez-Nieva, M. Dresselhaus and T. Palacios, *Nano letters*, 2011, **12**, 161-166.
53. X. Li, W. Cai, J. An, S. Kim, J. Nah, D. Yang, R. Piner, A. Velamakanni, I. Jung and E. Tutuc, *science*, 2009, **324**, 1312-1314.
54. J. Yu, J. Li, W. Zhang and H. Chang, *Chemical science*, 2015, **6**, 6705-6716.
55. Y. Hotta, H. Yilmaz, T. Shirai, K. Ohota, K. Sato and K. Watari, *Journal of the American Ceramic Society*, 2008, **91**, 1095-1101.

56. N. Omura, Y. Hotta, K. Sato, Y. Kinemuchi, S. Kume and K. Watari, *Journal of the American Ceramic Society*, 2006, **89**, 2738-2743.
57. N. Omura, Y. Hotta, K. Sato, Y. Kinemuchi, S. Kume and K. Watari, *Journal of the European Ceramic Society*, 2007, **27**, 733-737.
58. A. D. R. Castillo, V. Pellegrini, A. Ansaldo, F. Ricciardella, H. Sun, L. Marasco, J. Buha, Z. Dang, L. Gagliani and E. Lago, *Materials Horizons*, 2018, **5**, 890-904.
59. Y. Tominaga, K. Sato, D. Shimamoto, Y. Imai and Y. Hotta, *Ceramics International*, 2015, **41**, 10512-10519.
60. W. Zhao, M. Fang, F. Wu, H. Wu, L. Wang and G. Chen, *Journal of materials chemistry*, 2010, **20**, 5817-5819.
61. I.-Y. Jeon, Y.-R. Shin, G.-J. Sohn, H.-J. Choi, S.-Y. Bae, J. Mahmood, S.-M. Jung, J.-M. Seo, M.-J. Kim and D. W. Chang, *Proceedings of the National Academy of Sciences*, 2012, **109**, 5588-5593.
62. A. Ciesielski and P. Samorì, *Chemical Society Reviews*, 2014, **43**, 381-398.
63. D. Nuvoli, L. Valentini, V. Alzari, S. Scognamillo, S. B. Bon, M. Piccinini, J. Illescas and A. Mariani, *Journal of Materials Chemistry*, 2011, **21**, 3428-3431.
64. A. B. Bourlinos, V. Georgakilas, R. Zboril, T. A. Steriotis and A. K. Stubos, *small*, 2009, **5**, 1841-1845.
65. Y. Wang, Z. Shi and J. Yin, *Journal of Materials Chemistry*, 2011, **21**, 11371-11377.
66. S. Xie, O. M. Istrate, P. May, S. Barwich, A. P. Bell, U. Khan and J. N. Coleman, *Nanoscale*, 2015, **7**, 4443-4450.
67. H. Ye, T. Lu, C. Xu, B. Han, N. Meng and L. Xu, *Macromolecular Chemistry and Physics*, 2018, **219**, 1700482.
68. A. Harvey, C. Backes, Z. Gholamvand, D. Hanlon, D. McAteer, H. C. Nerl, E. McGuire, A. s. Seral-Ascaso, Q. M. Ramasse and N. McEvoy, *Chemistry of Materials*, 2015, **27**, 3483-3493.
69. C. Zhang, S. H. Park, O. Ronan, A. Harvey, A. Seral-Ascaso, Z. Lin, N. McEvoy, C. S. Boland, N. C. Berner and G. S. Duesberg, *Small*, 2017, **13**, 1701677.
70. A. Winchester, S. Ghosh, S. Feng, A. L. Elias, T. Mallouk, M. Terrones and S. Talapatra, *ACS applied materials & interfaces*, 2014, **6**, 2125-2130.
71. G. S. Bang, K. W. Nam, J. Y. Kim, J. Shin, J. W. Choi and S.-Y. Choi, *ACS applied materials & interfaces*, 2014, **6**, 7084-7089.
72. K. Lee, H. Y. Kim, M. Lotya, J. N. Coleman, G. T. Kim and G. S. Duesberg, *Advanced materials*, 2011, **23**, 4178-4182.
73. R. Jha and P. K. Guha, *Journal of materials science*, 2017, **52**, 7256-7268.
74. D. O'Suilleabhain, V. Vega-Mayoral, A. G. Kelly, A. Harvey and J. N. Coleman, *ACS applied materials & interfaces*, 2019, **11**, 8545-8555.
75. R. Woodward, R. Howe, T. Runcorn, G. Hu, F. Torrisi, E. Kelleher and T. Hasan, *Optics express*, 2015, **23**, 20051-20061.
76. Z. Luo, Y. Li, M. Zhong, Y. Huang, X. Wan, J. Peng and J. Weng, *Photonics Research*, 2015, **3**, A79-A86.
77. F. Song and X. Hu, *Nature communications*, 2014, **5**, 4477.
78. A. Harvey, X. He, I. J. Godwin, C. Backes, D. McAteer, N. C. Berner, N. McEvoy, A. Ferguson, A. Shmeliov and M. E. Lyons, *Journal of Materials Chemistry A*, 2016, **4**, 11046-11059.
79. A. Rovetta, M. Browne, A. Harvey, I. Godwin, J. Coleman and M. Lyons, *Nanotechnology*, 2017, **28**, 375401.
80. D. McAteer, I. J. Godwin, Z. Ling, A. Harvey, L. He, C. S. Boland, V. Vega-Mayoral, B. Szydłowska, A. A. Rovetta and C. Backes, *Advanced Energy Materials*, 2018, **8**, 1702965.

81. P. Yasaei, B. Kumar, T. Foroozan, C. Wang, M. Asadi, D. Tuschel, J. E. Indacochea, R. F. Klie and A. Salehi-Khojin, *Advanced Materials*, 2015, **27**, 1887-1892.
82. S. Lin, Y. Chui, Y. Li and S. P. Lau, *FlatChem*, 2017, **2**, 15-37.
83. M. M. Alsaif, M. R. Field, T. Daeneke, A. F. Chrimes, W. Zhang, B. J. Carey, K. J. Berean, S. Walia, J. van Embden and B. Zhang, *ACS applied materials & interfaces*, 2016, **8**, 3482-3493.
84. J. B. Boland, A. Harvey, R. Tian, D. Hanlon, V. Vega-Mayoral, B. Szydlowska, A. Griffin, T. Stimpel-Lindner, S. Jaskaniec and V. Nicolosi, *Nanoscale Advances*, 2019, **1**, 1560-1570.
85. C. Gibaja, D. Rodriguez-San-Miguel, P. Ares, J. Gómez-Herrero, M. Varela, R. Gillen, J. Maultzsch, F. Hauke, A. Hirsch and G. Abellán, *Angewandte Chemie International Edition*, 2016, **55**, 14345-14349.
86. V. Vega-Mayoral, R. Tian, A. G. Kelly, A. Griffin, A. Harvey, M. Borrelli, K. Nisi, C. Backes and J. N. Coleman, *Nanoscale*, 2019, **11**, 6206-6216.
87. A. Harvey, J. B. Boland, I. Godwin, A. G. Kelly, B. M. Szydłowska, G. Murtaza, A. Thomas, D. J. Lewis, P. O'Brien and J. N. Coleman, *2D Materials*, 2017, **4**, 025054.
88. A. G. Kelly, V. Vega-Mayoral, J. B. Boland and J. N. Coleman, *2D Materials*, 2019, **6**, 045036.
89. M. S. Arnold, A. A. Green, J. F. Hulvat, S. I. Stupp and M. C. Hersam, *Nature nanotechnology*, 2006, **1**, 60.
90. J. Zhu, J. Kang, J. Kang, D. Jariwala, J. D. Wood, J.-W. T. Seo, K.-S. Chen, T. J. Marks and M. C. Hersam, *Nano letters*, 2015, **15**, 7029-7036.
91. M. S. Arnold, S. I. Stupp and M. C. Hersam, *Nano letters*, 2005, **5**, 713-718.
92. A. A. Green and M. C. Hersam, *Nano letters*, 2009, **9**, 4031-4036.
93. A. A. Green and M. C. Hersam, *Advanced Materials*, 2011, **23**, 2185-2190.
94. C. Backes, B. M. Szydłowska, A. Harvey, S. Yuan, V. Vega-Mayoral, B. R. Davies, P.-l. Zhao, D. Hanlon, E. J. Santos and M. I. Katsnelson, *ACS nano*, 2016, **10**, 1589-1601.
95. J. M. Hughes, D. Aherne and J. N. Coleman, *Journal of Applied Polymer Science*, 2013, **127**, 4483-4491.
96. M. Rubinstein, *Journal of Polymer Science Part B: Polymer Physics*, 2010, **48**, 2548-2551.
97. S. D. Bergin, Z. Sun, D. Rickard, P. V. Streich, J. P. Hamilton and J. N. Coleman, *ACS nano*, 2009, **3**, 2340-2350.
98. W. Cao, J. Wang and M. Ma, *The journal of physical chemistry letters*, 2019, **10**, 981-986.
99. G. Cunningham, M. Lotya, C. S. Cucinotta, S. Sanvito, S. D. Bergin, R. Menzel, M. S. P. Shaffer and J. N. Coleman, *ACS Nano*, 2012, **6**, 3468-3480.
100. J. N. Coleman, *Accounts of Chemical Research*, 2013, **46**, 14-22.
101. J. N. Coleman, *Advanced Functional Materials*, 2009, **19**, 3680-3695.
102. Y. Hernandez, M. Lotya, D. Rickard, S. D. Bergin and J. N. Coleman, *Langmuir*, 2009, **26**, 3208-3213.
103. T. Lindvig, M. L. Michelsen and G. M. Kontogeorgis, *Fluid Phase Equilibria*, 2002, **203**, 247-260.
104. K. S. Suslick, D. A. Hammerton and R. E. Cline, *Journal of the American Chemical Society*, 1986, **108**, 5641-5642.
105. K. S. Suslick, *science*, 1990, **247**, 1439-1445.
106. E. B. Flint and K. S. Suslick, *Science*, 1991, **253**, 1397-1399.
107. J. H. Bang and K. S. Suslick, *Advanced materials*, 2010, **22**, 1039-1059.
108. M. Ashokkumar, *Ultrasonics sonochemistry*, 2011, **18**, 864-872.
109. Y. Y. Huang and E. M. Terentjev, *Polymers*, 2012, **4**, 275-295.

110. W. Qiao, S. Yan, X. He, X. Song, Z. Li, X. Zhang, W. Zhong and Y. Du, *Rsc Advances*, 2014, **4**, 50981-50987.
111. S. P. Ogilvie, M. J. Large, M. A. O'Mara, P. J. Lynch, C. L. Lee, A. A. King, C. Backes and A. B. Dalton, *2D Materials*, 2019, **6**, 031002.
112. G. J. Kynch, *Transactions of the Faraday society*, 1952, **48**, 166-176.
113. V. Nicolosi, D. Vrbanic, A. Mrzel, J. McCauley, S. O'Flaherty, C. McGuinness, G. Compagnini, D. Mihailovic, W. J. Blau and J. N. Coleman, *The Journal of Physical Chemistry B*, 2005, **109**, 7124-7133.
114. F. Withers, H. Yang, L. Britnell, A. Rooney, E. Lewis, A. Felten, C. Woods, V. Sanchez Romaguera, T. Georgiou and A. Eckmann, *Nano letters*, 2014, **14**, 3987-3992.
115. P. Chamoli, M. K. Das and K. K. Kar, *Journal of Applied Physics*, 2017, **122**, 185105.
116. C. Backes, T. M. Higgins, A. Kelly, C. Boland, A. Harvey, D. Hanlon and J. N. Coleman, *Chemistry of Materials*, 2016, **29**, 243-255.
117. K. Suzuki, A. Kobayashi, S. Kaneko, K. Takehira, T. Yoshihara, H. Ishida, Y. Shiina, S. Oishi and S. Tobita, *Physical Chemistry Chemical Physics*, 2009, **11**, 9850-9860.
118. S. Leyre, E. Coutino-Gonzalez, J. Joos, J. Ryckaert, Y. Meuret, D. Poelman, P. Smet, G. Durinck, J. Hofkens and G. Deconinck, *Review of scientific instruments*, 2014, **85**, 123115.
119. B. Fultz and J. M. Howe, *Transmission electron microscopy and diffractometry of materials*, Springer Science & Business Media, 2012.
120. L. Reimer, *Transmission electron microscopy: physics of image formation and microanalysis*, Springer, 2013.
121. Z. Wang, *Journal*, 2000.
122. J. I. Goldstein, D. E. Newbury, J. R. Michael, N. W. Ritchie, J. H. J. Scott and D. C. Joy, *Scanning electron microscopy and X-ray microanalysis*, Springer, 2017.
123. S. J. B. Reed, *Electron microprobe analysis and scanning electron microscopy in geology*, Cambridge University Press, 2005.
124. L. Reimer, *Scanning electron microscopy: physics of image formation and microanalysis*, Springer, 2013.
125. F. J. Giessibl, *Reviews of modern physics*, 2003, **75**, 949.
126. D. Rugar and P. Hansma, *Physics today*, 1990, **43**, 23-30.
127. A. C. Ferrari, *Solid state communications*, 2007, **143**, 47-57.
128. C. V. Raman and K. S. Krishnan, *Nature*, 1928, **121**, 501.
129. A. Smekal, *Naturwissenschaften*, 1923, **11**, 873-875.
130. S. Perkowitz, *Optical characterization of semiconductors: infrared, Raman, and photoluminescence spectroscopy*, Elsevier, 2012.
131. F. Wooten, *Optical properties of solids*, Academic press, 2013.
132. T. Okpalugo, P. Papakonstantinou, H. Murphy, J. McLaughlin and N. Brown, *Carbon*, 2005, **43**, 153-161.
133. J. Wolstenholme and J. Watts, *An Introduction to Surface Analysis by XPS and AES*, J. Wiley & sons, 2003.
134. T. Yamashita and P. Hayes, *Applied surface science*, 2008, **254**, 2441-2449.
135. J.-J. Rousseau, *Basic crystallography*, John Wiley & Son Ltd, 1998.
136. R. Kohli and K. L. Mittal, *Developments in Surface Contamination and Cleaning, Vol. 1: Fundamentals and Applied Aspects*, William Andrew, 2015.
137. V. S. Ramachandran and J. J. Beaudoin, *Handbook of analytical techniques in concrete science and technology: principles, techniques and applications*, Elsevier, 2000.
138. N. Mounet, M. Gibertini, P. Schwaller, D. Campi, A. Merkys, A. Marrazzo, T. Sohier, I. E. Castelli, A. Cepellotti and G. Pizzi, *Nature nanotechnology*, 2018, **13**, 246.
139. A. Manthiram and C. Tsang, *Journal of the Electrochemical Society*, 1996, **143**, L143-L145.

140. F. Gao, L. Zhang and S. Huang, *Materials Letters*, 2010, **64**, 537-540.
141. J. Rajeswari, P. S. Kishore, B. Viswanathan and T. K. Varadarajan, *Electrochemistry communications*, 2009, **11**, 572-575.
142. C. Xia, Y. Zhou, D. B. Velusamy, A. A. Farah, P. Li, Q. Jiang, I. N. Odeh, Z. Wang, X. Zhang and H. N. Alshareef, *Nano letters*, 2018, **18**, 1506-1515.
143. A. Kim, E. Park, H. Lee and H. Kim, *Journal of Alloys and Compounds*, 2016, **681**, 301-306.
144. M. Osada and T. Sasaki, *Journal of Materials Chemistry*, 2009, **19**, 2503-2511.
145. L. Yang, Q. Gao, Y. Zhang, Y. Tang and Y. Wu, *Electrochemistry communications*, 2008, **10**, 118-122.
146. Q. Yang, Q. Liang, J. Liu, S. Liang, S. Tang, P. Lu and Y. Lu, *Materials Letters*, 2014, **127**, 32-35.
147. M. Chhowalla, H. S. Shin, G. Eda, L.-J. Li, K. P. Loh and H. Zhang, *Nature chemistry*, 2013, **5**, 263.
148. S. Balendhran, J. Z. Ou, M. Bhaskaran, S. Sriram, S. Ippolito, Z. Vasic, E. Kats, S. Bhargava, S. Zhuiykov and K. Kalantar-Zadeh, *Nanoscale*, 2012, **4**, 461-466.
149. C. J. Zhang, S.-H. Park, S. E. O'Brien, A. Seral-Ascaso, M. Liang, D. Hanlon, D. Krishnan, A. Crossley, N. McEvoy and J. N. Coleman, *Nano Energy*, 2017, **39**, 151-161.
150. C. Backes, K. R. Paton, D. Hanlon, S. Yuan, M. I. Katsnelson, J. Houston, R. J. Smith, D. McCloskey, J. F. Donegan and J. N. Coleman, *Nanoscale*, 2016, **8**, 4311-4323.
151. Z. Gholamvand, D. McAteer, A. Harvey, C. Backes and J. N. Coleman, *Chemistry of Materials*, 2016, **28**, 2641-2651.
152. D. Hanlon, C. Backes, E. Doherty, C. S. Cucinotta, N. C. Berner, C. Boland, K. Lee, A. Harvey, P. Lynch and Z. Gholamvand, *Nature communications*, 2015, **6**, 8563.
153. J. Texter, *Angewandte Chemie International Edition*, 2015, **54**, 10258-10262.
154. C. Backes, R. J. Smith, N. McEvoy, N. C. Berner, D. McCloskey, H. C. Nerl, A. O'Neill, P. J. King, T. Higgins and D. Hanlon, *Nature communications*, 2014, **5**, 4576.
155. M. Camacho-López, L. Escobar-Alarcón, M. Picquart, R. Arroyo, G. Córdoba and E. Haro-Poniatowski, *Optical Materials*, 2011, **33**, 480-484.
156. D. McAteer, I. J. Godwin, Z. Ling, A. Harvey, L. He, C. S. Boland, V. Vega-Mayoral, B. Szydłowska, A. A. Rovetta, C. Backes, J. B. Boland, X. Chen, M. E. G. Lyons and J. N. Coleman, *Advanced Energy Materials*, 2018, **8**, 1702965.
157. P. May, U. Khan, A. O'Neill and J. N. Coleman, *Journal of Materials Chemistry*, 2012, **22**, 1278-1282.
158. K. A. Olson and G. L. Schrader, *MRS Online Proceedings Library Archive*, 1990, **187**.
159. G. Rodriguez-Gattorno, A. Martínez-Hernández, L. Aleman-Vazquez and E. Torres-Garcia, *Applied Catalysis A: General*, 2007, **321**, 117-124.
160. M. Dieterle and G. Mestl, *Physical Chemistry Chemical Physics*, 2002, **4**, 822-826.
161. Y. Jin and P. K. Shen, *Journal of Materials Chemistry A*, 2015, **3**, 20080-20085.
162. E. Comini, L. Yubao, Y. Brando and G. Sberveglieri, *Chemical Physics Letters*, 2005, **407**, 368-371.
163. Y. Sun, X. Hu, W. Luo and Y. Huang, *Journal of Materials Chemistry*, 2012, **22**, 425-431.
164. J. K. Shon, H. S. Lee, G. O. Park, J. Yoon, E. Park, G. S. Park, S. S. Kong, M. Jin, J.-M. Choi and H. Chang, *Nature communications*, 2016, **7**, 11049.
165. A. Bhaskar, M. Deepa and T. Narasinga Rao, *ACS applied materials & interfaces*, 2013, **5**, 2555-2566.
166. N. Nitta, F. Wu, J. T. Lee and G. Yushin, *Materials today*, 2015, **18**, 252-264.
167. L. Zhou, H. B. Wu, Z. Wang and X. W. Lou, *ACS applied materials & interfaces*, 2011, **3**, 4853-4857.
168. Z. Xu, H. Wang, Z. Li, A. Kohandehghan, J. Ding, J. Chen, K. Cui and D. Mitlin, *The Journal of Physical Chemistry C*, 2014, **118**, 18387-18396.

169. Y. Liu, X. He, D. Hanlon, A. Harvey, J. N. Coleman and Y. Li, *ACS nano*, 2016, **10**, 8821-8828.
170. P. Poizot, S. Laruelle, S. Grugeon, L. Dupont and J. Tarascon, *Nature*, 2000, **407**, 496.
171. H. Fu, Z. Xu, T. Wang, K. Li, X. Shen, J. Li and J. Huang, *Journal of The Electrochemical Society*, 2018, **165**, A439-A447.
172. Z. Xu, T. Wang, L. Kong, K. Yao, H. Fu, K. Li, L. Cao, J. Huang and Q. Zhang, *Particle & Particle Systems Characterization*, 2017, **34**, 1600223.
173. Y. Sun, X. Hu, W. Luo and Y. Huang, *ACS nano*, 2011, **5**, 7100-7107.
174. C. Gabbett, C. S. Boland, A. Harvey, V. Vega-Mayoral, R. J. Young and J. N. Coleman, *Chemistry of Materials*, 2018, **30**, 5245-5255.
175. P. D. Antunez, J. J. Buckley and R. L. Brutchey, *Nanoscale*, 2011, **3**, 2399-2411.
176. Q. Wang, S.-Z. Kang, X. Li, Y.-W. Yang, L. Qin and J. Mu, *Journal of Alloys and Compounds*, 2015, **631**, 21-25.
177. Y. J. Cho, H. S. Im, Y. Myung, C. H. Kim, H. S. Kim, S. H. Back, Y. R. Lim, C. S. Jung, D. M. Jang and J. Park, *Chemical Communications*, 2013, **49**, 4661-4663.
178. M. T. Edmonds, A. Tadich, A. Carvalho, A. Ziletti, K. M. O'Donnell, S. P. Koenig, D. F. Coker, B. Özyilmaz, A. C. Neto and M. Fuhrer, *ACS applied materials & interfaces*, 2015, **7**, 14557-14562.
179. A. Favron, E. Gaufrès, F. Fossard, A.-L. Phaneuf-L'Heureux, N. Y. Tang, P. L. Lévesque, A. Loiseau, R. Leonelli, S. Francoeur and R. Martel, *Nature materials*, 2015, **14**, 826.
180. J. B. Boland, A. Harvey, R. Tian, D. Hanlon, V. Vega-Mayoral, B. Szydlowska, A. Griffin, T. Stimpel-Lindner, S. Jaskaniec and V. Nicolosi, *Nanoscale Advances*, 2019.
181. C. Backes, D. Campi, B. M. Szydłowska, K. Synnatschke, E. Ojala, F. Rashvand, A. Harvey, A. Griffin, Z. Sofer and N. Marzari, *ACS nano*, 2019.
182. A. Harvey, C. Backes, J. B. Boland, X. He, A. Griffin, B. Szydlowska, C. Gabbett, J. F. Donegan and J. N. Coleman, *Nature communications*, 2018, **9**, 4553.
183. E. Sutter, B. Zhang, M. Sun and P. Sutter, *ACS nano*, 2019, **13**, 9352-9362.
184. T. F. Jaramillo, K. P. Jørgensen, J. Bonde, J. H. Nielsen, S. Horch and I. Chorkendorff, *science*, 2007, **317**, 100-102.
185. G. Cunningham, M. Lotya, C. S. Cucinotta, S. Sanvito, S. D. Bergin, R. Menzel, M. S. Shaffer and J. N. Coleman, *ACS nano*, 2012, **6**, 3468-3480.
186. G. Wang, A. Chernikov, M. M. Glazov, T. F. Heinz, X. Marie, T. Amand and B. Urbaszek, *Reviews of Modern Physics*, 2018, **90**, 021001.
187. K. Synnatschke, P. Cieslik, A. Harvey, A. Castellanos-Gomez, T. Tian, C.-J. Shih, A. Chernikov, E. J. G. Santos, J. N. Coleman and C. Backes, *Chemistry of Materials*, **in press**.
188. J. D. Wiley, A. Breitschwerdt and E. Schonherr, *Solid State Communications*, 1975, **17**, 355-359.
189. R. X. Fei, W. B. Li, J. Li and L. Yang, *Applied Physics Letters*, 2015, **107**.
190. R. K. Ulaganathan, Y. Y. Lu, C. J. Kuo, S. R. Tamalampudi, R. Sankar, K. M. Boopathi, A. Anand, K. Yadav, R. J. Mathew, C. R. Liu, F. C. Chou and Y. T. Chen, *Nanoscale*, 2016, **8**, 2284-2292.
191. N. Nitta, F. X. Wu, J. T. Lee and G. Yushin, *Materials Today*, 2015, **18**, 252-264.
192. Y. Wei, J. He, Q. Zhang, C. Liu, A. Wang, H. Li and T. Zhai, *Materials Chemistry Frontiers*, 2017, **1**, 1607-1614.
193. Y. D. Liu, L. Ren, X. Qi, L. W. Yang, J. Li, Y. Wang and J. X. Zhong, *Journal of Energy Chemistry*, 2014, **23**, 207-212.
194. S. H. Park, R. Y. Tian, J. Coelho, V. Nicolosi and J. N. Coleman, *Advanced Energy Materials*, DOI: 10.1002/aenm.201901359.
195. Y. G. Zhou, *Journal of Materials Chemistry A*, 2016, **4**, 10906-10913.

196. R. D. Costa, E. Orti, H. J. Bolink, F. Monti, G. Accorsi and N. Armaroli, *Angewandte Chemie International Edition*, 2012, **51**, 8178-8211.
197. P. Matyba, H. Yamaguchi, G. Eda, M. Chhowalla, L. Edman and N. D. Robinson, *Acs Nano*, 2010, **4**, 637-642.
198. S. Jeong, S. Lee and J.-H. Boo, *Current Applied Physics*, 2004, **4**, 655-658.
199. M. D. Moore, M. H. Bowler, J. E. Reynolds III, V. M. Lynch, Y. Shen, J. D. Slinker and J. L. Sessler, *ACS applied materials & interfaces*, 2018, **10**, 24699-24707.
200. S. B. Meier, D. Tordera, A. Pertegas, C. Roldan-Carmona, E. Ortí and H. J. Bolink, *Materials Today*, 2014, **17**, 217-223.
201. S. Tang, A. Sandström, P. Lundberg, T. Lanz, C. Larsen, S. van Reenen, M. Kemerink and L. Edman, *Nature communications*, 2017, **8**, 1190.
202. S. Tang and L. Edman, in *Photoluminescent Materials and Electroluminescent Devices*, Springer, 2017, pp. 375-395.
203. Q. Pei, G. Yu, C. Zhang, Y. Yang and A. J. Heeger, *Science*, 1995, **269**, 1086-1088.
204. J. D. Slinker, J. A. DeFranco, M. J. Jaquith, W. R. Silveira, Y.-W. Zhong, J. M. Moran-Mirabal, H. G. Craighead, H. D. Abruña, J. A. Marohn and G. G. Malliaras, *Nature materials*, 2007, **6**, 894.
205. J. Pu, T. Fujimoto, Y. Ohasi, S. Kimura, C. H. Chen, L. J. Li, T. Sakanoue and T. Takenobu, *Advanced Materials*, 2017, **29**, 1606918.
206. D. Tordera, S. Meier, M. Lenes, R. D. Costa, E. Ortí, W. Sarfert and H. J. Bolink, *Advanced Materials*, 2012, **24**, 897-900.
207. A. W. Achtstein, A. Antanovich, A. Prudnikau, R. Scott, U. Woggon and M. Artemyev, *The Journal of Physical Chemistry C*, 2015, **119**, 20156-20161.
208. V. Colvin, M. Schlamp and A. P. Alivisatos, *Nature*, 1994, **370**, 354.
209. M. J. Bowers, J. R. McBride and S. J. Rosenthal, *Journal of the American Chemical Society*, 2005, **127**, 15378-15379.
210. M. Nirmal, B. O. Dabbousi, M. G. Bawendi, J. Macklin, J. Trautman, T. Harris and L. E. Brus, *Nature*, 1996, **383**, 802.
211. J. Zhao, J. A. Bardecker, A. M. Munro, M. S. Liu, Y. Niu, I.-K. Ding, J. Luo, B. Chen, A. K.-Y. Jen and D. S. Ginger, *Nano letters*, 2006, **6**, 463-467.
212. S. Choi, A. M. Berhane, A. Gentle, C. Ton-That, M. R. Phillips and I. Aharonovich, *ACS applied materials & interfaces*, 2015, **7**, 5619-5623.
213. F. Lebre, D. Hanlon, J. B. Boland, J. Coleman and E. C. Lavelle, *Advanced Biosystems*, 2018, **2**, 1800102.
214. H. Sun, D. Hanlon, D. A. Dinh, J. B. Boland, A. E. D. R. Castillo, C. Di Giovanni, A. Ansaldo, V. Pellegrini, J. N. Coleman and F. Bonaccorso, *2D Materials*, 2017, **5**, 015024.
215. J. J. Gough, N. McEvoy, M. O'Brien, A. P. Bell, D. McCloskey, J. B. Boland, J. N. Coleman, G. S. Duesberg and A. L. Bradley, *Advanced Functional Materials*, 2018, **28**, 1706149.
216. C. S. Boland, U. Khan, M. Binions, S. Barwich, J. B. Boland, D. Weaire and J. N. Coleman, *Nanoscale*, 2018, **10**, 5366-5375.

9

Appendix:

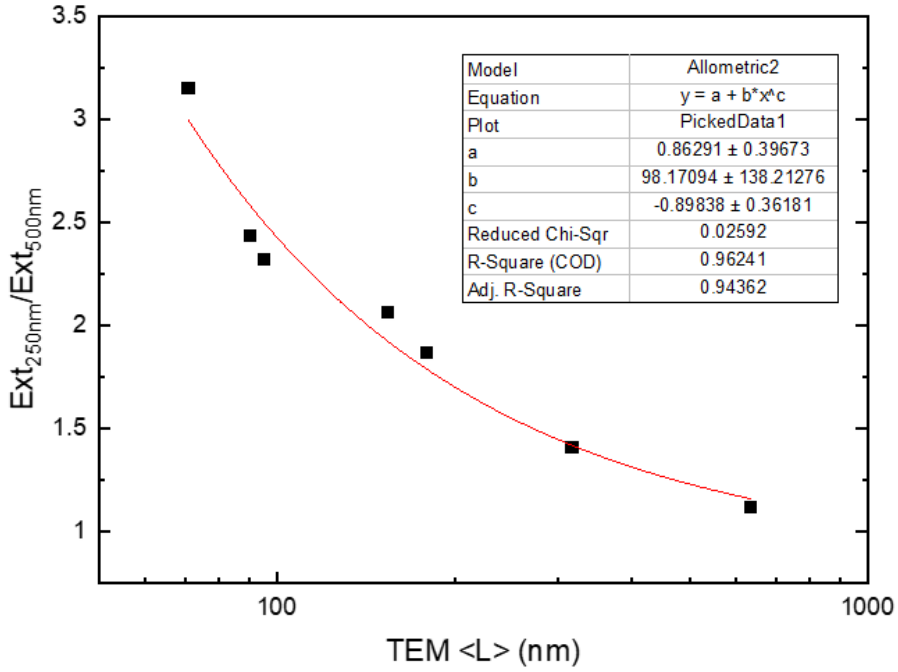

Fig 3.4 (b) fitting data.

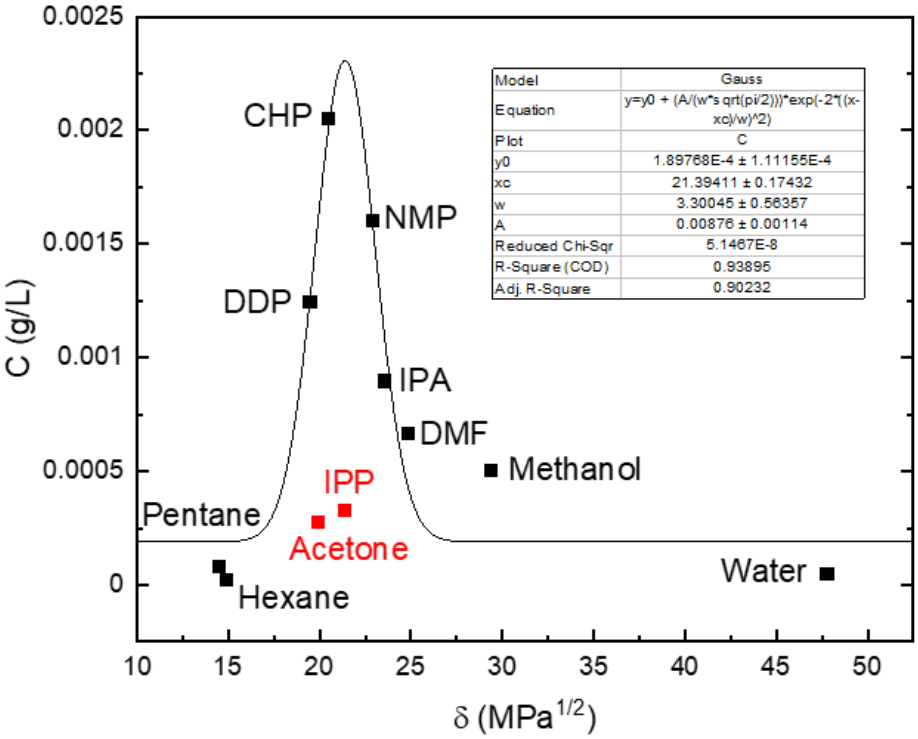

Fig 3.7 fitting data

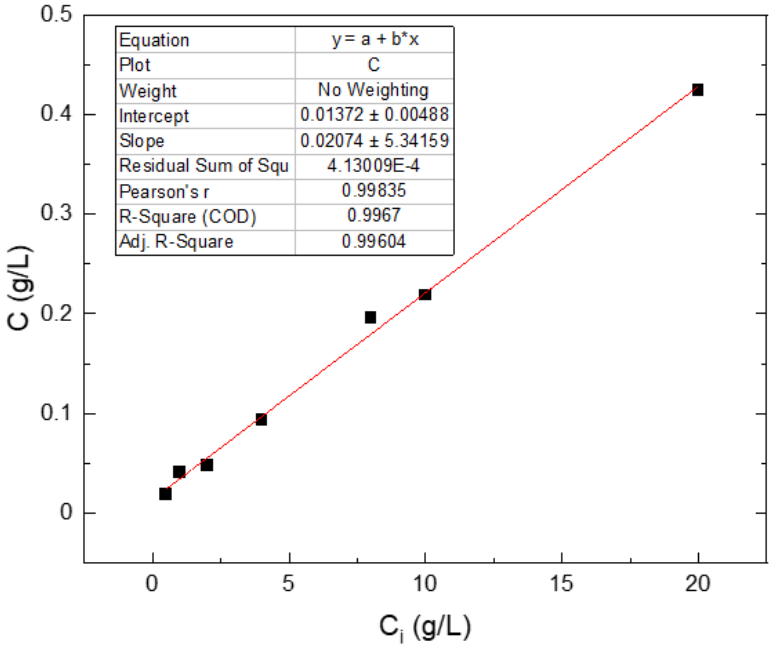

Fig 3.8 (a) fitting data.

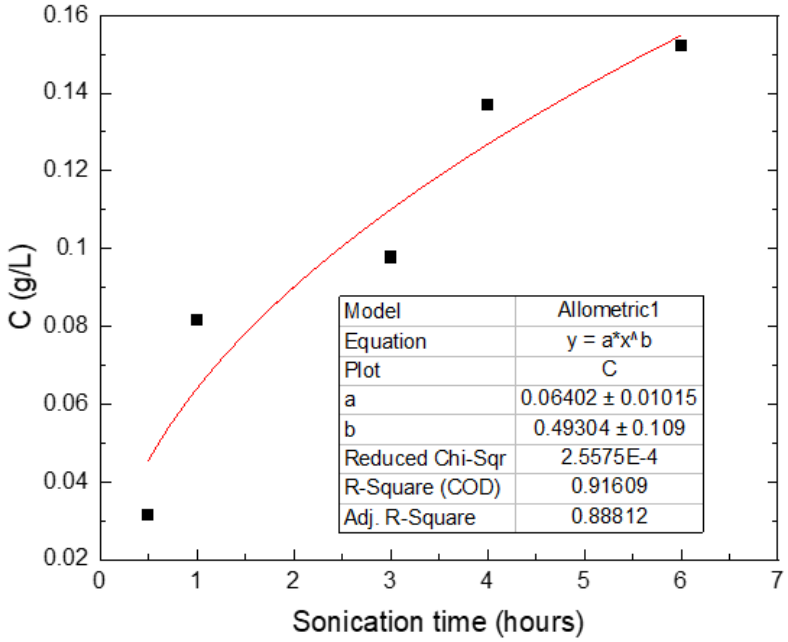

Fig 3.8 (b) fitting data.

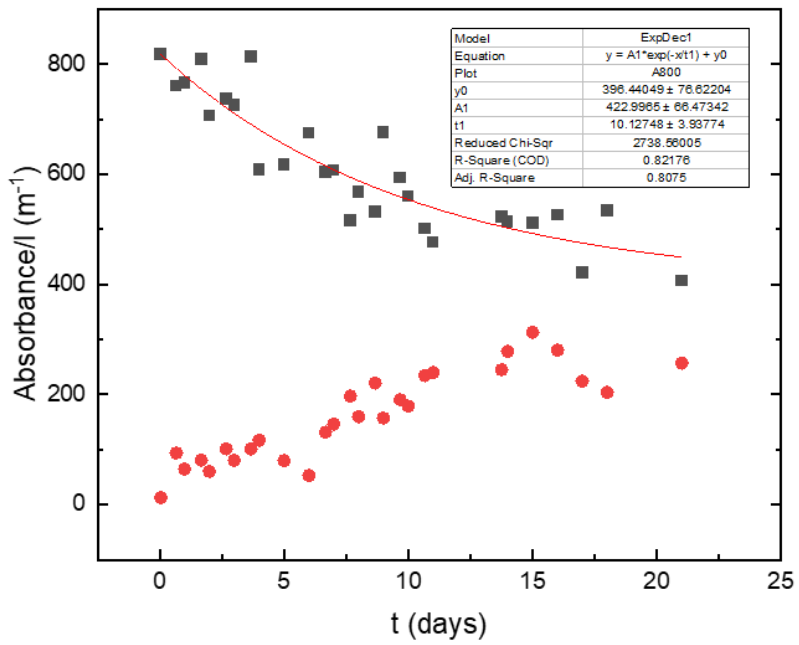

Fig 3.21 fitting data.

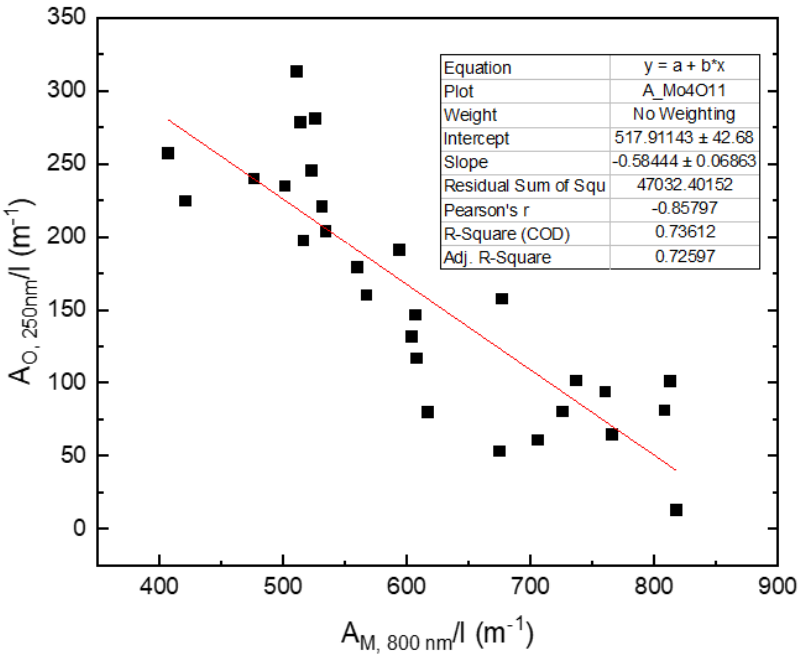

Fig 3.22 fitting data.

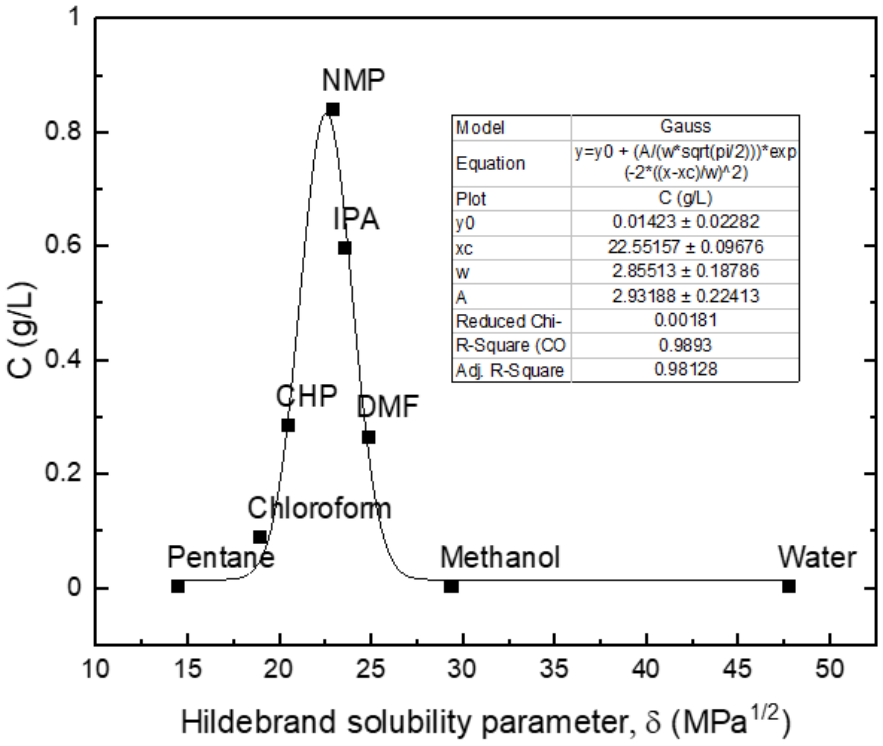

Fig 4.3 fitting data.

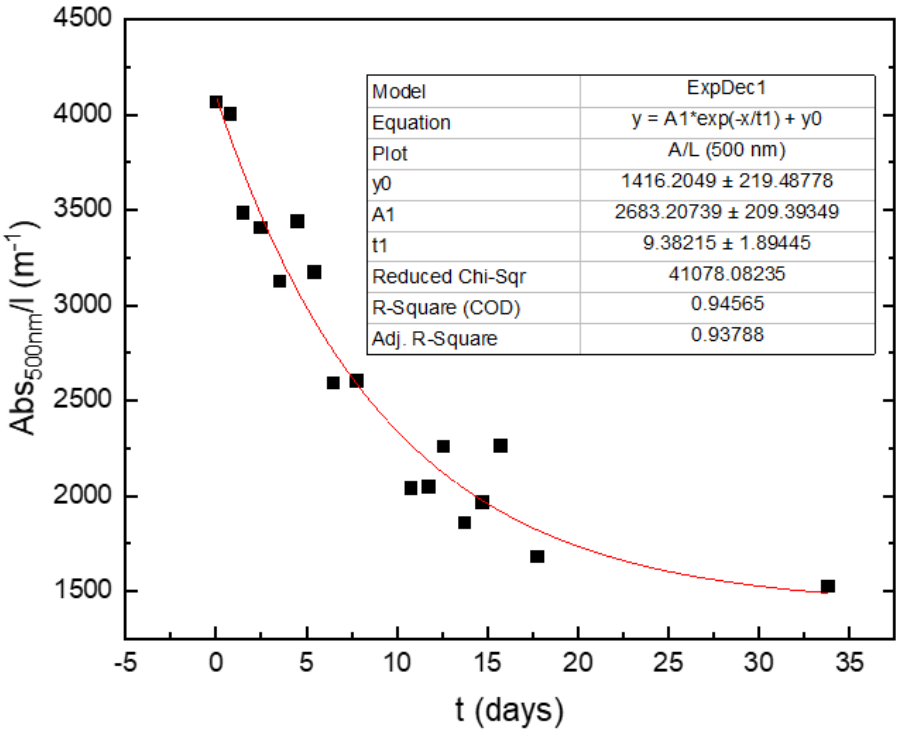

Fig 4.8 (a) fitting data.

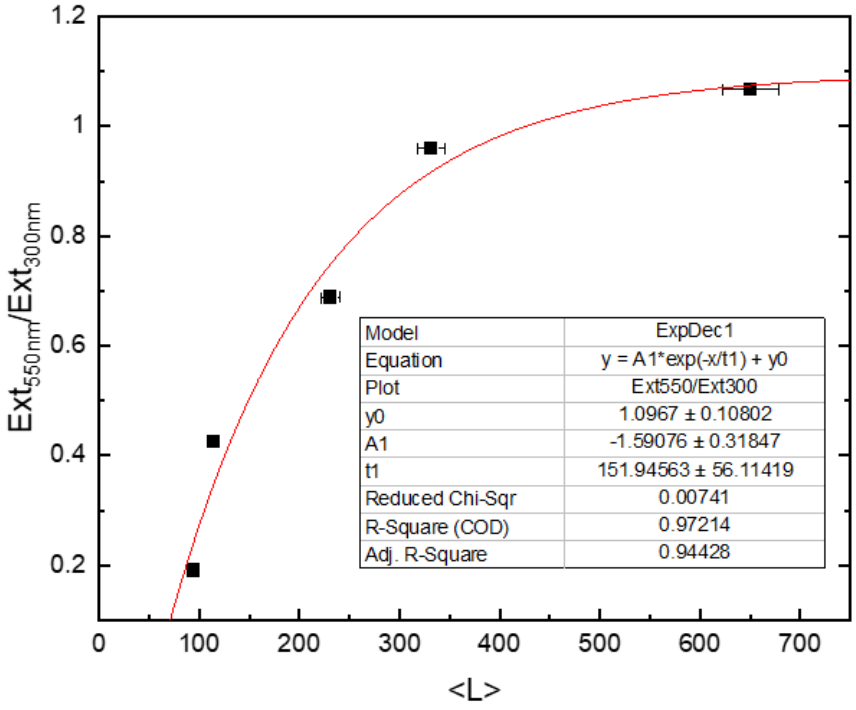

Fig 4.14 fitting data.